

UNIVERSITÀ DEGLI STUDI DI NAPOLI FEDERICO II



Dottorato di Ricerca in Ingegneria Aerospaziale,
Navale e della Qualità (XXII ciclo)

Dipartimento di Ingegneria Aerospaziale

Aerodynamic Analysis of Low Reynolds Number Flows

Tutore
Ch.mo Prof. Renato Tognaccini

Candidato
Pietro Catalano

ANNO ACCADEMICO 2009

ABSTRACT

An aerodynamic analysis of low-Reynolds number flows is presented. The focus is placed on the laminar separation bubbles, a peculiar phenomenon of these kind of flows. The only simulations techniques feasible to be applied to complex configurations appear to be the methods based on the Reynolds Averaged Navier Stokes equations. A critical point is the turbulence modelling. In fact, the turbulence models are calibrated for flows at high Reynolds number with separation in the turbulent regime.

The flow over a flat plate with an imposed pressure gradient, and around the Selig-Donavan 7003 airfoil is considered. Large eddy simulations have also been performed and used as reference for the RANS results.

Laminar separation bubbles have been found by the Spalart-Allmaras and the $\kappa - \omega$ SST turbulence models. The models have been used without prescribing the transition location and assuming low values of the free-stream turbulence.

The main results have been achieved for the $\kappa - \omega$ SST turbulence model. This model is very reliable for transonic flows at high Reynolds number, but has shown limits when applied to low-Reynolds number flows. A modification of the model has been proposed. The modified model, named as $\kappa - \omega$ SST-LR, has provided a correct simulation of the boundary layer in the tests performed at low and high Reynolds numbers. The laminar separation bubble arising of the SD 7003 airfoil has been well captured. The accuracy of the new model is not reduced in transonic regime.

Nomenclature

∇	Nabla operator
B	Constant in the logarithmic law of velocity
b	Wing span
c	Airfoil chord
C_D	Drag coefficient
C_F	Friction coefficient
C_L	Lift coefficient
C_P	Pressure coefficient
DES	Detached eddy simulation
DNS	Direct numerical simulation
e	Energy (Internal + Kinetic) per unit mass
$ILES$	Implicit large eddy simulation
L	Length
LES	Large eddy simulation
LSB	Laminar separation bubble
p	Static pressure
$RANS$	Reynolds Averaged Navier Stokes
Re	Reynolds number
RSM	Reynolds Stress Model
SD	Selig-Donovan
SST	Shear Stress Transport
T	Temperature
t	Time

t_{ij}	Viscous stress tensor
u,v,w	Velocity components in x,y,z directions
u_i	Velocity in tensor notation
u_τ	Friction velocity
V	Module of the velocity
x,y,z	Cartesian coordinates
x_i	Position vector in tensor notation
y^+	Viscous coordinate in the wall-normal direction, $\frac{u_\tau y}{\nu}$

Subscripts

∞	Free stream conditions
<i>ref</i>	Reference
<i>tr</i>	Transition

Symbols

α	Angle of attack
δ^*	Displacement thickness
δ_{ij}	Kronecker delta
η	Kolmogorov length scale
	Self-similar coordinate
κ	Turbulent kinetic energy
κ_a	von Kármán constant
λ	Heat conduction coefficient
μ	Molecular viscosity
μ_t	Eddy viscosity
ν	Kinematic viscosity, $\frac{\mu}{\rho}$
Ω	Vorticity
ω	Specific turbulent dissipation rate
ρ	Density
τ_{ij}	Sub-grid stress tensor
	Reynolds stress tensor
τ_w	Surface shear stress
τ_{xy}	Reynolds shear stress

$\tilde{\nu}$	Working variable of the Spalart-Allmaras turbulence model
ε	Turbulent dissipation rate
t_η	Kolmogorov time scale
u_η	Kolmogorov velocity scale

Superscripts

+	Viscous units
---	---------------

Contents

1	Introduction	1
1.1	Aerodynamics of Low Reynolds Number Flows	2
2	Physical and Mathematical Model	7
2.1	Large Eddy Simulation	10
2.1.1	Subgrid Modelling	10
2.1.2	Dynamic Models	11
2.1.3	LASSIE Code	12
2.1.3.1	Numerical method	13
2.2	Reynolds Averaging of the Navier-Stokes Equations	14
2.2.1	The One-equation Spalart-Allmaras Turbulence Model	16
2.2.1.1	Free Shear Layer Flows	16
2.2.1.2	Wall Bounded Flows	17
2.2.2	The Two-equation Turbulence Models	20
2.2.2.1	The κ - ω Wilcox model	22
2.2.2.1.1	Free Shear Layer Fows	22
2.2.2.1.2	Boundary Layer Flows	23
2.2.2.1.2.1	The log layer	23
2.2.2.1.2.2	The defect layer	24
2.2.2.1.2.3	The viscous sublayer	25
2.2.2.1.3	Free-stream Dependency	27
2.2.2.2	The κ - ω TNT model	28
2.2.2.3	The κ - ω SST turbulence model	30

2.2.3	ZEN Code	33
2.2.3.1	Numerical definition	34
2.2.3.2	UZEN: the Time-accurate Version	36
2.3	Detached Eddy Simulation	37
2.3.1	SA-DES	37
2.3.2	SST-DES	38
3	Laminar Separation Bubbles	39
3.1	Flow over a Flat Plate	40
3.1.1	Numerical Set-up	40
3.1.2	Influence of free-stream Turbulence	44
3.2	Flow around the SD 7003 Airfoil	53
3.2.1	Grid Assessment	53
3.2.2	Turbulence Models Assessment	55
3.2.3	Results by κ - ω SST turbulence model	55
3.2.3.1	Main Characteristics of the Flow	56
3.2.3.2	Large Eddy Simulations	57
3.2.3.3	RANS-LES Comparison	60
3.2.3.4	Flow at $\alpha = 4^\circ$	62
4	Turbulence Modelling	65
4.1	Analysis of the the κ - ω SST model	65
4.2	The κ - ω SST-LR model	69
4.2.1	Analysis for Low Reynolds Number Flows	72
4.3	Drag polar of the SD 7003 airfoil	80
4.3.1	Stall Characteristics	83
5	Transonic Flows	86
5.1	RAE 2822 Airfoil	86
5.1.1	Case 9	86
5.1.2	Case 10	87
5.2	RAE M2155 Wing	89

6	Conclusions	91
----------	--------------------	-----------

Introduction

Aerodynamic performances of aerial vehicles are largely influenced by the Reynolds number. The different flow regimes occurring in a wide range of Reynolds numbers are well described by Carmichael [1].

The regime at Reynolds number lower than 10^2 is of interest for devices used to reduce the turbulence level of wind tunnels, but not for airfoil-like machines.

The regime of Reynolds number up to 10^4 regards insects and small model airplanes. The flow is strongly laminar and not able to sustain adverse pressure gradients. Some interesting solutions are adopted in nature in order to prevent the separation. The dragonfly has a saw tooth single surface airfoil. It is thought that eddies are formed in the troughs and keep the flow attached. The fly has a large number of fine hair-like elements that promote an eddy-induced energy transfer and prevent separation.

The range of Reynolds number between $10^4 - 10^5$ is typical of flying animals and large model airplanes. At the lower end of this regime, natural laminar regime is possible provided that the lift coefficient of the flying machine remains quite low (≈ 0.5). Higher lift coefficients would produce a flow separation without re-attachment with a drop in lift and a rise of the drag coefficient. Carmichael [1] has pointed out that, under natural laminar flow separation, the distance between the separation and the re-attachment point expressed in terms of Reynolds number is about 50000. Thus, if a separation occurs at Reynolds number lower than 50000, the distance to the trailing edge is insufficient for the re-attachment of the flow. At higher Reynolds

number re-attachement is possible, but the bubble is of significant length with an important impact on the performance.

The next Reynolds number regime, up to 10^6 , is of interest of large soaring birds but also of large radio controlled model aircrafts, ultra-light gliders, and human powered aircrafts. Airfoils for wind turbines also operate in this regime. Extensive laminar flow is possible and the performances of the airfoils are improved with respect to lower Reynolds numbers.

Large aircrafts fly at Reynolds numbers of order of magnitude $10^7 - 10^8$. It is still possible to obtain large regions of laminar flows. The flight altitude has to be high in order to keep the Reynolds number per unit length reasonably low. Favourable pressure gradients are necessary and are obtained through a careful design of the wing sections. Devices to stabilize the boundary layer are also used.

Reynolds numbers still higher are typically for large water-immersed vehicles such as tankers and nuclear submarines.

1.1 Aerodynamics of Low Reynolds Number Flows

The limit of the low Reynolds number regime is usually indicated to be 2×10^5 [2, 3]. Below this limit, the drag polar of the airfoils present a decline of the aerodynamic efficiency due to the presence of laminar separations.

The research in the field of the low Reynolds number flows is being pushed by the the growing interest of the aerospace industries in unmanned and micro-aerial vehicles (UAV and MAV). UAV wings typically operate at a Reynolds number of $10^4 - 10^5$. At these Reynolds numbers, the flow cannot sustain strong adverse pressure gradients and often separates in the laminar regime. The disturbances present in the laminar region are amplified inside the separated shear layer and transition to the turbulent regime occurs. The turbulence developing inside the re-circulation region enhances the momentum transport and the flow re-attaches.

This phenomenon, the laminar separation bubble, is one of the main critical aspects of flows at low Reynolds numbers and adversely affects the performance of an airfoil. Thick bubbles change the effective contour of an airfoil. This results in an increase of the pressure drag. Suction is reduced in the aft part and pressure recovery is decreased in the rear part of the airfoil. Skin friction drag increases as well due to the rise of the turbulent momentum. A more significant effect occurs when the turbulent transport is not sufficient to close the bubble. The separated region extends up to the trailing edge. This causes a loss of lift and an increase of drag with hysteresis effects of the force coefficients with the angle of attack.

The only simulation techniques feasible to be applied to complex configurations such as High Altitude Long Endurance (HALE) unmanned vehicles appear to be the methods based on the Reynolds Averaged Navier Stokes equations. A critical point in applying the RANS approach to low Reynolds number flows is the turbulence modelling. In fact the presence of separation bubbles means that the separation is laminar and that the transition points are very difficult to be set. The turbulence models are instead calibrated for separation in the turbulent flow regime, and need the transition points to be known *a priori*.

Spalart and Strelets [4] performed a direct numerical simulation (DNS) of a separation bubble over a flat plate. They also applied the RANS equations arguing that turbulence models should be able to deal with this kind of flow, where the transition is due to the flow that re-circulating inside the separated region brings turbulent fluid upstream in the laminar zone. They used a so-called "trip-less" approach consisting of setting non-zero turbulence inflow values during the first iterations and then setting zero turbulence values until a steady state is reached. The Spalart-Allmaras model [5] finds a bubble but with a slow recovery and a re-attachment more downstream with respect to DNS results. The $\kappa - \omega$ SST model [6] provides a separation only if modified by a term derived from the Spalart-Allmaras model.

The possibility of using the Reynolds Averaged Navier Stokes equations for the numerical simulation of low Reynolds number flows and laminar sep-

aration bubbles is addressed in several papers. Howard *et al.* [7] performed RANS simulations of a laminar bubble over a flat plate using the $\kappa - g$ model [8] with and without fixing the transition point, and modified by using coefficients depending on the local turbulent Reynolds number as proposed by Wilcox [9]. The model without any treatment of the transition provides a very weak separation. The model with modified coefficients presents a bubble with a re-attachment anticipated with respect to DNS. The $\kappa - g$ model not modified but applied with the transition point imposed returns a bubble. The re-attachment point is located more downstream than DNS data.

The RANS approach, with some treatment to take into account the transition phenomenon, has been applied to the Selig-Donovan 7003 airfoil by several researchers. This airfoil has been specifically designed for small model gliders at Reynolds number below 10^5 , and exhibits a relatively large laminar bubble over a broad range of incidences at Reynolds number of 6×10^4 . The Selig-Donovan 7003 airfoil has been the subject of numerical and experimental investigations [3].

Windte [10], Radespiel [11], Yuan *et al.* [12] employed a RANS solver coupled to a transition prediction method to simulate the flow around the SD7003 airfoil at $Re = 6 \times 10^4$. Contour plots of Reynolds stresses are presented. Some interesting results were achieved by the Menter BSL-two layer model [6], the explicit algebraic Reynolds stress model by Wallin [13], and the Wilcox RSM model [9]. The drag polar of the airfoil is computed with a reasonable accuracy at low angle of attack. A systematic over-prediction of the C_L with respect to the experiments is however noted. Some dependence of the results on the choice of the N_{crit} is seen mainly at the high incidences.

An easier approach has been also tried. Tang [14] applied the RANS equations without any particular treatment of the transition to the flow at $Re = 6 \times 10^4$ around the SD 7003 airfoil. First a laminar simulation is performed. The transition is considered to occur in the separated region at the point where the flow reverses direction and moves downstream. Then, a simulation with imposed transition point is performed. Results are presented for the flow at $\alpha = 4^\circ$ in terms of contour plot of the Reynolds stresses,

pressure coefficient, and velocity contours with stream-lines. Good results are achieved by the Spalart-Allmaras model. A too short bubble is instead returned by the Menter BSL-two layer, and the Jones-Lauder [15] $\kappa - \varepsilon$ models.

Large eddy simulations of low Reynolds number flows are becoming affordable, at least for validating the results of the much faster RANS solvers. Indeed, LES of the flow around the SD 7003 airfoil have been performed. Yuan *et al.* [12] employed an incompressible solver using the SIMPLE algorithm [16] for the pressure-velocity coupling. The static Smagorinsky and the selective scale model by Lenormand *et al.* [17] have been used as sub-grid closures of the Navier Stokes equations. The flow at $Re = 6 \times 10^4$, and $\alpha = 4^\circ$ has been computed. Differences with respect to RANS results in the zone of the bubble in terms of pressure and friction coefficients are shown. The importance of 3D fluid structures is discussed. Galbraith and Visbal [18] applied an high-order implicit LES to compute the entire drag polar of the SD7003 airfoil at $Re = 6 \times 10^4$. Good accuracy with the experimental data is shown. The stall is well predicted. The C_L compares well with the experiments also at a post-stall angle, while the C_D is over-predicted.

Rumsey and Spalart [19] have performed an analysis of the behaviour of the Spalart-Allmaras and the $\kappa-\omega$ SST (modified adding sustaining terms [20]) turbulence models in low Reynolds number regions of an aerodynamic flow field. They tested the behaviour of the models over a flat plate with decreasing values of the free-stream turbulence, and found that the $\kappa-\omega$ SST exhibits a correct trend for the transition to turbulence. Rumsey and Spalart [19] also considered the flow around the NACA 0012 airfoil at Reynolds number 1×10^5 . The main conclusion of their article is that “these models are intended for fully turbulent high Reynolds number computations, and using them for transitional (e.g., low Reynolds number) or relaminarizing flows is not appropriate. Competing models which fare better in these areas have not been identified.”

The main aim of the activities reported in this thesis has been to give a contribution to the numerical simulations of low Reynolds number flows.

The physical and mathematical models adopted are described in the chapter 2.

Chapter 3 deals with the phenomenon of the laminar separation bubbles. A RANS method is applied by using several turbulence models to the incompressible flow over a flat plate with an imposed pressure gradient and around the Selig-Donovan 7003 airfoil. Large eddy simulations of the flow around the SD 7003 airfoil have been also performed and used as a reference for the results achieved by RANS. The laminar separation bubbles are reproduced without specifying the location of the transition from the laminar to the turbulent regime. The turbulence models are run assuming the flow turbulent in all the flow field and adopting low values of the free-stream turbulence.

The chapter 4 focus on the κ - ω SST turbulence model, a model that, despite of the limits shown in low Reynolds number applications, is very reliable for transonic flows, as pointed out by different authors (cfr. Catalano and Amato [21, 22]). The limits of this model have been confirmed. However it is shown that they are not due to “design” problems of the model but rather to its implementation. Indeed a modification of the SST formulation is proposed. This allows for a very satisfactory simulation of the laminar separation bubble when the transition point is prescribed. An excellent agreement with the LES results is obtained in terms of pressure and skin friction distributions along the SD 7003 airfoil. The κ - ω SST model, with low Reynolds modifications, has been applied to compute the drag polar of the SD 7003 airfoil. The new turbulence model has shown results in good agreement with both experimental and LES data. The angle and the characteristics of the stall of the SD 7003 airfoil have been well predicted.

The “performance” of the new model is not reduced in transonic regime at high Reynolds number. This is shown in chapter 5 where the flow around typical transonic benchmark, such as the airfoil RAE 2822 and the wing RAE M2155, is discussed.

The conclusions are drawn in the chapter 6.

Physical and Mathematical Model

The equations of the fluid dynamics are the well-known Navier-Stokes equations that come directly from the conservation laws of mass, momentum and energy. These equations, under the hypothesis of *continuum* flow, no dissociation, no real gas effects, fluid in a state of thermodynamic equilibrium, negligibility of body forces and heat sources, have the following form in a cartesian coordinate system :

$$\frac{\partial U}{\partial t} + \frac{\partial F_1^c}{\partial x} + \frac{\partial F_2^c}{\partial y} + \frac{\partial F_3^c}{\partial z} = \frac{\partial F_1^\nu}{\partial x} + \frac{\partial F_2^\nu}{\partial y} + \frac{\partial F_3^\nu}{\partial z} \quad (2.1)$$

where

$$U = \begin{pmatrix} \rho \\ \rho u \\ \rho v \\ \rho w \\ \rho e \end{pmatrix} \quad (2.2)$$

is the vector of the unknown flow variables,

$$F_1^c = \begin{pmatrix} \rho u \\ \rho u^2 + p \\ \rho uv \\ \rho uw \\ (\rho e + p)u \end{pmatrix} \quad F_2^c = \begin{pmatrix} \rho v \\ \rho vu \\ \rho v^2 + p \\ \rho vw \\ (\rho e + p)v \end{pmatrix} \quad F_3^c = \begin{pmatrix} \rho w \\ \rho wu \\ \rho wv \\ \rho w^2 + p \\ (\rho e + p)w \end{pmatrix} \quad (2.3)$$

are the convective, and

$$\begin{aligned}
 F_1^\nu &= \begin{pmatrix} 0 \\ t_{11} \\ t_{12} \\ t_{13} \\ ut_{11} + vt_{12} + wt_{13} - q_1 \end{pmatrix} \\
 F_2^\nu &= \begin{pmatrix} 0 \\ t_{21} \\ t_{22} \\ t_{23} \\ ut_{21} + vt_{22} + wt_{23} - q_2 \end{pmatrix} \\
 F_3^\nu &= \begin{pmatrix} 0 \\ t_{31} \\ t_{32} \\ t_{33} \\ ut_{31} + vt_{32} + wt_{33} - q_3 \end{pmatrix}
 \end{aligned} \tag{2.4}$$

the diffusive fluxes. The stress tensor t_{ij} is related to the strain tensor through the molecular viscosity μ

$$t_{ij} = \mu \left(\frac{\partial u_i}{\partial x_j} + \frac{\partial u_j}{\partial x_i} - \frac{2}{3} \frac{\partial u_k}{\partial x_k} \delta_{ij} \right) \tag{2.5}$$

with $i = 1..3$, $j = 1..3$ and the convention on the summation of the repeated indices is used. The heat flux q_j is defined by the Fourier law as

$$q_j = -\lambda \frac{\partial T}{\partial x_j} \tag{2.6}$$

The equations (2.1) with the initial and boundary conditions are, for a laminar flow regime, a closed system of equations once the dependence of the molecular viscosity and thermal conductivity on the thermodynamic properties of the flow are specified. The relations $\mu = \mu(p, T)$, $\lambda = \lambda(p, T)$ together with the state thermodynamic equation are the closures needed.

In the turbulent regime, the scenario is different. The flow exhibits scales with large variations in space and time. The direct resolution of all the motion scales can be prohibitively expensive and depends on the Reynolds number. Following the Kolmogorov hypotheses, the statistics of the smallest scales of motion are uniquely determined by the molecular viscosity ν and by the dissipation rate of the turbulent kinetic energy ε . The length, velocity and time Kolmogorov scales are built on the basis of dimensional analysis as

$$\eta = (\nu^3/\varepsilon)^{1/4} \quad u_\eta = (\nu\varepsilon)^{1/4} \quad \tau_\eta = (\nu\varepsilon)^{1/2} \quad (2.7)$$

with $\varepsilon \approx u^3/L$. The spatial resolution must to be of order of magnitude η and the size of the computational domain has to be proportional to the most energetic scale of the flow L . The number of points required to resolve the Kolmogorov scales in the three computational directions is

$$N = N_1 * N_2 * N_3 = \left(\frac{L}{\eta}\right)^3 = \mathcal{O}(Re^{9/4}) \quad (2.8)$$

The equations have to be resolved in time with a time step $\Delta t \approx \tau_\eta$ (without taking into account numerical stability requirements) for a number of time steps

$$N_T = \frac{T}{\Delta t} \approx \frac{L}{u\tau_\eta} = \mathcal{O}(Re^{1/2}) \quad (2.9)$$

The cost of a simulation is proportional to $N * N_T = \mathcal{O}(Re^{11/4})$ rapidly growing with the Reynolds number.

The direct numerical simulation (DNS) of all the motion scales of a turbulent flow is limited to flows at $Re = \mathcal{O}(10^{3,4})$. An averaging of the Navier Stokes equations is performed in order to make affordable the numerical simulation of flows at higher Reynolds number. The results discussed in this thesis have been achieved by numerical methods based on Large Eddy Simulations (LES), and the Reynolds Averaged Navier Stokes equations (RANS), based respectively on a spatial and time averaging of the (2.1).

2.1 Large Eddy Simulation

A spatial filtering of the Navier-Stokes equations is introduced by the following operation

$$\bar{f}(\underline{x}, t) = \int_D f(\underline{x}', t) \bar{G}(\underline{x} - \underline{x}', \Delta) d\underline{x}' \quad (2.10)$$

where f is a fluid dynamic variable, \bar{G} the filter function, Δ the filter width, and D stands for the computational domain. The filtered equations allow to resolve the scale of the motion up a certain size, while the effect of the unresolved scales needs to be modelled. The Large Eddy Simulation resolves the large scales of motion; the scales that carry the energy, are dynamically more important, and are characteristics of the flow. The small scales of the motions; the scales where the dissipation of energy in heat takes place are modelled. These scales are believed to be homogeneous, isotropic and not dependent on the particular flow.

The unknown term, that takes into account the effect of the unresolved scales on the resolved ones, is the subgrid stress tensor given by :

$$\tau_{ij} = \overline{u_i u_j} - \bar{u}_i \bar{u}_j \quad (2.11)$$

2.1.1 Subgrid Modelling

Many subgrid models make use of the "eddy viscosity" concept relating the subgrid stress tensor (2.11) to the resolved strain tensor through the subgrid scale viscosity ν_{sgs} as

$$\tau_{ij} - \frac{1}{3} \delta_{ij} \tau_{kk} = -2\nu_{sgs} \bar{S}_{ij} = -\nu_{sgs} \left(\frac{\partial \bar{u}_i}{\partial x_j} + \frac{\partial \bar{u}_j}{\partial x_i} \right) \quad (2.12)$$

The Smagorinsky model, the progenitor of most subgrid models, comes from the equilibrium hypothesis. It is supposed that at the small scale level, the production of the subgrid kinetic energy is balanced by the viscous dissipation ε_ν :

$$-\tau_{ij} \bar{S}_{ij} = \varepsilon_\nu \quad (2.13)$$

The substitution of (2.11) into the (2.13) yields

$$-2\nu_{sgs}\overline{S_{ij}}\overline{S_{ij}} \propto \frac{\kappa_{sgs}^3}{l} \quad (2.14)$$

where it has been considered that the viscous dissipation is proportional to the subgrid kinetic energy κ_{sgs} and to a length scale l

$$\epsilon_\nu \propto \frac{\kappa_{sgs}^3}{l} \quad (2.15)$$

Since $\nu \propto \kappa_{sgs}l$ and l is proportional to the filter width Δ , the subgrid kinetic energy results

$$\kappa_{sgs} \propto \Delta(2\overline{S_{ij}}\overline{S_{ij}}) = 2\Delta|\overline{S}| \quad (2.16)$$

Therefore, the subgrid viscosity is obtained as

$$\nu_{sgs} = (C_S\Delta)^2|\overline{S}| \quad (2.17)$$

The Smagorinsky constant C_S is real with an usual value between 0.1 and 0.2. In presence of solid boundaries, the length scale is modified by the Van Driest damping function in order to take into account the reduced growth of the small scale close to a wall. The (2.17) is modified to

$$\nu_{sgs} = [C_S\Delta(1 - e^{-\frac{y^+}{25}})]^2|\overline{S}| \quad (2.18)$$

2.1.2 Dynamic Models

In the dynamic models the Smagorinsky constant C_S is not more assigned "a priori" but is computed during the numerical simulation. A new filter, the test filter function \hat{G} with a width $\hat{\Delta} > \Delta$ is introduced. The application of the filter function \hat{G} to the Navier Stokes equations gives rise to the filtered quantities

$$\hat{f}(\underline{x}, t) = \int_D f(\underline{x}', t)\hat{G}(\underline{x} - \underline{x}', \hat{\Delta}, \Delta)d\underline{x}' \quad (2.19)$$

and to subgrid stresses that read as

$$T_{ij} = \widehat{\overline{u_i u_j}} - \hat{u}_i \hat{u}_j \quad (2.20)$$

It is possible to consider the resolved turbulent stresses

$$L_{ij} = \widehat{\overline{u_i u_j}} - \widehat{u_i} \widehat{u_j} \quad (2.21)$$

that represent the contribution to the Reynolds stresses of the scales whose length is intermediate between the test filter $\hat{\Delta}$ and the filter Δ . It is worth noting that L_{ij} are not unknown and can be computed explicitly. Instead, an eddy viscosity model is assumed for both τ_{ij} and T_{ij}

$$\tau_{ij} - \frac{1}{3} \delta_{ij} \tau_{kk} = -2C \Delta^2 |\overline{S}| \overline{S}_{ij} \quad (2.22)$$

$$T_{ij} - \frac{1}{3} \delta_{ij} T_{kk} = -2C \hat{\Delta}^2 |\hat{S}| \hat{S}_{ij} \quad (2.23)$$

Equation (2.21) can be rearranged as

$$L_{ij} = \widehat{\overline{u_i u_j}} - \widehat{u_i} \widehat{u_j} + \widehat{\overline{u_i u_j}} - \widehat{u_i} \widehat{u_j} = T_{ij} - \hat{\tau}_{ij} \quad (2.24)$$

The substitution of equations (2.22) and (2.23) into the (2.24) provides a relation usable for the determination of C . Equation (2.24) cannot be satisfied exactly because the stress tensors have been replaced by a model. Furthermore the system of equations (2.24) is overestimated since there are more equations than unknowns. These issues are addressed by considering that the error in resolving the (2.24)

$$e_{ij} = L_{ij} - T_{ij} + \hat{\tau}_{ij} = L_{ij} + 2C \left(\hat{\Delta}^2 |\hat{S}| \hat{S}_{ij} - \Delta^2 |\overline{S}| \overline{S}_{ij} \right) = L_{ij} + 2CM_{ij} \quad (2.25)$$

be minimized in a least-square sense

$$\frac{\partial \langle e_{ij} e_{ij} \rangle}{\partial C} = 2 \left\langle e_{ij} \frac{\partial e_{ij}}{\partial C} \right\rangle = 2 \left\langle (L_{ij} + 2CM_{ij}) M_{ij} \right\rangle = 0 \quad (2.26)$$

and

$$C = -\frac{1}{2} \frac{\langle L_{ij} M_{ij} \rangle}{\langle M_{ij} M_{ij} \rangle} \quad (2.27)$$

2.1.3 LASSIE Code

An incompressible flow solver of the Navier Stokes equations has been used for the large eddy simulations [23]. The code employs an energy-conservative

numerical scheme. Second order central differences in stream-wise and wall-normal directions, and Fourier collocations in the span-wise direction are used. The code is written in body-fitted coordinates with a staggered arrangement of the flow variables. The fractional step approach [24], in combination with the Crank-Nicholson method for the viscous terms and the 3rd order Runge-Kutta scheme is used for the time advancement. The continuity constraint is imposed at each Runge-Kutta substep by solving a Poisson equation for the pressure. The subgrid scale stress tensor is modelled by the dynamic Smagorinsky model [25] in combination with a least-contraction and span-wise averaging [26].

2.1.3.1 Numerical method

The momentum equation of the (2.1) is written for an incompressible flow as

$$\frac{\partial u_j}{\partial t} + \frac{\partial u_i u_j}{\partial x_j} = -\frac{\partial p}{\partial x_j} + \frac{\partial}{\partial x_k} \left((\nu + \nu_{SGS}) \frac{\partial u_j}{\partial x_k} \right) \quad (2.28)$$

The (2.28) is advanced in time with a time step Δt in three stages ($m = 1..3$).

1. A velocity field is evaluated as

$$\begin{aligned} \frac{\hat{u}_j - u_j^n}{\Delta t} + \left(\gamma_m H(u_i^n) + \zeta_m H(u_i^{n-1}) \right) &= -\frac{\partial p^n}{\partial x_j} + \\ &+ \left(\alpha_m L(u_j^n) + \beta_m L(\hat{u}_j) \right) \end{aligned} \quad (2.29)$$

where H and L stand for the convective and diffusive operator.

2. The field \hat{u}_j is updated as

$$\frac{u_j^* - \hat{u}_j}{\Delta t} = \left(\alpha_m + \beta_m \right) \frac{\partial p^n}{\partial x_j} \quad (2.30)$$

3. The field u_i^* is not divergence-free. The continuity is enforced by up-grading the pressure solving

$$\frac{1}{\Delta t} \frac{\partial u_j^*}{\partial x_j} = \left(\alpha_m + \beta_m \right) \frac{\partial p^{n+1}}{\partial x_j} \quad (2.31)$$

4. The solenoidal velocity field at the time level $n + 1$ is evaluated as

$$u_j^{n+1} = u_j^* - (\alpha_m + \beta_m) \Delta t \frac{\partial p^{n+1}}{\partial x_j} \quad (2.32)$$

The coefficients used are the following :

$$\begin{aligned} \gamma_1 &= \frac{1}{\sqrt{3}} & \gamma_2 &= \frac{1}{2\sqrt{3}} = & \gamma_3 &= 1.0 \\ \zeta_1 &= 0 & \zeta_2 &= \frac{1}{2} - \frac{1}{\sqrt{3}} & \zeta_3 &= -\frac{1}{2} - \frac{1}{2\sqrt{3}} \\ \alpha_m &= \beta_m = \gamma_m + \zeta_m \end{aligned} \quad (2.33)$$

It is worth noting that $\alpha_1 + \alpha_2 + \alpha_3 = \beta_1 + \beta_2 + \beta_3 = 0.5$

2.2 Reynolds Averaging of the Navier-Stokes Equations

A time averaging process of the (2.1) is performed. Instantaneous flow variables are considered as the sum of a mean and a fluctuating value :

$$f(\underline{x}, t) = \bar{f}(\underline{x}, t) + f'(\underline{x}, t) \quad (2.34)$$

The mean value is computed by averaging the variable over a time interval ΔT much larger than the period of the fluctuating part but smaller than the time interval associated with the unsteady flow :

$$\bar{f}(\underline{x}, t) = \frac{1}{\Delta T} \int_0^{\Delta T} f(\underline{x}, t) dt \quad (2.35)$$

Therefore :

$$\overline{f'(\underline{x}, t)} = 0 \quad , \quad \overline{\bar{f}(\underline{x}, t)} = \bar{f}(\underline{x}, t) \quad (2.36)$$

but

$$\overline{f'(\underline{x}, t)g'(\underline{x}, t)} \neq 0 \quad (2.37)$$

The time averaging of (2.1), performed by applying the (2.34 - 2.35) taking into account the (2.36 - 2.37), leads to a system of equations for the mean

value of the unknown flow variables (2.2). These equations, named Reynolds Averaged Navier Stokes (RANS), are formally identical to (2.3-2.4) with the exception of a new unknown term that comes from the convective fluxes. This term, the Reynolds stress tensor, is constituted by the double correlation of the turbulent velocity fluctuations :

$$\tau_{ij} = -\overline{\rho u'_i u'_j} \quad (2.38)$$

A set of transport equations to directly compute the components of (2.38) can be derived by multiplying the Navier Stokes equations by the velocity fluctuations and then time-averaging. The resulting Reynolds stress equations read, for an incompressible flow, as:

$$\begin{aligned} \frac{\partial \tau_{ij}}{\partial t} + u_k \frac{\partial \tau_{ij}}{\partial x_k} &= -\tau_{ik} \frac{\partial u_j}{\partial x_k} - \tau_{jk} \frac{\partial u_i}{\partial x_k} + 2\mu \overline{\frac{\partial u'_i}{\partial x_k} \frac{\partial u'_j}{\partial x_k}} + \overline{p' \left(\frac{\partial u'_i}{\partial x_j} + \frac{\partial u'_j}{\partial x_i} \right)} + \\ &+ \frac{\partial}{\partial x_k} \left[\nu \frac{\partial \tau_{ij}}{\partial x_k} + \overline{\rho u'_i u'_j u'_k} + \overline{p' u'_i \delta_{jk}} + \overline{p' u'_j \delta_{ik}} \right] \end{aligned} \quad (2.39)$$

New unknowns have been generated. Although equations for these terms could be obtained, the non linearity of the Navier Stokes equations would generate additional unknown terms. The usual approach is to relate the Reynolds tensor to the resolved mean flow variables through a turbulence model.

The Reynolds tensor, in analogy to (2.5), is made proportional to the mean flow strain tensor through the eddy viscosity :

$$\tau_{ij} = \mu_t \left(\frac{\partial u_i}{\partial x_j} + \frac{\partial u_j}{\partial x_i} - \frac{2}{3} \frac{\partial u_k}{\partial x_k} \delta_{ij} \right) - \frac{2}{3} \rho \kappa \delta_{ij} \quad (2.40)$$

where κ is the turbulent kinetic energy. The task on any turbulence model is to close the RANS equations by computing the eddy viscosity μ_t that is assumed to depend on the velocity and length scale of the turbulent eddies

$$\mu_t \propto \kappa^{1/2} l^\alpha \quad (2.41)$$

Several turbulence models, ranging from algebraic to Reynolds stress models, have been developed and can be found in literature. In the algebraic models [27], the eddy viscosity is completely determined in terms of local flow variables. These models are cheap and robust, but are not able to take into account important effects of the flow history.

2.2.1 The One-equation Spalart-Allmaras Turbulence Model

In the one-equation models, only one or a combination of the turbulent scales are computed by solving a transport equation.

Likely, the Spalart-Allmaras [5] is the most famous one-equation turbulence model. In this model the eddy viscosity is computed by an intermediate variable $\tilde{\nu}$ through the relation

$$\mu_t = \rho\nu_t = \rho\tilde{\nu}f_{v1}(\chi) \quad (2.42)$$

where χ is the ratio between the model working variable $\tilde{\nu}$ and the molecular kinematic viscosity, and f_{v1} is a damping function accounting for the wall effects. The intermediate variable $\tilde{\nu}$ is computed by solving a differential equation that can be written as:

$$\begin{aligned} \frac{D\tilde{\nu}}{Dt} &= C_{b1} \left[1 - f_{t2} \right] \tilde{S}\tilde{\nu} + \frac{1}{\sigma} \left[\nabla \cdot ((\nu + \tilde{\nu})\nabla\tilde{\nu}) + C_{b2}(\nabla\tilde{\nu})^2 \right] \\ &- \left[C_{w1}f_w - \frac{C_{b1}}{\kappa_a^2}f_{t2} \right] \left[\frac{\tilde{\nu}}{d} \right]^2 + f_{t1}\Delta U^2 \end{aligned} \quad (2.43)$$

The physical meaning of each term of the (2.43), and the way the model has been built are explained in the following sections.

2.2.1.1 Free Shear Layer Flows

The basic Spalart-Allmaras turbulence model is well suited for free shear layer flows only, and consists of a transport equation, with a production and a diffusive term, for the eddy viscosity itself

$$\frac{D\nu_t}{Dt} = C_{b1}S\nu_t + \frac{1}{\sigma} \left[\nabla \cdot (\nu_T\nabla\nu_t) + C_{b2}(\nabla\nu_t)^2 \right] \quad (2.44)$$

where S is assumed to be the flow vorticity $|\Omega|$.

Three constants need to be determined. A first idea for the order of magnitude of C_{b1} can be obtained considering an homogeneous shear layer ($S = |\frac{\partial u}{\partial y}|$). For this kind of flow, experimental and DNS data say that ν_T

increases with a growth rate between 0.10 and 0.16, while the present model yields an eddy viscosity that grows exponentially as $e^{C_{b1}St}$. This means that C_{b1} must be of order of magnitude 0.10.

On other hand the lack of a destruction term in the (2.44), gives an inconsistency in case of an isotropic ($S = 0$) turbulent flow where the eddy viscosity decreases with the time as $t^{-\frac{1}{5}}$, and generally for the class of shear flows, such as an axisymmetric wake, in which ν_T decreases. Anyhow the diffusion term of the (2.44) can eliminate this deficiency. In fact the diffusion term can bring down the eddy viscosity if the quantity $\nu_T^{1+C_{b2}}$ does not decrease. Considering an axisymmetric wake this condition is satisfied only if $C_{b2} \leq 1$.

An upper limit for C_{b2} is obtained from the behaviour of a turbulent front which propagates into a non turbulent region. The solution provided by the (2.44) is physically correct only if $C_{b2} > -1$.

Two other constrains for the constants can be found by requiring that the model provides correct levels of the shear stress in two dimensional mixing layer and wakes.

After these calibrations a degree of freedom has still been left. Assuming a value of the constant σ between 0.6 and 1 (the chosen value is $2/3$), the resulting model is better suited for wakes than for jet flows that are anyway less relevant for aeronautical applications.

2.2.1.2 Wall Bounded Flows

In case of boudary layer flows, the equation (2.44) must be modified.

Three distinct regions, the sublayer, the log, and the defect layer, can be discerned in a turbulent boundary layer. The log layer is the zone sufficiently close to the wall where inertial terms can be neglected, but also sufficiently far from the surface that the molecular stress is negligible with respect to the Reynolds stress. The sublayer is the region closest to a solid surface where the turbulence is negligible with respect to the molecular viscous effects. The defect layer extends from the end of the log layer to the border of the

boundary layer.

For the defect and log layers, the transport equation of the Spalart and Allmaras turbulence model is the following

$$\frac{D\nu_t}{Dt} = C_{b1}S\nu_t + \frac{1}{\sigma} \left[\nabla \cdot (\nu_t \nabla \nu_t) + C_{b2}(\nabla \nu_t)^2 \right] - C_{w1} \left[\frac{\nu_t}{d} \right]^2 \quad (2.45)$$

where d is the distance from the wall, and C_{w1} a new constant. The adding of this new term does not affect the values of C_{b1} , C_{b2} , and σ since the last term of equation (2.45) becomes negligible for free shear flows ($d \gg \delta$).

The value of C_{w1} is determined considering the log layer region of a turbulent flow where

$$S = \frac{u_\tau}{\kappa_a d} \quad \nu_t = u_\tau \kappa_a d \quad (2.46)$$

where $u_\tau = \sqrt{\frac{\tau_w}{\rho}}$ is the friction velocity and $\tau_w = \mu \frac{\partial u}{\partial y} \Big|_{y=0}$ the wall shear stress. The equilibrium between production, diffusion, and destruction terms results in the following equation for C_{w1} :

$$C_{w1} = \frac{C_{b1}}{\kappa_a^2} + \frac{(1 + C_{b2})}{\sigma} \quad (2.47)$$

Nevertheless since the last term of the (2.45) decays too slowly in the outer region of the boundary layer, it is multiplied by a function f_w which, following the algebraic models, can be considered dependent on the mixing length $l \equiv \sqrt{\nu_t/S}$. The function f_w is defined in the following way

$$f_w = g \left[\frac{1 + C_{w3}^6}{g^6 + C_{w3}^6} \right]^{\frac{1}{6}} \quad (2.48)$$

$$g = r + C_{w2} (r^6 - r)$$

The variable r depends on the mixing length and on the distance from the wall through the following relation

$$r = \frac{\nu_t}{S \kappa_a^2 d^2} \quad (2.49)$$

The new constants introduced are calibrated by matching the skin friction coefficient on a flat plate.

In order to deal with the sub-layer region of a turbulent flow, the eddy viscosity needs to be computed in terms of a new variable through the introduction of a damping function

$$\nu_T = \tilde{\nu} f_{v1}(\chi) \quad f_{v1} = \frac{\chi^3}{\chi^3 + C_{v1}^3} \quad (2.50)$$

where $\chi = \tilde{\nu}/\nu$. All the variables of the (2.45) are reformulated in terms of $\tilde{\nu}$ instead of ν_t , and S is replaced by

$$\tilde{S} = S + \frac{\tilde{\nu}}{\kappa_a^2 d^2} f_{v2} \quad f_{v2} = 1 - \frac{\chi}{1 + \chi f_{v1}} \quad (2.51)$$

The functions f_{v1} and f_{v2} are constructed in such a way that the new variables maintain their log layer behaviour through the boundary layer. The value of the new constant C_{v1} is 7.1, and has been chosen by Spalart and Allmaras on the basis of their experience.

The final version of the model valid for free shear layer flows, and for boundary layer flows is

$$\frac{D\tilde{\nu}}{Dt} = C_{b1} \tilde{S} \tilde{\nu} + \frac{1}{\sigma} \left[\underline{\nabla} \cdot ((\nu + \tilde{\nu}) \underline{\nabla} \tilde{\nu}) + C_{b2} (\underline{\nabla} \tilde{\nu})^2 \right] - C_{w1} f_w \left[\frac{\tilde{\nu}}{d} \right]^2 \quad (2.52)$$

where also the diffusion term has been modified by the adding of a molecular diffusion term.

In the equation (2.52) the transition is left free. In order to control the flow parameters in the laminar region and to initiate the transition near the specified points, so-called "tripping" terms are added to the (2.52). With these terms the transport equation of the model assumes the form of the (2.43).

The production term of the (2.52) is multiplied by the function $1 - f_{t2}$, with

$$f_{t2} = C_{t3} e^{-C_{t4} \chi^2} \quad (2.53)$$

whose aim is to keep, in the laminar region, the working variable $\tilde{\nu}$ in the range between 0 and its free stream value. The values, chosen on empirical basis, for C_{t3} and C_{t4} are respectively 1.2 and 0.5. In the equation (2.43) ΔU

represents the absolute value of the difference between the velocity at the wall trip point (actually zero) and that at the considering field point. The function f_{t1} is given by the following expression

$$f_{t1} = C_{t1} g_t e^{\left(-C_{t2} \frac{\omega_t^2}{\Delta U^2} [d^2 + g_t^2 dt^2]\right)} \quad (2.54)$$

with $g_t \equiv \min(0.1, \Delta U / \omega_t \Delta x_t)$, and ω_t the vorticity at the trip point, and Δx_t the grid spacing along the wall at the trip point. The function f_{t1} is of the Gaussian type and is dependent on the grid spacing through the parameter g_t . This allows to keep the influence of the transition terms confined nearby the trip point. Numerical experiments have shown that suitable values for C_{t1} and C_{t2} are respectively 1 and 2.

2.2.2 The Two-equation Turbulence Models

The two-equation models, in the limits of the (2.40), are complete in the sense that two transport equations for both the turbulent scales are solved, and the Reynolds tensor can be completely determined from the local state of the mean flow and of the mean turbulent quantities. The velocity scale is chosen to be the square root of the turbulent kinetic energy κ , while the length scale is usually determined from κ and an auxiliary variable ζ .

The transport equations for a generic two-equation turbulence model $\kappa-\zeta$ [21], can be written, in a cartesian coordinate system, as :

$$\frac{\partial U^{\kappa\zeta}}{\partial t} + \frac{\partial E^{\kappa\zeta}}{\partial x} + \frac{\partial F^{\kappa\zeta}}{\partial y} + \frac{\partial G^{\kappa\zeta}}{\partial z} = \frac{\partial E_{\nu}^{\kappa\zeta}}{\partial x} + \frac{\partial F_{\nu}^{\kappa\zeta}}{\partial y} + \frac{\partial G_{\nu}^{\kappa\zeta}}{\partial z} + H^{\kappa\zeta} \quad (2.55)$$

where the the vector of the unknown variables is

$$U^{\kappa\zeta} = \begin{pmatrix} \rho\kappa \\ \rho\zeta \end{pmatrix} \quad (2.56)$$

the convective fluxes are

$$E^{\kappa\zeta} = \begin{pmatrix} \rho u \kappa \\ \rho u \zeta \end{pmatrix} \quad F^{\kappa\zeta} = \begin{pmatrix} \rho v \kappa \\ \rho v \zeta \end{pmatrix} \quad G^{\kappa\zeta} = \begin{pmatrix} \rho w \kappa \\ \rho w \zeta \end{pmatrix} \quad (2.57)$$

and the diffusive fluxes read as

$$E_{\nu}^{\kappa\zeta} = \begin{pmatrix} \mu_{\kappa} \frac{\partial \kappa}{\partial x} \\ \mu_{\zeta} \frac{\partial \zeta}{\partial x} \end{pmatrix} \quad F_{\nu}^{\kappa\zeta} = \begin{pmatrix} \mu_{\kappa} \frac{\partial \kappa}{\partial y} \\ \mu_{\zeta} \frac{\partial \zeta}{\partial y} \end{pmatrix} \quad G_{\nu}^{\kappa\zeta} = \begin{pmatrix} \mu_{\kappa} \frac{\partial \kappa}{\partial z} \\ \mu_{\zeta} \frac{\partial \zeta}{\partial z} \end{pmatrix} \quad (2.58)$$

with μ_{κ} and μ_{ζ} the eddy diffusivities of the turbulent variables. The source term is given by

$$H^{\kappa\zeta} = \begin{pmatrix} P_{\kappa} - D_{\kappa} \\ P_{\zeta} - D_{\zeta} \end{pmatrix} \quad (2.59)$$

where P_{κ}, D_{κ} and P_{ζ}, D_{ζ} stand for the production and destruction term of κ and ζ respectively.

The terms of the transport equation of κ can be derived by considering the equation (2.39) with $i = j$ since $\tau_{ii} = -\overline{\rho u'_i u'_i} = -2\rho\kappa$. The diffusive fluxes take into account for the molecular diffusion of κ , the turbulent transport and the pressure diffusion

$$\mu_{\kappa} \frac{\partial \kappa}{\partial x_j} = \mu \frac{\partial \kappa}{\partial x_j} - \frac{1}{2} \overline{\rho u'_i u'_i u'_j} - \overline{p' u'_j} \quad (2.60)$$

The production represents the rate at which the kinetic energy is transferred from the mean flow to the turbulence

$$P_{\kappa} = \tau_{ij} \frac{\partial u_i}{\partial x_j} \quad (2.61)$$

and the destruction is equal to the dissipation, the rate at which the turbulent kinetic energy is converted into thermal internal energy

$$D_{\kappa} = \varepsilon = \nu \overline{\frac{\partial u'_i}{\partial x_k} \frac{\partial u'_i}{\partial x_k}} \quad (2.62)$$

The equation for ζ can be derived from the Navier Stokes but results much more complicated than (2.39) and involves many unknowns for which reliable closures have not been found. The transport equation for ζ is obtained from the transport equation of κ multiplying by ζ/κ and calibrating the new constants.

The most popular turbulence models make use, as second turbulent scale, of the turbulent dissipation rate ε [15], or of the specific turbulent dissipation

rate $\omega \propto \varepsilon/\kappa$ [9]. The κ - ω models are less stiff and more accurate than κ - ε models for boundary layers flows subject to adverse pressure gradients [28, 29]. Nevertheless, κ - ε models maintain their reliability for wakes and in the zones of the field far from the solid boundaries.

2.2.2.1 The κ - ω Wilcox model

The κ - ω turbulence models consist of two transport equations to determine κ and ω , with the eddy viscosity computed as:

$$\mu_t = \gamma^* \frac{\rho \kappa}{\omega} \quad (2.63)$$

The constant γ^* can be incorporated, with no loss of generality, in the definition of ω .

The transport equations for the standard κ - ω model as proposed by Wilcox [30] are

$$\frac{\partial(\rho\kappa)}{\partial t} + \frac{\partial(\rho\kappa u_j)}{\partial x_j} = \tau_{ij} \frac{\partial u_i}{\partial x_j} - \beta^* \rho \omega \kappa + \frac{\partial}{\partial x_j} \left[(\mu + \sigma_\kappa \mu_t) \frac{\partial \kappa}{\partial x_j} \right] \quad (2.64)$$

$$\frac{\partial(\rho\omega)}{\partial t} + \frac{\partial(\rho\omega u_j)}{\partial x_j} = \gamma \frac{\omega}{\kappa} \tau_{ij} \frac{\partial u_i}{\partial x_j} - \beta \rho \omega^2 + \frac{\partial}{\partial x_j} \left[(\mu + \sigma_\omega \mu_t) \frac{\partial \omega}{\partial x_j} \right] \quad (2.65)$$

The constants present in the above equations have the following values

$$\beta^* = 0.09 \quad \sigma_\kappa = 0.5 \quad \beta = 0.075 \quad \sigma_\omega = 0.5 \quad (2.66)$$

$$\gamma = \frac{\beta}{\beta^*} - \frac{\sigma_\omega \kappa_a^2}{\sqrt{\beta^*}} \quad (2.67)$$

and have been determined by calibrating the model for basic flows.

2.2.2.1.1 Free Shear Layer Fows A first indication for the values of the constants can be achieved by evaluating the decaying process of the homogeneous isotropic turbulence. The equations 2.64 - 2.65, in case of homogeneous isotropic turbulence, simplify to:

$$\frac{\partial \kappa}{\partial t} = -\beta^* \omega \kappa \quad (2.68)$$

$$\frac{\partial \omega}{\partial t} = -\beta \omega^2 \quad (2.69)$$

from which the solution for κ is found to be:

$$\kappa \propto t^{-\beta^*/\beta} \quad (2.70)$$

Experimental observations indicate that $\kappa \propto t^{-n}$ with $n = 1.25 \pm 0.06$ and therefore the ratio

$$\frac{\beta^*}{\beta} = \frac{6}{5} \quad (2.71)$$

has been chosen.

2.2.2.1.2 Boundary Layer Flows Other information to determine the constants, and the near wall behaviour of ω can be achieved by assessing the model for the three regions (viscous, logarithmic and defect) of a turbulent boundary layer.

2.2.2.1.2.1 The log layer is the portion of the boundary layer far enough from the surface to make the molecular viscosity negligible with respect to the eddy viscosity, but close enough to neglect the convection with respect to the production and the diffusion of turbulence. In this zone the logarithmic law of the velocity

$$u^+ = \frac{1}{\kappa_a} \log y^+ + B \quad (2.72)$$

stands, the eddy viscosity varies linearly with the distance from the wall, and the Reynolds shear stress

$$\tau_{xy} = \mu_t \left(\frac{\partial u}{\partial y} + \frac{\partial v}{\partial x} \right) \quad (2.73)$$

results to be constant.

The momentum equation, and the 2.64 - 2.65 reduce to

$$0 = \frac{\partial}{\partial y} \left[\nu_t \frac{\partial u}{\partial y} \right] \quad (2.74)$$

$$0 = \nu_t \left(\frac{\partial u}{\partial y} \right)^2 - \beta^* \omega \kappa + \sigma_k \frac{\partial}{\partial y} \left[\nu_t \frac{\partial \kappa}{\partial y} \right] \quad (2.75)$$

$$0 = \gamma \left(\frac{\partial u}{\partial y} \right)^2 - \beta \omega^2 + \sigma_\omega \frac{\partial}{\partial y} \left[\nu_t \frac{\partial \omega}{\partial y} \right] \quad (2.76)$$

and yield the following solution:

$$u = \frac{u_\tau}{\kappa_a} \log y + \text{constant} \quad \kappa = \frac{u_\tau^2}{\sqrt{\beta^*}} \quad \omega = \frac{u_\tau}{\sqrt{\beta^*} \kappa_a y} \quad (2.77)$$

with $u_\tau = \sqrt{\tau_w/\rho}$ the friction velocity.

By substitution of the above solution in the (2.64) or (2.65), the following expression for the Kármán constant is obtained

$$\kappa_a^2 = \frac{\sqrt{\beta^*} \left(\frac{\beta}{\beta^*} - \gamma \right)}{\sigma_\omega} \quad (2.78)$$

from which the (2.67) can be retrieved.

From the definition of the friction velocity, follows that

$$\tau_w = \rho u_\tau^2 = \sqrt{\beta^*} \rho \kappa \quad (2.79)$$

Several experimental data indicate for the the ratio τ/κ in the log layer a value of about 0.3; thus the value of 0.09 can be assigned to β^* .

2.2.2.1.2.2 The defect layer is the outer region of the boundary layer where the molecular viscosity is negligible with respect to the eddy viscosity. Wilcox [9] has analyzed the defect layer by using a perturbation method. This has allowed to determine, by means of a numerical experimentation, the values of the constants σ_κ and σ_ω .

The perturbation expansion of the defect layer has been made in terms of the ratio of the friction velocity to the Eulerian velocity U_e at the edge of the boundary layer, and of dimensionless coordinates, ξ and η , defined as follows

$$\xi = \frac{x}{L} \quad \eta = \frac{y}{\Delta} \quad \Delta = \frac{U_e \delta^*}{u_\tau} \quad (2.80)$$

where δ^* is the displacement thickness, and L is a characteristic streamwise length scale supposed to be very large with respect to δ^* .

The velocity is expressed as

$$\frac{u(x, y)}{U_e} = 1 - \left(\frac{u_\tau}{U_e} \right) U_1(\xi, \eta) + \dots \quad (2.81)$$

where $U_1(\xi, \eta)$ is the solution of the first order transformed momentum equation with the following boundary conditions

$$\eta \rightarrow \infty \quad U_1 \rightarrow 0 \quad (2.82)$$

$$\eta \rightarrow 0 \quad \frac{\partial U_1}{\partial \eta} \rightarrow -\frac{1}{\kappa_a \eta} \quad (2.83)$$

The turbulent variables, κ and ω , can be expressed as:

$$\kappa = \frac{u_\tau^2}{\sqrt{\beta^*}} \left[K_0(\eta) + \dots \right] \quad (2.84)$$

$$\omega = \frac{u_\tau}{\sqrt{\beta^*} \Delta} \left[W_0(\eta) + \dots \right] \quad (2.85)$$

with K_0 and W_0 solution of the first order transformed turbulence equations with the following boundary conditions

$$\eta \rightarrow \infty \quad K_0(\eta) \rightarrow 0 \quad W_0(\eta) \rightarrow 0 \quad (2.86)$$

$$\eta \rightarrow 0 \quad K_0(\eta) \rightarrow \left[1 + \kappa_1 \eta \log \eta + \dots \right]$$

$$W_0(\eta) \rightarrow \frac{1}{\kappa_a \eta} \left[1 + w_1 \eta \log \eta + \dots \right] \quad (2.87)$$

where κ_1 and w_1 are given by

$$\kappa_1 = \frac{\beta_T / \kappa_a}{\frac{\sigma_\kappa \kappa_a^2}{2\sqrt{\beta^*}} - 1} \quad (2.88)$$

$$w_1 = \frac{\sigma_\kappa \kappa_a^2 / (2\sqrt{\beta^*})}{1 - \beta / (\gamma \beta^*)} \kappa_1 \quad (2.89)$$

and $\beta_T = \frac{\delta^*}{\tau_w} \frac{dP}{dx}$ represents the pressure gradient in dimensionless form.

The defect layer analysis, by using the perturbation method briefly summarized above, has been used by Wilcox to predict the boundary layer over a flat plate in case of zero pressure gradient and for β_T ranging from -0.5 to 9 . The best matching between the numerical and experimental results has been found using $\sigma_\kappa = \sigma_\omega = 0.5$, and therefore these are the values assigned to the two constants.

2.2.2.1.2.3 The viscous sublayer is the region of the boundary layer closest to the surface. In this zone the velocity varies linearly with

the distance from the wall, and the molecular diffusion has to be taken into account. Considering an incompressible pressure constant case and being the convective terms negligible in the sublayer, the momentum equation and the (2.64) - (2.65) reduce to

$$u_\tau^2 = (\nu + \nu_t) \frac{\partial u}{\partial y} \quad (2.90)$$

$$0 = \nu_t \left(\frac{\partial u}{\partial y} \right)^2 - \beta^* \omega \kappa + \frac{\partial}{\partial y} \left[(\nu + \sigma_k \nu_t) \frac{\partial \kappa}{\partial y} \right] \quad (2.91)$$

$$0 = \gamma \left(\frac{\partial u}{\partial y} \right)^2 - \beta \omega^2 + \frac{\partial}{\partial y} \left[(\nu + \sigma_\omega \nu_t) \frac{\partial \omega}{\partial y} \right] \quad (2.92)$$

Wilcox has shown that, for a perfectly smooth surface in the equation (2.92) dissipation and molecular diffusion balance, and the following asymptotic behaviour for ω can be retrieved

$$\omega \rightarrow \frac{6\nu}{(\beta y^2)} \quad y \rightarrow 0 \quad (2.93)$$

The above equation can be used to specify ω at the wall, and permits together with the other boundary conditions

$$y^+ \rightarrow \infty \quad \kappa \rightarrow \frac{u_\tau}{\sqrt{\beta^*}} \quad \omega \rightarrow \frac{u_\tau}{\sqrt{\beta^* \kappa} y} \quad (2.94)$$

$$y^+ \rightarrow 0 \quad u = \kappa = 0 \quad (2.95)$$

to close the set of equations (2.90)-(2.92).

From the solution obtained it is possible to calculate the constant of the logarithmic wall law (2.72) as

$$B = \lim_{y^+ \rightarrow \infty} \left[u^+ - \frac{1}{\kappa_a} \right] \quad (2.96)$$

The standard Wilcox model yields $B = 5.1$, a value that falls well within the scatter of the experimental data.

These results show that the model can be used without additional special viscous damping terms.

2.2.2.1.3 Free-stream Dependency Several applications of the Wilcox κ - ω turbulence models to wall bounded flows can be found in literature [29, 28, 31, 8]. The model has always provided satisfactory results becoming widely used for external transonic aerodynamics. The reason is the simplicity of its formulation in the viscous sublayer. The model does not require the use of damping functions and employs straightforward Dirichlet boundary conditions resulting to be less stiff and more robust than other popular two equation models (i.e. κ - ε).

However a dependency of the results on the free-stream value of ω has been found. This free-stream dependency has been seen to be very strong for free shear layer flows but is also significant for boundary layer flows. Menter [32] has shown that a correct solution for high Reynolds number boundary layer flows can be achieved if a lower limit on ω is imposed. Applying the perturbation analysis of the defect layer the following estimate for this limit is obtained

$$\omega_{lim} = \frac{1}{\beta} \frac{1}{\delta^*} \frac{d}{dx} (U_e \delta^*) = \mathcal{O} \left(10 \frac{U_\infty}{L} \right) \quad (2.97)$$

where L is a characteristic length in the streamwise direction. In practical applications, however, ω_{lim} could result to be too high with respect to the free-stream values of the turbulent variables and therefore its use could be not appropriate.

The κ - ε turbulence model generally does not show to have this free-stream dependency, and since, by performing the change of variable $\omega \rightarrow \varepsilon$, it is possible to see that the main difference between the two models is the so-called cross diffusion term ($\propto \frac{\partial \kappa}{\partial x_j} \frac{\partial \omega}{\partial x_j}$), Menter has proposed to resolve this drawback of the κ - ω models by taking into account this additional term in the evaluation of ω .

Wilcox [33] has proposed a revised model with the inclusion of the cross-diffusion term, and has shown that this term is effective in eliminating the sensitivity to the free-stream value of ω but adversely affects the compressible boundary layer predictions.

2.2.2.2 The κ - ω TNT model

Kok has proposed the TNT κ - ω model [34]. The cross diffusion term is taken into account only if positive, and therefore it is not effective in the near wall region where the gradients of κ and ω have opposite signs. The computation of distances from the wall is avoided. Thus the main advantages of the κ - ω models are preserved.

The equations of the TNT model are

$$\frac{\partial(\rho\kappa)}{\partial t} + \frac{\partial(\rho\kappa u_j)}{\partial x_j} = \tau_{ij} \frac{\partial u_i}{\partial x_j} - \beta^* \rho \omega \kappa + \frac{\partial}{\partial x_j} \left[(\mu + \sigma_\kappa \mu_t) \frac{\partial \kappa}{\partial x_j} \right] \quad (2.98)$$

$$\frac{\partial(\rho\omega)}{\partial t} + \frac{\partial(\rho\omega u_j)}{\partial x_j} = \gamma \frac{\omega}{\kappa} \tau_{ij} \frac{\partial u_i}{\partial x_j} - \beta \rho \omega^2 + \frac{\partial}{\partial x_j} \left[(\mu + \sigma_\omega \mu_t) \frac{\partial \omega}{\partial x_j} \right] + C_D \quad (2.99)$$

where

$$C_D = \sigma_d \frac{\rho}{\omega} \text{Max} \left[\frac{\partial \kappa}{\partial x_j} \frac{\partial \omega}{\partial x_j}, 0 \right] \quad (2.100)$$

The constants are

$$\beta^* = 0.09 \quad \sigma_\kappa = \frac{2}{3} \quad \beta = 0.075 \quad \sigma_\omega = 0.5 \quad \sigma_d = 0.5 \quad (2.101)$$

and the (2.67) always stands for γ .

The values assigned to β and β^* follow from the (2.71) and (2.79), the value of σ_ω has been chosen in order to try to minimize the impact in the near-wall region, and γ always comes from the (2.78). The values of the other two constants σ_κ and σ_d have a weak influence on the solution in the inner boundary layer, and have been determined by Kok by performing an analysis of the 1-dimensional diffusion problem:

$$\frac{\partial u}{\partial t} = \frac{\partial}{\partial y} \left[\nu_t \frac{\partial u}{\partial y} \right] \quad (2.102)$$

$$\frac{\partial \kappa}{\partial t} = \frac{\partial}{\partial y} \left[\sigma_\kappa \nu_t \frac{\partial \kappa}{\partial y} \right] \quad (2.103)$$

$$\frac{\partial \omega}{\partial t} = \frac{\partial}{\partial y} \left[\sigma_\omega \nu_t \frac{\partial \omega}{\partial y} \right] + \sigma_d \frac{1}{\omega} \frac{\partial \kappa}{\partial y} \frac{\partial \omega}{\partial y} \quad (2.104)$$

This set of equations admits a solution consisting of a front between a turbulent and a non turbulent region moving with a velocity c in the positive y direction

$$u = u_0 H(ct - y) \left| \frac{ct - y}{\delta_0} \right|^{\frac{\sigma_\kappa \sigma_\omega}{\sigma_\omega - \sigma_\kappa + \sigma_d}} \quad (2.105)$$

$$\kappa = \kappa_0 H(ct - y) \left| \frac{ct - y}{\delta_0} \right|^{\frac{\sigma_\omega}{\sigma_\omega - \sigma_\kappa + \sigma_d}} \quad (2.106)$$

$$\omega = \omega_0 H(ct - y) \left| \frac{ct - y}{\delta_0} \right|^{\frac{\sigma_\kappa - \sigma_d}{\sigma_\omega - \sigma_\kappa + \sigma_d}} \quad (2.107)$$

where H is the Heaviside function, u_0 , κ_0 , ω_0 are positive constants, and c is given by

$$c = \frac{\kappa_0}{\omega_0 \delta_0} \frac{\sigma_\kappa \sigma_\omega}{\sigma_\omega - \sigma_\kappa + \sigma_d} \quad (2.108)$$

Cazalbou et al. [35] have studied the behaviour of the turbulence models at the edges of a turbulent region and have shown that the (2.105)-(2.107) can be considered as a local solution of the general mono dimensional problem at $y = ct$ if, in the (2.98)-(2.99), the source terms become negligible compared to the diffusion terms when approaching the front. From (2.98) the diffusion, the production, and dissipation terms result respectively

$$\frac{\partial}{\partial y} \left[\sigma_k \nu_t \frac{\partial \kappa}{\partial y} \right] \propto H(ct - y) \left| \frac{ct - y}{\delta_0} \right|^{\frac{\sigma_\kappa - \sigma_d}{\sigma_\omega - \sigma_\kappa + \sigma_d}} \quad (2.109)$$

$$\nu_t \left[\frac{\partial}{\partial y} \right]^2 \propto H(ct - y) \left| \frac{ct - y}{\delta_0} \right|^{\frac{(2\sigma_\kappa - 1)\sigma_\omega + \sigma_\kappa - \sigma_d}{\sigma_\omega - \sigma_\kappa + \sigma_d}} \quad (2.110)$$

$$\beta^* \kappa \omega \propto H(ct - y) \left| \frac{ct - y}{\delta_0} \right|^{\frac{\sigma_\omega + \sigma_\kappa - \sigma_d}{\sigma_\omega - \sigma_\kappa + \sigma_d}} \quad (2.111)$$

and requiring that the exponent in the production and dissipation terms be larger than the one in the diffusion term, the following constraints

$$\sigma_\kappa > 0.5 \quad \sigma_\omega > 0.0 \quad (2.112)$$

are obtained. The same constraints can be obtained from the (2.99).

Imposing that the transported variable (u, κ, ω) go to zero when approaching the front, the following relations are obtained

$$\sigma_\omega - \sigma_\kappa + \sigma_d > 0.0 \quad (2.113)$$

$$\sigma_\kappa - \sigma_d > 0.0 \quad (2.114)$$

Examination of the (2.105) shows that the velocity profile could exhibit an infinite slope at the edge of the front unless

$$\sigma_\omega - \sigma_\kappa + \sigma_d \leq \sigma_\kappa \sigma_\omega \quad (2.115)$$

The (2.112) and (2.113) also ensure that the velocity of the front is positive and therefore that the turbulent front moves into the non turbulent region.

The set of constants proposed by Kok satisfies all the constraints of the turbulent non turbulent (TNT) analysis presented above, while neither the standard Wilcox model nor the Wilcox model including the cross diffusion term ($\sigma_\omega = 0.6, \sigma_\kappa = 1.0, \sigma_d = 0.3$) [33] respect the relation (2.113).

2.2.2.3 The κ - ω SST turbulence model

The Shear Stress Transport (SST) κ - ω turbulence model has been designed by Menter [6] with the aim to retain the robust and accurate formulation of the Wilcox model in the near wall region, and to take advantage of the free-stream independence of the κ - ε model in the outer part of the boundary layer and in the wakes. In order to achieve this, the constants of the model and the cross diffusion term are multiplied by a blending function equal to one in the near wall region and equal to zero away from the surface.

The transport equations of the SST κ - ω turbulence model read as

$$\frac{\partial(\rho\kappa)}{\partial t} + \frac{\partial(\rho\kappa u_j)}{\partial x_j} = \tau_{ij} \frac{\partial u_i}{\partial x_j} - \beta^* \rho \omega \kappa + \frac{\partial}{\partial x_j} \left[(\mu + \sigma_\kappa \mu_t) \frac{\partial \kappa}{\partial x_j} \right] \quad (2.116)$$

$$\begin{aligned} \frac{\partial(\rho\omega)}{\partial t} + \frac{\partial(\rho\omega u_j)}{\partial x_j} &= \gamma \frac{\rho}{\mu_t} \tau_{ij} \frac{\partial u_i}{\partial x_j} - \beta \rho \omega^2 + \frac{\partial}{\partial x_j} \left[(\mu + \sigma_\omega \mu_t) \frac{\partial \omega}{\partial x_j} \right] \\ &+ 2(1 - F_1) \rho \sigma_{\omega_2} \frac{1}{\omega} \frac{\partial \kappa}{\partial x_j} \frac{\partial \omega}{\partial x_j} \end{aligned} \quad (2.117)$$

where each constant is calculated as

$$\phi = F_1\phi_1 + (1 - F_1)\phi_2 \quad (2.118)$$

The values of the constants are:

- for the inner zone (κ - ω type)

$$\sigma_{\kappa_1} = 0.85 \quad \sigma_{\omega_1} = 0.5 \quad \beta_1 = 0.075 \quad (2.119)$$

- for the outer zone (κ - ε type)

$$\sigma_{\kappa_2} = 1.0 \quad \sigma_{\omega_2} = 0.856 \quad \beta_2 = 0.0828 \quad (2.120)$$

and

$$\beta^* = 0.09 \quad \gamma_{1,2} = \frac{\beta_{1,2}}{\beta^*} - \frac{\sigma_{\omega_{1,2}}\kappa_a^2}{\sqrt{\beta^*}} \quad (2.121)$$

The blending function F_1 is computed as

$$F_1 = \tanh(\text{arg}_1^4) \quad (2.122)$$

with

$$\text{arg}_1 = \text{Min} \left[\text{Max} \left(\frac{\sqrt{\kappa}}{0.09\omega y}, \frac{500\nu}{\omega y^2} \right), \frac{4\rho\sigma_{\omega_2}\kappa}{CD_{\kappa\omega}y^2} \right] \quad (2.123)$$

and

$$CD_{\kappa\omega} = \text{Max} \left[2\rho\sigma_{\omega_2} \frac{1}{\omega} \frac{\partial\kappa}{\partial x_j} \frac{\partial\omega}{\partial x_j}, 10^{-20} \right] \quad (2.124)$$

In the (2.123) the first argument represents the turbulent length scale $L_t = \sqrt{\kappa}/(\beta^*\omega)$ divided by the shortest distance to the next surface, the second term becomes important in the viscous sublayer and ensures that F_1 does not go to zero in that region, while the last term prevents a possible free stream dependence of the κ - ω type solution.

In order to improve the simulation of adverse pressure gradient flows, the effect of the transport of the principal shear stress ($\tau_{xy} = -\rho\overline{u'v'}$) has been included in the definition of the eddy viscosity. Following the Bradshaw's

assumption, employed also by the Johnson-King model, τ_{xy} is assumed to be proportional, in the boundary layer, to the turbulent kinetic energy

$$\tau_{xy} = \rho a_1 \kappa \quad (2.125)$$

where a_1 is a constant.

In a two equation model, the shear stress is usually computed by means of the vorticity

$$\tau_{xy} = \mu_t \Omega \quad (2.126)$$

a relation that, if the eddy viscosity is expressed by the (2.63), can be also written as

$$\tau_{xy} = \rho \sqrt{\frac{P_\kappa}{D_\kappa}} a_1 \kappa \quad (2.127)$$

where P_κ and D_κ represent the production and the destruction of κ respectively.

The ratio P_κ/D_κ can be significantly greater than one in adverse pressure gradient flows. Therefore, the equation (2.127) could lead to an overprediction of τ_{xy} unless the eddy viscosity is defined as follows

$$\mu_t = \rho \frac{a_1 \kappa}{\Omega} \quad (2.128)$$

However the following expression

$$\mu_t = \rho \frac{a_1 \kappa}{\text{Max}(a_1 \omega, \Omega)} \quad (2.129)$$

is employed instead of the (2.128). In fact, the equation (2.128) cannot be used in the complete flow field because there are points where Ω goes to zero. The (2.129) guarantees the use of equation (2.128) for most of the adverse pressure gradient regions where $\Omega > a_1 \omega$, and of equation (2.63) for the rest of the boundary layer. Nevertheless, in order to recover the (2.63) for free shear layer flows, where the relation (2.125) does not necessarily hold, a blending function, that limits the use of Ω only to wall bounded flows, has been included in the 2.129.

Finally the eddy viscosity is written as

$$\mu_T = \frac{\rho a_1 \kappa}{\text{Max}(a_1 \omega, \Omega F_2)} \quad (2.130)$$

with $a_1 = 0.31$, and the blending function F_2 evaluated as

$$F_2 = \tanh(\text{arg}_2^2) \quad (2.131)$$

with

$$\text{arg}_2 = \text{Max} \left[2 \frac{\sqrt{\kappa}}{0.09\omega y}, \frac{500\nu}{\omega y^2} \right] \quad (2.132)$$

The function F_2 has been designed to be 1 close to solid boundaries and 0 in the upper part of the logarithmic region of a turbulent boundary layer where Eq. (2.125) should be recovered.

The κ - ω Shear Stress Transport (SST) model has been successively applied in a wide range of applications, and is regarded in the aeronautical community as the best linear two equation model for compressible external aerodynamics [36, 37].

2.2.3 ZEN Code

The flow solver adopted for the RANS simulations is a multi-block well assessed tool for the analysis of complex configurations in the subsonic, transonic, and supersonic regimes [21, 38]. The equations are discretized by means of a standard cell-centered finite volume scheme with blended self adaptive second and fourth order artificial dissipation. The pseudo time-marching advancement is performed by using the Runge-Kutta algorithm with convergence accelerators such as the multi-grid and residual smoothing techniques.

The turbulence equations are weakly coupled with the RANS equations and solved only on the finest grid level of a multi-grid cycle. Algebraic, one-equation, two-equations [39], and non linear eddy viscosity turbulence models [40] are available.

2.2.3.1 Numerical definition

The Navier-Stokes equations (2.1), after applying the Gauss theorem, are written for each cell (i, j, k) of a computational domain as

$$\frac{d}{dt} \int_{V_{ijk}} U_{ijk} dV_{ijk} + \int_{\partial V_{ijk}} (F^c - F^v) dS_{ijk} = \int_{V_{ijk}} Q dV_{ijk} \quad (2.133)$$

where U is the vector of the unknown variables, F^c is the convective flux, F^v the viscous (physical and artificial) flux, and Q stands for the source term (if any). The volume of the computational cell is V_{ijk} .

The (2.133), by means of a cell centered finite volume approach, reduce to

$$V_{ijk} \frac{dU_{ijk}}{dt} + R_{ijk}^c - R_{ijk}^v - V_{ijk} Q_{ijk} = 0 \quad (2.134)$$

with R^c and R^v the total net fluxes (convective and viscous respectively) positive if outgoing from the volume V_{ijk} .

The residual R_{ijk}^c is obtained as the sum of the fluxes across the six faces of the cell (i, j, k)

$$R_{ijk}^c = f_{i+1/2} - f_{i-1/2} + f_{j+1/2} - f_{j-1/2} + f_{k+1/2} - f_{k-1/2} \quad (2.135)$$

At the interface $i + 1/2$ of the cell (i, j, k) , the flux $f_{i+1/2}$, positive if outgoing from the volume V_{ijk} , is evaluated as

$$f_{i+1/2} = \begin{cases} q_{i+1/2} \rho_{i+1/2} \\ q_{i+1/2} (\rho u)_{i+1/2} + p_{i+1/2} A_{i+1/2} \\ q_{i+1/2} H_{i+1/2} \end{cases} \quad (2.136)$$

where $\rho_{i+1/2}$ is the density, $p_{i+1/2}$ the thermodynamic pressure, $(\rho u)_{i+1/2}$ the momentum, and $H_{i+1/2}$ the enthalpy evaluated at the cell face by averaging between the values at the centers of the cells (i, j, k) and $(i + 1, j, k)$. The volume flux $q_{i+1/2}$ is computed as :

$$q_{i+1/2} = \frac{(\rho u)_{i+1/2} \cdot A_{i+1/2}}{\rho_{i+1/2}} \quad (2.137)$$

where $A_{i+1/2}$ is the area vector of the face $(i + 1/2, j, k)$ pointing in the positive i direction.

The residual R_{ijk}^v is obtained as the sum of the fluxes across the six faces of the cell (i, j, k)

$$R_{ijk}^v = g_{i+1/2} - g_{i-1/2} + g_{j+1/2} - g_{j-1/2} + g_{k+1/2} - g_{k-1/2} \quad (2.138)$$

The generic flux $g_{i+1/2}$ requires, for the momentum equation, the evaluation of the velocities derivatives and of the heat flux for the energy equation.

The derivatives of the velocities are computed by integrating over a cell volume and applying the Gauss theorem. The gradient of the generic velocity component u is obtained as

$$(\nabla u)_{i,j,k} = \frac{1}{V_{i,j,k}} \sum_{f=1}^6 u_f \underline{A}_f \quad (2.139)$$

where u_f is the value of u at the face center, and \underline{A}_f is the area vector of the face. Thus the derivative of u in the x_i direction results to be

$$\begin{aligned} \frac{\partial u}{\partial x_i} = & \frac{1}{V_{i,j,k}} \left(\frac{(u_{i+1,j,k} + u_{i,j,k})}{2} A_{i+1/2,j,k}^{x_i} - \frac{(u_{i,j,k} + u_{i-1,j,k})}{2} A_{i-1/2,j,k}^{x_i} \right. \\ & + \frac{(u_{i,j+1,k} + u_{i,j,k})}{2} A_{i,j+1/2,k}^{x_i} - \frac{(u_{i,j,k} + u_{i,j-1,k})}{2} A_{i,j-1/2,k}^{x_i} \\ & \left. + \frac{(u_{i,j,k+1} + u_{i,j,k})}{2} A_{i,j,k+1/2}^{x_i} - \frac{(u_{i,j,k} + u_{i,j,k-1})}{2} A_{i,j,k-1/2}^{x_i} \right) \end{aligned} \quad (2.140)$$

with $A_{i+1/2,j,k}^{x_i}$ the x_i -component of the area vector of the face $(i + 1/2, j, k)$

$$A_{i+1/2,j,k}^{x_i} = A_{i+1/2,j,k} n_{i+1/2,j,k}^{x_i} \quad (2.141)$$

where $\underline{n}_{i+1/2,j,k}$ is the normal versor of the face.

The heat flux is computed as $(\lambda_{tot})_{i+1/2} (\nabla_i T)_{i+1/2}$ where

$$(\lambda_{tot})_{i+1/2} = \frac{C_p \mu_{i+1/2}}{Pr} + \frac{C_p (\mu_t)_{i+1/2}}{Pr_t} \quad (2.142)$$

is the total heat conduction coefficient with μ the molecular and μ_t the turbulent viscosity and Pr and Pr_t the Prandtl and the turbulent Prandtl number respectively. The molecular and turbulent viscosity are computed by averaging between the cells sharing the considered interface

$$\mu_{i+1/2} = \frac{\mu_{i,j,k} + \mu_{i+1,j,k}}{2} \quad (2.143)$$

$$(\mu_t)_{i+1/2} = \frac{(\mu_t)_{i,j,k} + (\mu_t)_{i+1,j,k}}{2} \quad (2.144)$$

The i component of the gradient of the temperature T is evaluated as

$$(\nabla_i T)_{i+1/2} = \frac{T_{i+1} - T_i}{\Delta L_{i+1/2}} \quad (2.145)$$

where

$$\Delta L_{i+1/2} = \frac{V_{i,j,k} + V_{i+1,j,k}}{2|A_{i+1/2}|} \quad (2.146)$$

with $|A_{i+1/2}|$ the area of the face $(i + 1/2, j, k)$, and $V_{i+1,j,k}$ the volume of the cell $(i + 1, j, k)$.

The equation (2.134) is advanced in time by using a Runge Kutta (RK) algorithm. The m - stage formula, assuming that n is the known time level, is

$$U_{i,j,k}^{(0)} = U_{i,j,k}^{(n)} \quad (2.147)$$

$$(U_{i,j,k}^{(k)} - U_{i,j,k}^{(0)}) = \alpha_k \Delta t_{i,j,k} \left[-\frac{1}{V_{i,j,k}} (R_{i,j,k}^c + R_{i,j,k}^v) + Q_{i,j,k} \right] \quad (2.148)$$

$$U_{i,j,k}^{(n+1)} = U_{i,j,k}^{(m-1)} \quad (2.149)$$

where α_k is the RK coefficient and $\Delta t_{i,j,k}$ is the time step which is evaluated for each grid cell separately. The convective residuals $R_{i,j,k}^c$ are computed at each stage of the procedure, while the terms $R_{i,j,k}^v$ and $Q_{i,j,k}$ are calculated only at the first stage and then are frozen.

The use of a local time step does not influence the steady-state solution, and allows to have, where possible, larger time steps and thus to expel disturbances faster.

2.2.3.2 UZEN: the Time-accurate Version

A time-accurate version of the flow solver has also been developed [41]. The time integration is based on the dual-time stepping method [42] where a pseudo steady-state problem is solved at each physical time step. The DTS considers the residual equations in an implicit way. All the variables are known at time level n , and the equations at the time level $n + 1$ become :

$$L_t \underline{U}^{n+1} = -\underline{\underline{R}}(\underline{U}^{n+1}) \quad (2.150)$$

where L_t is the time derivative operator, and

$$\underline{\underline{R}} = \underline{\underline{R}}^C + \underline{\underline{R}}^V \quad (2.151)$$

is the sum of the convective and viscous (physical and artificial) fluxes.

A second order backward difference formula is applied for the time discretization :

$$L_t \underline{U}^{n+1} = \frac{3\underline{U}^{n+1} - 4\underline{U}^n + \underline{U}^{n-1}}{2 \Delta t} \quad (2.152)$$

At each physical time level, the DTS method considers a new residual :

$$\underline{\underline{\tilde{R}}}(\underline{U}) = \underline{\underline{R}}(\underline{U}) + \frac{3\underline{U}^{n+1} - 4\underline{U}^n + \underline{U}^{n-1}}{2 \Delta t} \quad (2.153)$$

and the following equation

$$\frac{d\underline{U}}{d\tau} = -\underline{\underline{\tilde{R}}}(\underline{U}) \quad (2.154)$$

is solved in the dual-time τ . The integration of equation (2.154) to its steady state provides the solution of equation (2.152); the flow variables \underline{U} at the time level $n + 1$.

2.3 Detached Eddy Simulation

The detached eddy simulation belongs to the class of numerical techniques named hybrid LES-RANS. The accuracy of LES is tried to be achieved at a lower computational cost exploiting a RANS approach in the zone of the flow field where the boundary layer is expected to stay attached to the body. The LES approach should be applied only in the zone of separated flow.

The detached eddy simulation based on the Spalart-Allmaras and κ - ω SST models is implemented in the UZEN code [43]

2.3.1 SA-DES

The Detached Eddy Simulation was proposed by Shur and Spalart [44] by re-defining the length scale of the Spalart Allmaras model (Eq. 2.43). The

equilibrium hypothesis applied to the model reads as

$$C_{b1}\tilde{S}\tilde{\nu} = C_{w1}\left(\frac{\tilde{\nu}}{\tilde{d}}\right)^2 \quad (2.155)$$

and hence

$$\tilde{\nu} \approx \tilde{S}\tilde{d}^2 \quad (2.156)$$

The comparison of the above relation with the equation (2.17) shows that a Smagorinsky-like form of the model can be achieved by posing $\tilde{d} = C_S\Delta$. The DES version of the Spalart-Allmaras turbulence model is achieved by defining a length scale as

$$\tilde{d} = \text{Min}(d, C_{DES}\Delta) \quad (2.157)$$

where d is the distance from a solid boundary, $C_{DES} = 0.65$, and Δ has to be considered as the maximum local grid spacing

$$\Delta = \text{Max}(\Delta x, \Delta y, \Delta z) \quad (2.158)$$

2.3.2 SST-DES

The DES approach consists of multiplying the dissipation term of equation (2.64) by

$$F_{DES} = \text{Max}\left[\frac{L_t}{C_{DES}\Delta}(1 - F_2), 1\right] \quad (2.159)$$

where $L_t = \frac{\sqrt{\kappa}}{\beta^*\omega}$ is the turbulent length scale. The constant C_{DES} is computed, following equation (2.118), as

$$C_{DES} = F_1 C_{DES}^{\kappa\omega} + (1 - F_1) C_{DES}^{\kappa\varepsilon} \quad (2.160)$$

with $C_{DES}^{\kappa\omega} = 0.78$ and $C_{DES}^{\kappa\varepsilon} = 0.61$

Laminar Separation Bubbles

Flows at low Reynolds number are not able to sustain strong adverse pressure gradients and often separate in laminar flow regime. The turbulence developing inside the re-circulation region enhances the momentum transport, and the flow re-attaches. A laminar separation bubble (LSB) is formed. A sketch of the typical structure of a LSB is shown in figure 3.1. A large part of the

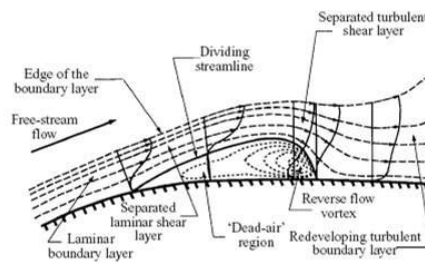


Figure 3.1: Structure of a laminar separation bubble, from Horton [45]

separated zone is characterized by a slow flow motion. This is named as *dead-air* region. The last part of the bubble presents a strong re-circulation vortex flow. Looking at the path of the dividing stream-line, it is clear that a sudden pressure recovery leading to the re-attachment of the flow occurs in this zone.

The capability of the RANS models to predict a laminar separation bubble is discussed in this chapter. The presence in the flow field of laminar separation bubbles means that the transition points cannot be set *a priori*. This is a critical point for the turbulence models that are calibrated for

separation in the turbulent flow regime, and need the transition points to be known. This issue has been addressed performing numerical simulations without specifying the transition location and using low values of the free-stream turbulence [46].

The first test-case discussed is the flow over a flat plate with an imposed pressure gradient. The results obtained by applying the ZEN code are compared to experimental [47] and DNS [48] data found in literature. Then the flow at Reynolds number 6.0×10^4 around the Selig-Donovan 7003 is taken into consideration. RANS and large eddy simulations have been performed and compared to experimental [49] and other numerical results [18].

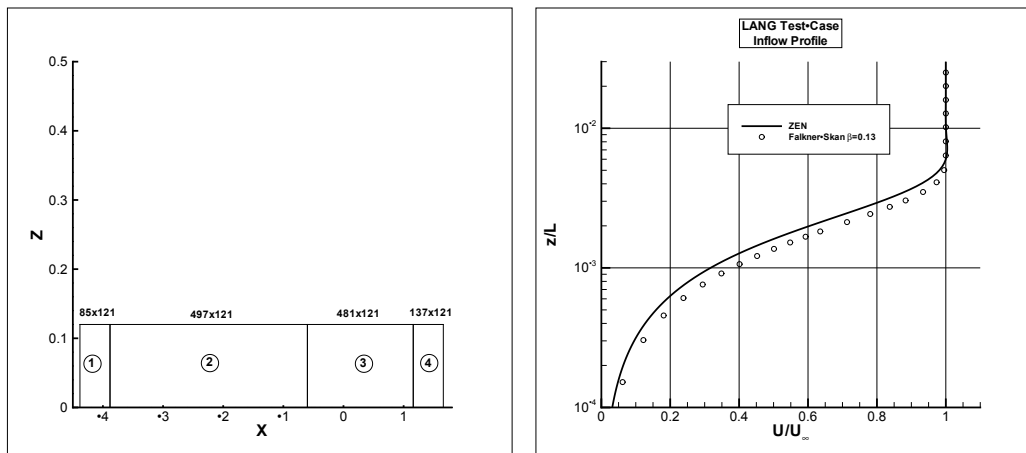
3.1 Flow over a Flat Plate

A flat plate is mounted in the laminar water tunnel of the Institute of Aerodynamics and Gasdynamics of University of Stuttgart [48, 47]. A pressure gradient is imposed by means of a body located at the upper boundary of the experimental apparatus. The free-stream velocity V_∞ is 0.125 m/s , and the viscosity ν is $1 \times 10^{-6} \text{ m}^2/\text{s}$. The resulting Reynolds number is about 1×10^5 . At the inflow, the measured velocity profile can be approximated by a Falkner-Skan solution with a Reynolds number based on the displacement thickness Re_{δ^*} of 900 and a Hartree parameter β of 0.13.

3.1.1 Numerical Set-up

A computational grid composed of 4 domains has been employed (figure 3.2a). The first and fourth block do not have any wall, while the second and third block have a solid boundary. The second domain is adopted to set up the velocity at the inflow of the third block that corresponds to the experimental flat plate. A laminar boundary layer develops in the second computational domain for a length

$$L_{\delta^*} = \left(\frac{Re_{\delta^*}}{C_1} \right)^2 \frac{\nu}{V_\infty} \quad (3.1)$$



(a) Computational Domain for the LSB over a Flat Plate. For each block the number of points is reported
 (b) Stream-wise velocity profile at the inflow boundary of the domain of interest

Figure 3.2: Numerical Set-up for the LSB over a Flat Plate.

obtained considering that

$$Re_{\delta^*} = C_1 \sqrt{\frac{V_\infty}{\nu}} L_{\delta^*} \quad C_1 = 1.7208 \quad (3.2)$$

The stream-wise velocity obtained numerically at the inflow of the domain of interest matches the experimental data (figure 3.2b).

This numerical set-up has been verified by considering the flow over the flat plate without an imposed pressure gradient. The ZEN code has been applied to simulate a laminar flow with a Reynolds number based on the length of the second and third domain of 4.935×10^5 . At the inflow boundary, free-stream conditions are imposed for the velocity components and density while the pressure is extrapolated from the interior. At the outflow boundary all the fluid dynamic variables are extrapolated. The friction coefficient compares very well with the Blasius curve [50] as shown in figure 3.3. The stream-wise and normal-wise components of the velocity are presented as functions of the self-similar coordinate $\eta = z \sqrt{\frac{u_\infty}{\nu x}}$ in figure 3.4. The velocities obtained at different locations x/L collapse in a unique plot in excellent agreement with the Blasius solution.

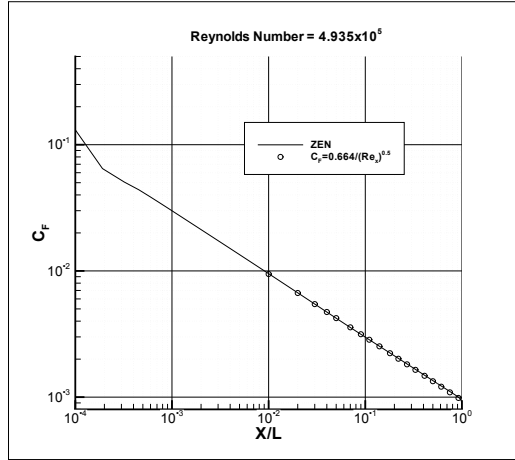
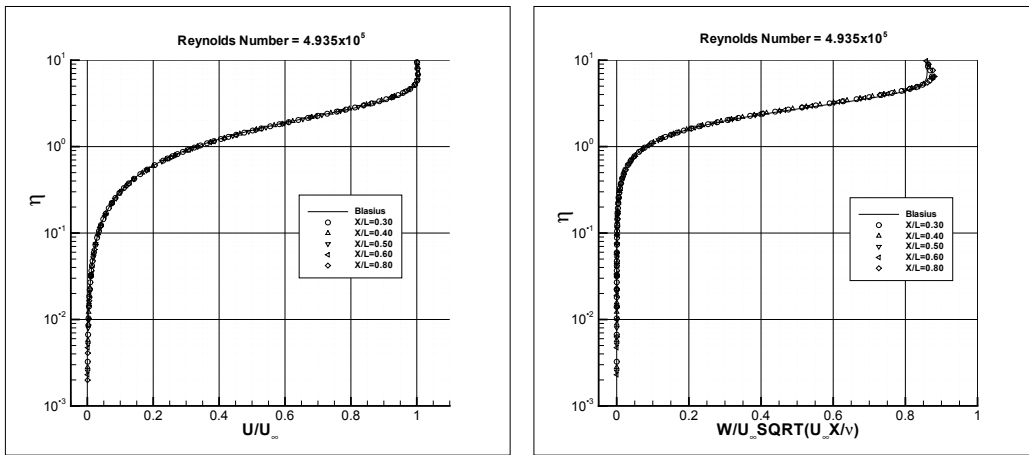


Figure 3.3: Laminar flow over a flat plate : Friction Coefficient



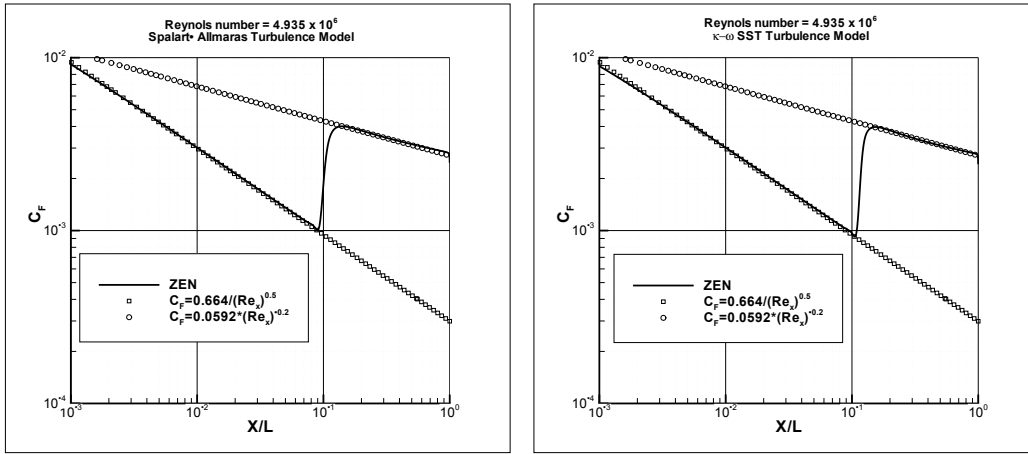
(a) Stream-wise velocity

(b) Normal-wise velocity

Figure 3.4: Laminar flow over a flat plate: Velocity profiles

The next step has been to increase the Reynolds number of an order of magnitude and simulate the flow imposing the transition at $x/L = 0.1$. The height of the wall-adjacent cells has been decreased with respect to the case at $Re = 4.935 \times 10^5$. The Spalart-Allmaras and the $\kappa\text{-}\omega$ SST turbulence models have been employed. The friction coefficient is shown in figure 3.5. The Blasius laminar and Prandtl turbulent curves [50] are reproduced very well.

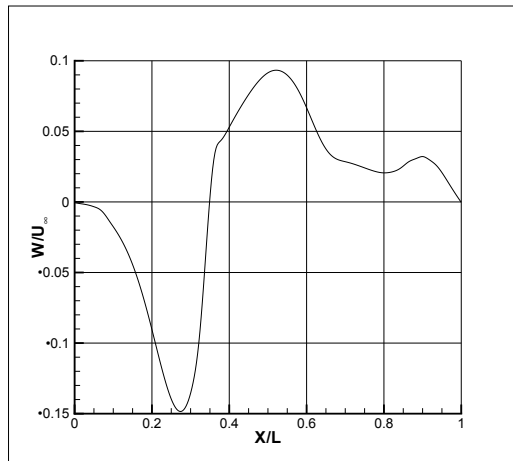
The experiment performed at the University of Stuttgart [48, 47] has been



(a) Spalart-Allmaras

 (b) κ - ω SST

Figure 3.5: Transitional Flow over a flat plate: Friction Coefficient

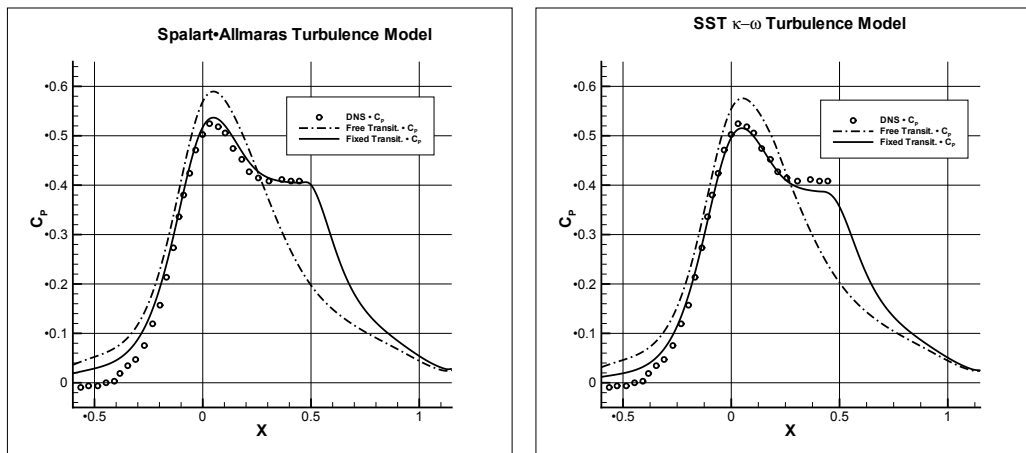


(a)

Figure 3.6: Normal-wise velocity profile at the top boundary of the domain of interest

simulated by adopting the numerical set-up described above. A pressure gradient is imposed at the top boundary of the 3rd computational domain (figure 3.2a) by prescribing a normal-wise velocity as come out by DNS data (figure 3.6). The following boundary condition has been implemented

$$w < 0 \Rightarrow \begin{cases} u & v & w & \rho & \text{imposed} \\ p & & & & \text{extrapolated} \end{cases} \quad w > 0 \Rightarrow \begin{cases} w & \text{imposed} \\ u & v & \rho & p & \text{extrapolated} \end{cases}$$



(a) Spalart-Allmaras

(b) κ - ω SST

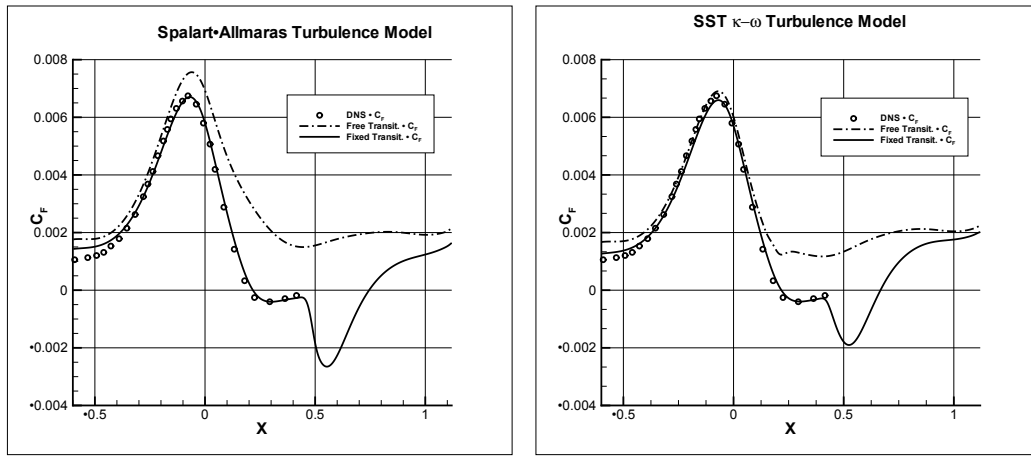
Figure 3.7: LSB over a Flat Plate : Pressure Coefficient. Effect of imposing transition point

3.1.2 Influence of free-stream Turbulence

The transition of the flow from the laminar to the turbulent regime is a critical point in reproducing laminar separation bubbles. This is shown in figures 3.7 and 3.8 where the pressure and friction coefficients achieved by the Spalart-Allmaras and κ - ω SST turbulence models with standard inputs are reported. It is clearly seen that only imposing the transition point, the flow separates and a laminar bubble is formed. No separation occurs if the turbulence models are run in a "fully turbulent" way without specifying the transition location.

Some researchers have coupled transition prediction methods to RANS solvers in order to simulate laminar bubbles [10, 11, 12].

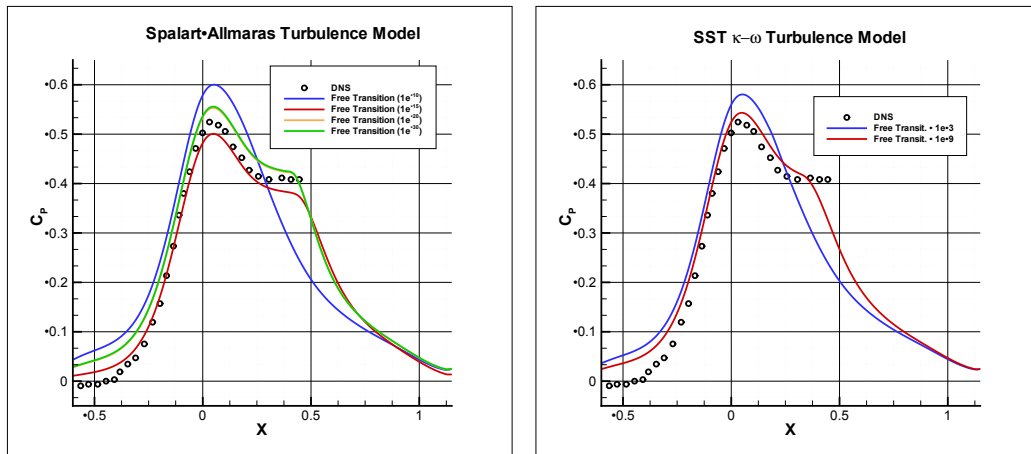
An other way has been tried [46]. Indeed laminar bubbles are found if the turbulence models are run with low values of the free-stream turbulent variables. No particular treatment of the transition mechanism is employed. The figures 3.9 and 3.10 show the pressure and friction coefficients achieved by lowering the free-stream values of the turbulent variables (the ratio $\frac{\tilde{\nu}}{\nu}$ for the Spalart Allmaras; $\frac{\mu_t}{\mu}$, and $\frac{\sqrt{\kappa}}{V}$ for the κ - ω SST). The RANS results are compared to DNS [48] data in the laminar part of the bubble. The



(a) Spalart-Allmaras

(b) $\kappa\text{-}\omega$ SST

Figure 3.8: LSB over a Flat Plate : Friction Coefficient. Effect of imposing transition point



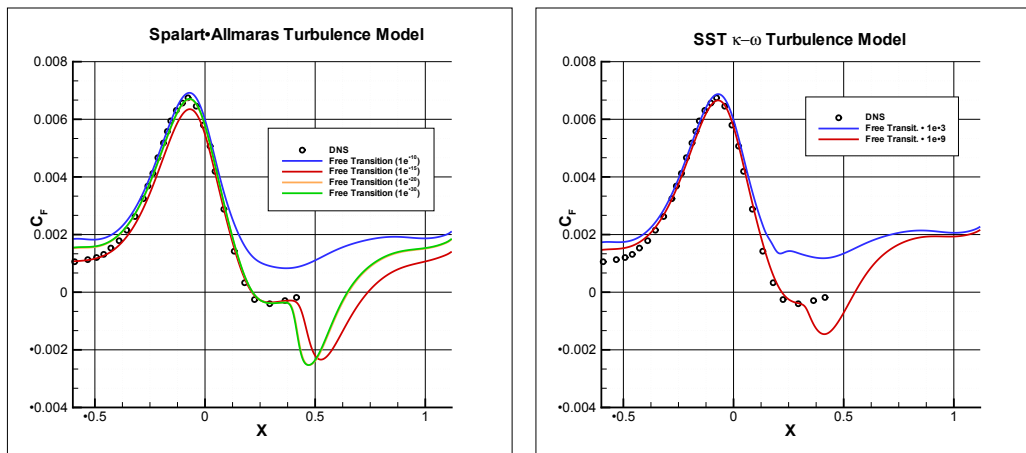
(a) Spalart-Allmaras

(b) $\kappa\text{-}\omega$ SST

Figure 3.9: LSB over a Flat Plate : Pressure Coefficient. Effect of lowering free-stream values of the turbulent variables; $\frac{\tilde{\nu}}{\nu}$ (a); $\frac{\mu_t}{\mu}$ (b)

re-attachment of the flow provided by the DNS is at $x = 0.6$.

The bubble is found if the free-stream values are sufficiently low. The Spalart-Allmaras (figures 3.9a, and 3.10a) returns a bubble if $\frac{\tilde{\nu}}{\nu}|_{\infty} \leq 1 \times 10^{-15}$ with the results obtained with $\frac{\tilde{\nu}}{\nu}|_{\infty} = 1 \times 10^{-20}$ and $\frac{\tilde{\nu}}{\nu}|_{\infty} = 1 \times 10^{-30}$ almost indistinguishable. All the simulations with bubble show the same separation



(a) Spalart-Allmaras

 (b) κ - ω SST

Figure 3.10: LSB over a Flat Plate : Friction Coefficient. Effect of lowering free-stream values of the turbulent variables; $\frac{\tilde{\nu}}{\nu}$ (a); $\frac{\mu_t}{\mu}$ (b)

point as the DNS. The simulation with $\frac{\tilde{\nu}}{\nu}|_{\infty} \leq 1 \times 10^{-15}$ follows better the C_F in the "dead air" region but gives a re-attachment point located more downstream than DNS data. The computation with $\frac{\tilde{\nu}}{\nu}|_{\infty} \leq 1 \times 10^{-20}$ provides a dead-air region shorter with respect to DNS but the length of the bubble is well reproduced.

The $\kappa - \omega$ SST model (figures 3.9b, and 3.10b), with difference to what found by Spalart [4], finds a bubble when used with $\frac{\mu_t}{\mu}|_{\infty} = 1 \times 10^{-9}$, and $\frac{\sqrt{\kappa}}{V}|_{\infty} = 10^{-6}$. The separation point is well predicted, the transition anticipated and the re-attachment slightly posticipated with respect to DNS.

The effect of lowering the free-stream turbulence has been investigated in more detail. The stream-wise velocity profiles at different locations achieved by the κ - ω SST and Spalart-Allmaras turbulence models are shown in figure 3.11 and 3.12 respectively. Velocities have been obtained by considering different conditions at the top boundary of the computational domain. Solid curves refer to simulations performed by imposing a pressure gradient, as reported in the previous section. The dashed-dot lines are for free-stream condition applied at the top boundary.

Two ways of dealing with the transition phenomenon are reported. Black

3.1 FLOW OVER A FLAT PLATE

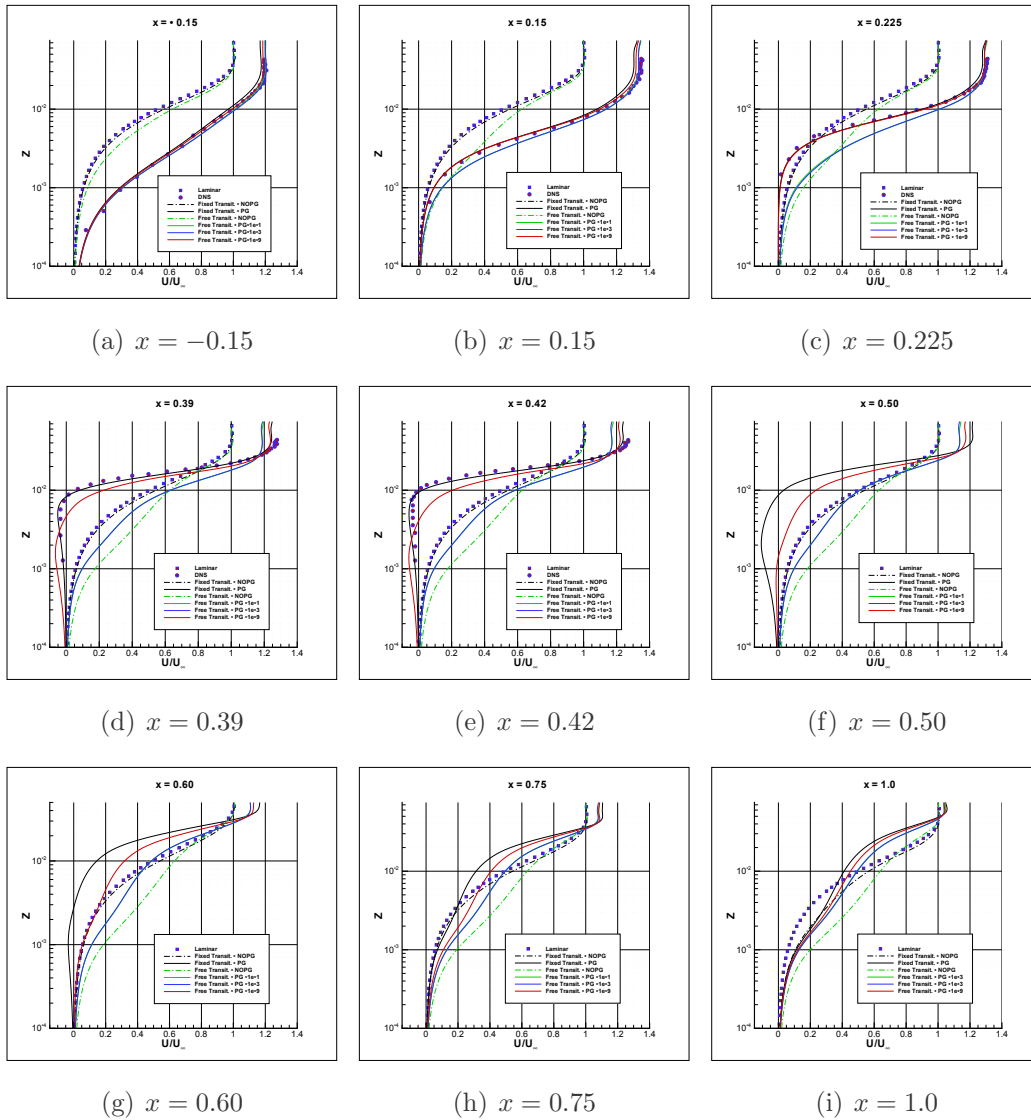


Figure 3.11: LSB over a flat plate - $\kappa - \omega$ SST turbulence model: Influence of free-stream turbulence on stream-wise velocity: — Fixed Transient - PG; - - - Fixed Transient - NOPG; — Free Transient - PG - 1e-1; — Free Transient - PG - 1e-2; — Free Transient - PG - 1e-3

lines are for the runs carried out by prescribing the location of the transition *a priori*, while the results achieved by *fully turbulent* simulations are shown in coloured curves. Decreasing values of the free-stream turbulence are used.

The results obtained with free-stream conditions imposed at the top boundary of the computational domain are compared to the velocities achieved

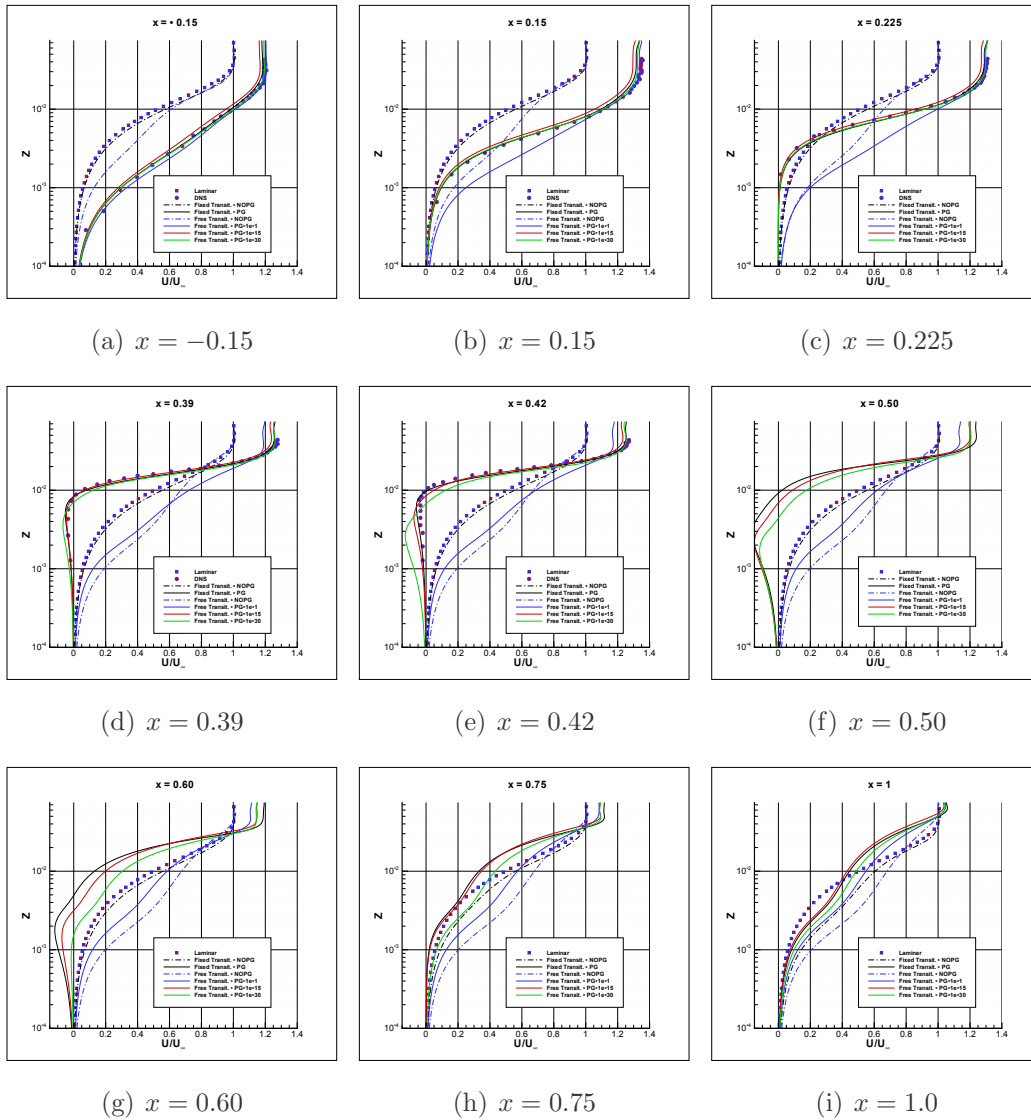


Figure 3.12: LSB over a flat plate - Spalart and Allmaras turbulence model: Influence of free-stream turbulence on stream-wise velocity: —- Pressure gradient; - · - No pressure gradient;

by a laminar simulation. The results of the simulation with an imposed pressure gradient are compared to the DNS data [48] at the stations where these are available.

The results of the simulations performed without an imposed pressure gradient and using *standard* value of the free-stream turbulence are first ana-

lyzed. Both the Spalart-Allmaras and the κ - ω SST turbulence models return the same kind of results. The flow obtained in case of prescribed transition location (at $x = 0.42$) remains in the laminar regime up to the transition point. In fact, it is possible to note from both figure 3.11 and 3.12, how the velocity profiles (black dash-dotted curves) compare with the laminar solution (square symbols) very well. A turbulent flow develops only downstream the transition location. Instead in case of simulation without fixing the transition location, the velocity profiles (green dash-dotted curves) do not follow the laminar solution (square symbol) showing a logarithmic turbulent region already at $x = 0.15$.

The simulations with an imposed pressure gradient have been performed by prescribing the transition location and by assuming the flow turbulent everywhere with decreasing values of the free-stream turbulence.

Different solutions corresponding to the free-stream ratio $\frac{\mu_t}{\mu}$ have been computed by applying the κ - ω SST model as shown in figure 3.11. The results obtained by imposing the transition (black solid curves) reproduce the DNS data very well. At the first station (figure 3.11a), all the velocity profiles achieved without fixing the transition location (coloured solid curves) follow the DNS data. The situation changes as the flow develops along the flat plate. Only the results achieved by using $\frac{\mu_t}{\mu}|_{\infty} = 1 \times 10^{-9}$ (red solid curve) follow the DNS data at $x = 0.15$ and provide a separation at $x = 0.225$. Downstream the separation point, the velocity obtained by prescribing the transition is still in good agreement with the DNS data. Instead the simulation with $\frac{\mu_t}{\mu}|_{\infty} = 1 \times 10^{-9}$ shows a velocity with some disagreement and provides a re-attachment anticipated with respect to the computation with the transition point fixed. The other simulations return a flow that develops a turbulent region upstream of the transition location and do not show any separation.

The results achieved by the Spalart-Allmaras turbulence model are reported in figure 3.12. The solution with the pressure gradient and fully turbulent conditions are obtained with decreasing value of the free-stream ratio $\frac{\tilde{\nu}}{\nu}$. The velocity corresponding to the value $\frac{\tilde{\nu}}{\nu}|_{\infty} = 0.1$ shows a turbulent flow and does not return a separation. The solution obtained with

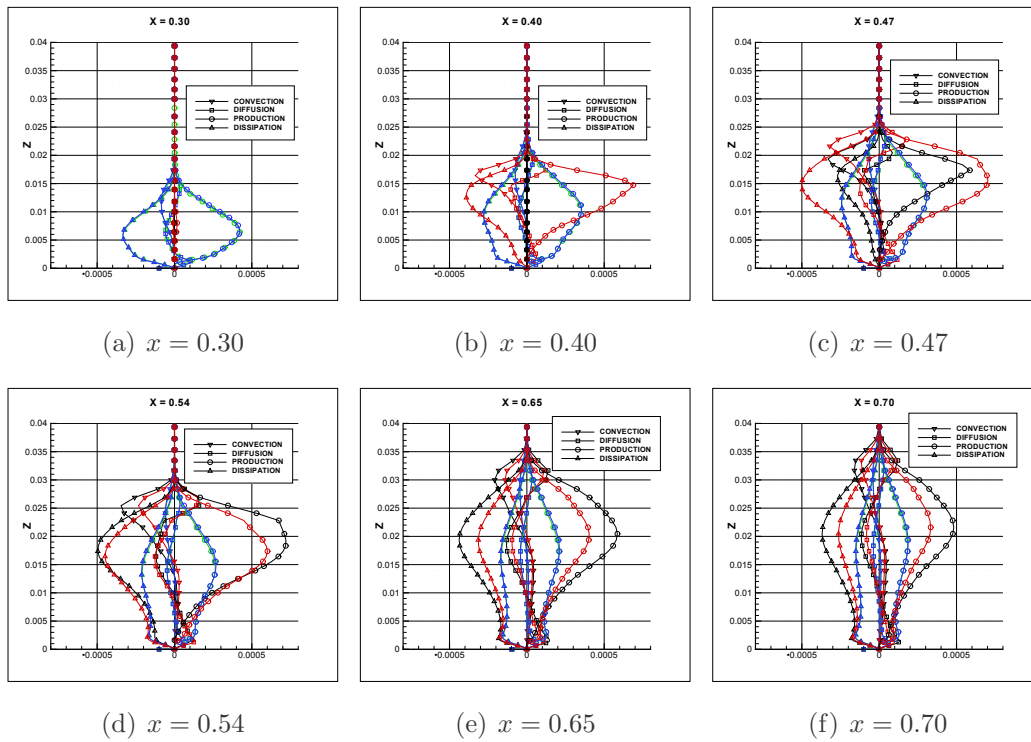


Figure 3.13: LSB over a flat plate: Balance of κ . The colours of the curves are the same as in figure 3.11

$\frac{\tilde{\nu}}{\nu}|_{\infty} = 10^{-15}$ follows both the DNS data and the results achieved by imposing the transition location very well. The velocity profile at the separation point ($x = 0.225$) is in excellent agreement with the DNS. The solution with $\frac{\tilde{\nu}}{\nu}|_{\infty} = 10^{-30}$ also shows a flow separation but the agreement with DNS is a little worse.

The budget of the turbulent kinetic energy has been analyzed by considering the different terms, namely convection, diffusion (equation 2.60), production (equation 2.61) and dissipation (equation 2.62), of the transport equation of κ (equation 2.116). The simulations with an imposed pressure gradient, already evaluated in terms of velocity profiles, are reported in figure (3.13).

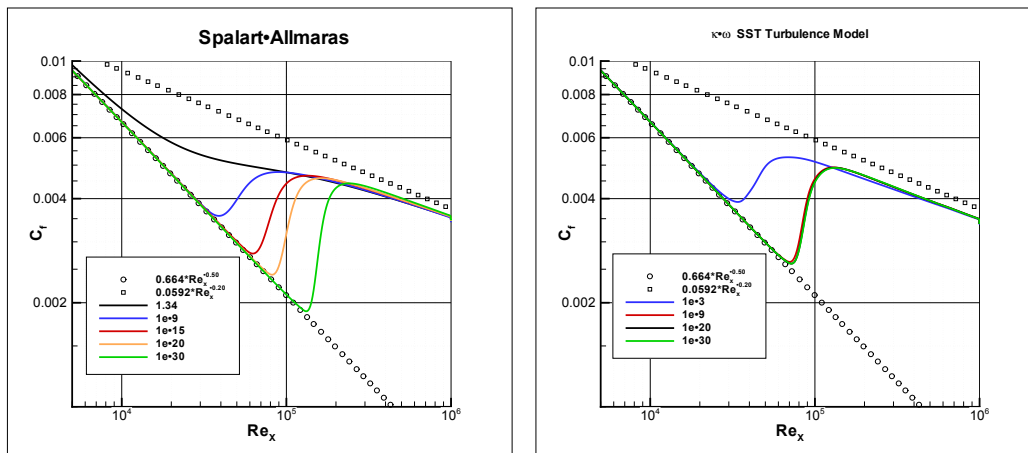
The first station (figure 3.13a) is located well upstream of the separation. The terms of the κ equation are different from zero only for the simulations performed with $\frac{\mu_t}{\mu}|_{\infty} = 1 \times 10^{-1}$ (green curve) and 10^{-3} (blue curve).

At $x = 0.40$ (figure 3.13b), the flow is approaching the transition (occurring at $x = 0.42$). The terms provided by the computation with $\frac{\mu_t}{\mu}|_\infty = 1 \times 10^{-9}$ become active and result larger than the ones provided by the other two simulations performed without imposing the transition location. At the station $x = 0.47$ (figure 3.13c), located downstream the transition point, also the simulation performed with the transition prescribed (black curve) has all the terms that contribute to the balance of κ . The results of the computations with $\frac{\mu_t}{\mu}|_\infty = 1 \times 10^{-1}$ and 10^{-3} are quite similar. The production and dissipation obtained by fixing the transition point become larger (in absolute value) than all the other simulations and resemble the ones obtained with $\frac{\mu_t}{\mu}|_\infty = 1 \times 10^{-9}$. The convection achieved by fixing the transition is similar to the convection obtained with $\frac{\mu_t}{\mu}|_\infty = 1 \times 10^{-9}$ in the inner part of the boundary layer while becomes larger in the outer part. Instead, the diffusion, both molecular and turbulent, resulting by the two simulation is very similar.

In all the simulations, the diffusion is positive close to the wall and in the last part of the boundary layer, while gives a negative contribution in the central region. Convection is first positive and then becomes negative. Production and dissipation are the terms that mainly contribute to the budget of κ in the outer part of the boundary layer.

The results reported in the figures (3.11)-(3.13) show that in case of simulations with the transition point prescribed, the flow remain in the laminar regime upstream of the transition and that the terms of the transport equation of κ are activated only downstream the transition. The use of low values of free-stream turbulence do not reproduce exactly the results achieved by fixing the transition *a priori* but allows to obtain a solution that resembles quite well a laminar flow upstream the actual transition. The Spalart-Allmaras has provided results better than the κ - ω SST turbulence model.

The analysis of the budget of the turbulent kinetic energy at different stations along the flat plate, has highlighted that the production of κ resulting from the computation with low value of $\frac{\mu_t}{\mu}|_\infty$ becomes different from zero a little upstream of the transition point. However the terms concurring



(a) Spalart-Allmaras

(b) $\kappa-\omega$ SST

Figure 3.14: Incompressible flow over a flat plate : Friction Coefficient. Effect of lowering free-stream values of the turbulent variables; $\frac{\tilde{\nu}}{\nu}$ (a); $\frac{\mu_t}{\mu}$ (b)

to the budget of κ obtained by fixing the transition point are similar, also from a quantitative point of view, to the ones resulting from the simulation performed with low values of free-stream turbulence for all the length of the flat plate.

The behaviour of the turbulence models when run with very low values of the turbulent variables has been further investigated by simulating the flow over a flat plate at $Re_L = 1 \times 10^6$.

A sort of numerical transition is shown. The friction coefficient is reported in figure 3.14 together with the Blasius and the Prandtl curves [50]. The Spalart-Allmaras model provides a jump from the laminar to the Prandtl curve if the ratio $(\frac{\tilde{\nu}}{\nu})|_{\infty}$ is kept low. This jump occurs at higher Reynolds number as this ratio decreases. A sort of convergence as the free-stream values are lowered is instead shown by the $\kappa-\omega$ SST model. The jump occurs at a Reynolds number of about 1×10^5 . Both the models slightly underpredict the Prandtl curve.

3.2 Flow around the SD 7003 Airfoil

The laminar separation bubble over an airfoil has been analyzed. The incompressible flow around the Selig-Donovan (SD) 7003 airfoil presents interesting characteristics. At Reynolds number 6×10^4 a bubble is formed on the upper surface of the airfoil. The bubble is located in the rear zone close to the trailing edge at low incidences, and moves upstream as the angle of attack increases.

This is a widely-used test case for which experimental [49] and numerical [18] data are available in literature. RANS and large eddy simulations at several angles of incidence have been performed. The main aim is to analyze the limits of the RANS methods by comparison with LES results.

A first set of results have been obtained by running the turbulence models without specifying the transition points (flows is assumed turbulent everywhere). Laminar separation bubbles are detected if the turbulence models are robust enough to be run with very low values of free-stream turbulence. An other set of results are presented by running the turbulence model with the transition location fixed at a point retrieved by the LES data.

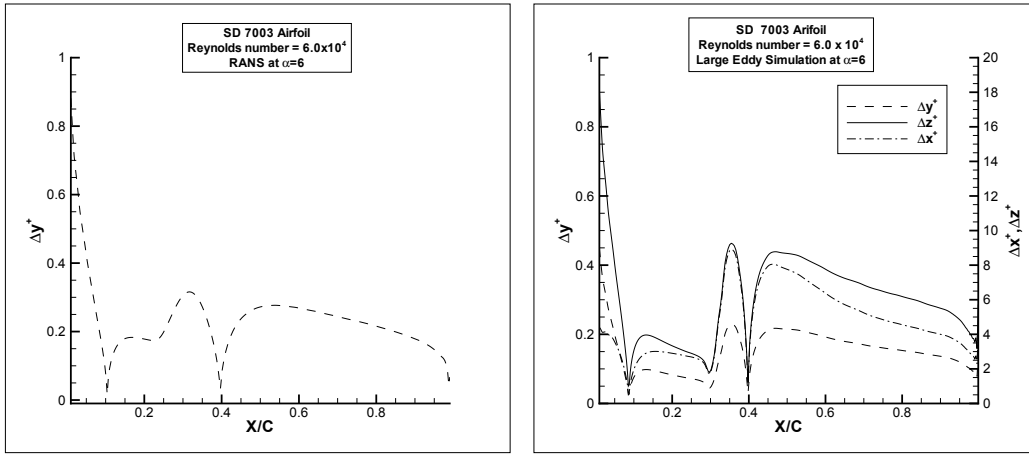
The NEC SX6 machine has been used. A RANS simulation has been obtained in about 8 hours while a LES solution has required about 30 days CPU of a single processor.

3.2.1 Grid Assessment

A C-topology grid with 768 (96 in the wake) cells in the stream-wise and 176 cells in the normal-wise direction has been employed. The far-field boundaries are located at a distance of 30 chords from the airfoil. The height of the wall-adjacent cells in viscous coordinates remains less than one for all the upper surface of the airfoil, as shown in Fig. 3.15a where the y^+ obtained by the RANS with the $\kappa - \omega$ SST turbulence model is presented.

The 2D mesh of the RANS computations has also been employed for the large eddy simulations. The only difference is that the branch-cut line is adapted with the angle of attack to follow the wake. The span-wise extension

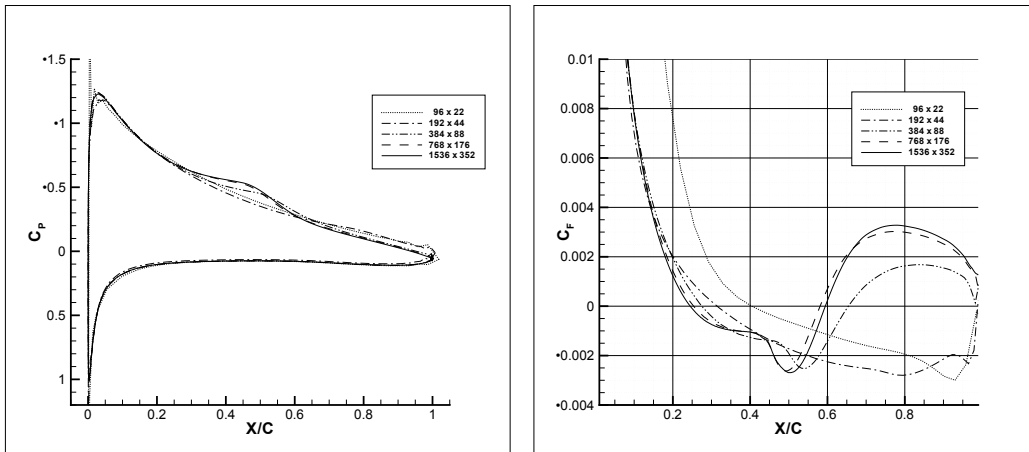
3.2 FLOW AROUND THE SD 7003 AIRFOIL



(a) RANS

(b) LES

Figure 3.15: SD7003 Airfoil, $Re = 6 \times 10^4$, $\alpha = 6^\circ$. Size of wall-adjacent grid cells; $--$: Δy^+ , $—$: Δz^+ , $- \cdot -$: Δx^+



(a) Pressure Coefficient

(b) Friction Coefficient

Figure 3.16: SD7003 Airfoil, $Re = 6.0 \times 10^4$, $\alpha = 4^\circ$. Grid convergence study of the RANS solution

of the computational domain is $0.1 \times c$ with 48 cells. The wall-adjacent cells in viscous coordinates have size less than one in the wall-normal direction, and order of magnitude 10 in the stream and span-wise directions (Fig. 3.15b).

A grid convergence study (Fig. 3.16) has been performed for the RANS solutions. Five levels of the computational mesh are considered. The two

coarsest grids provide a separated flow. The flow re-attaches in the three finer meshes with the re-attachment point between the 50% and 60% of the chord. Differences between the 4th and 5th level of the grid are negligible for both pressure (Fig. 3.16a) and friction coefficient (Fig. 3.16b). Therefore 4 levels of the grid are considered sufficiently accurate, and have been used in the simulations discussed in the following sections.

3.2.2 Turbulence Models Assessment

RANS simulations of the flow at $Re = 6 \times 10^4$ and $\alpha = 4^\circ$ around the SD 7003 airfoil have been performed by using several turbulence models. The transition is not specified and the flow is assumed to be turbulent everywhere. The Spalart-Allmaras [5], the $\kappa - \varepsilon$ Myong-Kasagi [51], and the $\kappa - \omega$ Wilcox [30], TNT [34], BSL, and SST [6] are the models tested. The value of the free-stream turbulence is decreased provided that a converged solution can be achieved. The large eddy simulations by Galbraith and Visbal [18] are taken as reference data.

All the RANS results show a different solution in terms of pressure (Fig. 3.17a and c) and friction coefficient (Fig. 3.17b and d) with respect to LES. The differences are better appreciated looking at the friction coefficient on the upper surface. The $\kappa - \varepsilon$ does not provide a flow separation. A flow with a separation and a re-attachment is returned by all the other turbulence models. The $\kappa - \omega$ SST and the Spalart-Allmaras provide a qualitatively good result. The C_F presents the same shape as LES data although the re-attachment point is anticipated. The $\kappa - \omega$ BSL yields a result in between the TNT and SST models.

3.2.3 Results by κ - ω SST turbulence model

In the following, the focus is placed on the κ - ω SST turbulence model. This model is very popular and reliable for transonic high-Reynolds number flows, as pointed out by different authors (cfr. Catalano and Amato [21, 22], Beazard *et al.* [37]), but its effectiveness for low-Reynolds number flows is doubtful

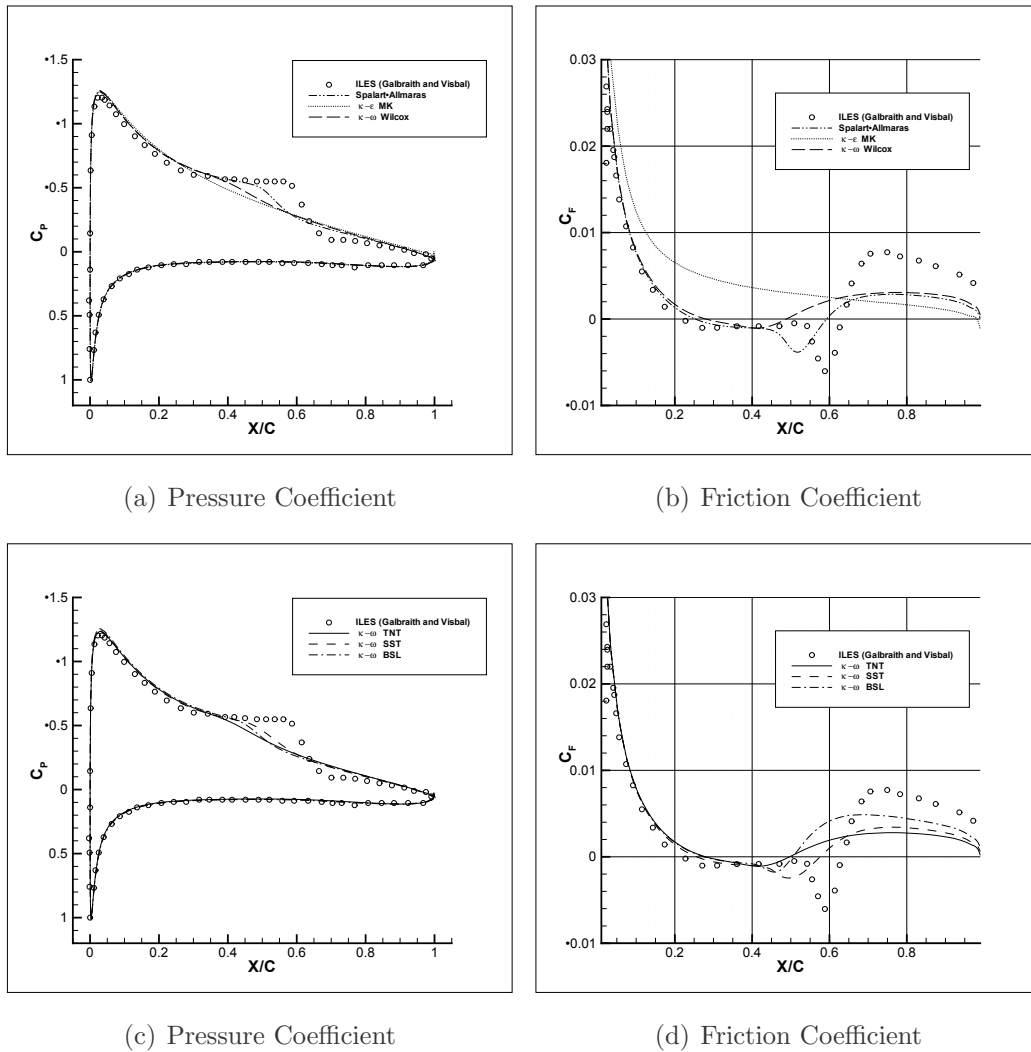


Figure 3.17: SD7003 Airfoil, $Re = 6.0 \times 10^4$, $\alpha = 4^\circ$. Results by several turbulence models

(Catalano and Tognaccini [46], Rumsey and Spalart [19]).

3.2.3.1 Main Characteristics of the Flow

The model is applied at several angles of incidence with $\frac{\mu_t}{\mu} |_\infty = 1 \times 10^{-9}$ and $\frac{\sqrt{k}}{U} |_\infty = 10^{-6}$. The friction and pressure coefficient as function of the angle of attack are presented in Fig. 3.18. A bubble is predicted in the trailing edge zone of the airfoil at $\alpha = 0^\circ$ and then moves towards the leading edge

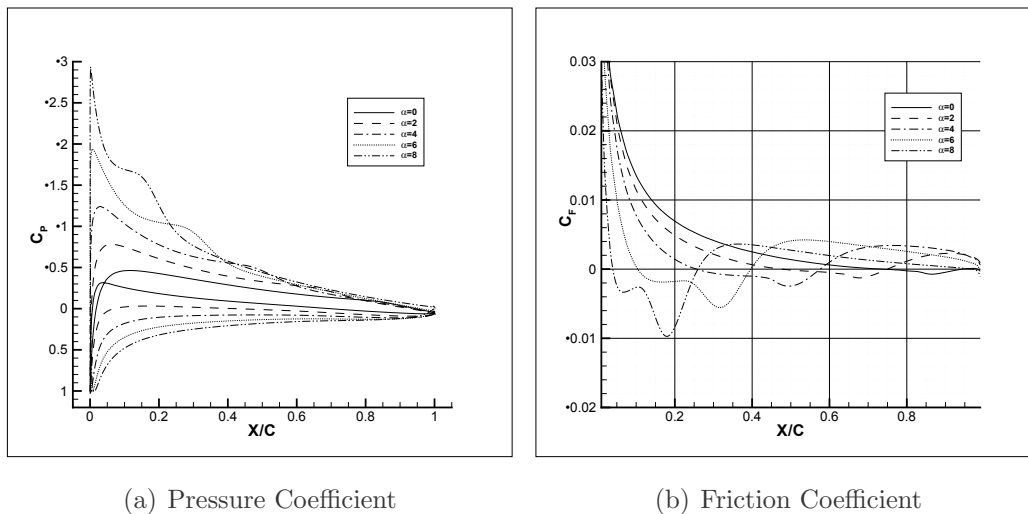


Figure 3.18: SD7003 Airfoil, $Re = 6.0 \times 10^4$. RANS, $\kappa - \omega$ SST with laminar-turbulent transition not prescribed: C_P and C_F over the airfoil at different angles of attack.

as α increases.

The evolution of the laminar bubble as a function of the angle of incidence is also presented in figure 3.19. The contour map of the turbulent kinetic energy shows that the turbulence is formed inside the bubble. The airfoil is stalled at $\alpha = 10^\circ$. This is likely a combined stall due to the interaction between the laminar bubble in the leading edge zone and a separated region appearing in the rear part of the airfoil at the high incidences.

3.2.3.2 Large Eddy Simulations

Large eddy simulations of the flow around the SD 7003 airfoil have been performed at several incidences. A RANS flow field has been used as initial solution and the simulation has been advanced in time with a time step $\Delta t = 1.5 \times 10^{-4}$. Figure 3.20 shows the three-dimensional turbulent flow that develops in the rear part of the airfoil downstream the separation. The time history of the lift and drag coefficients for the case at $\alpha = 4^\circ$ is shown in figure 3.21a and 3.21b. The large eddy simulation has been advanced in time for more than 20 characteristic times, and then the results have been

3.2 FLOW AROUND THE SD 7003 AIRFOIL

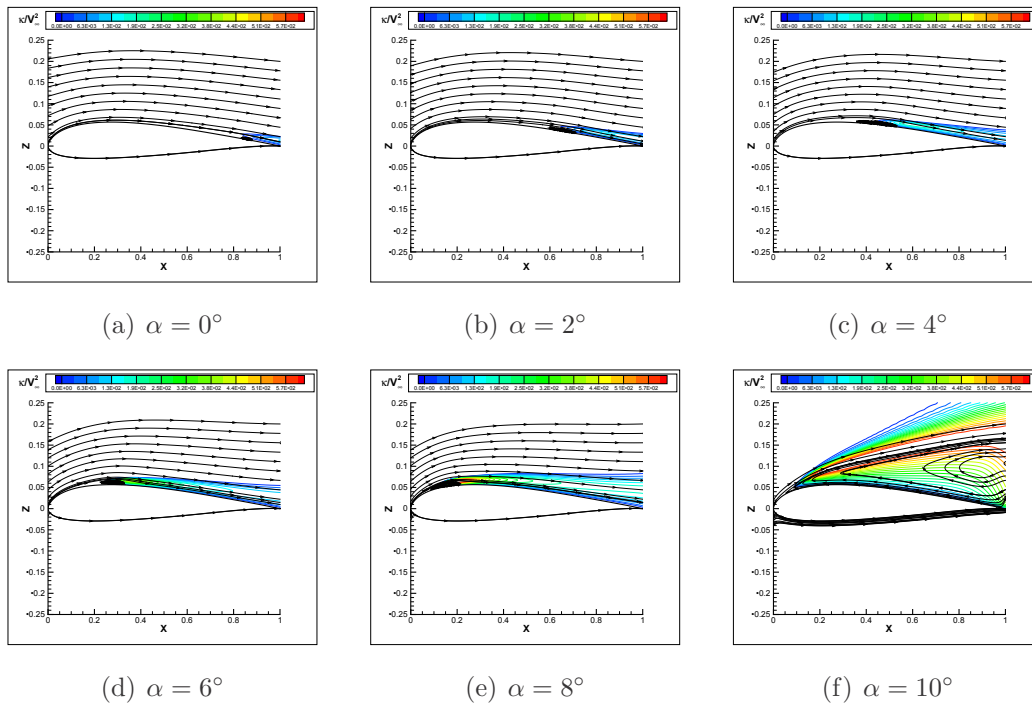


Figure 3.19: SD7003 Airfoil : RANS. Evolution of the bubble with the angle of attack. Contour map of k is shown

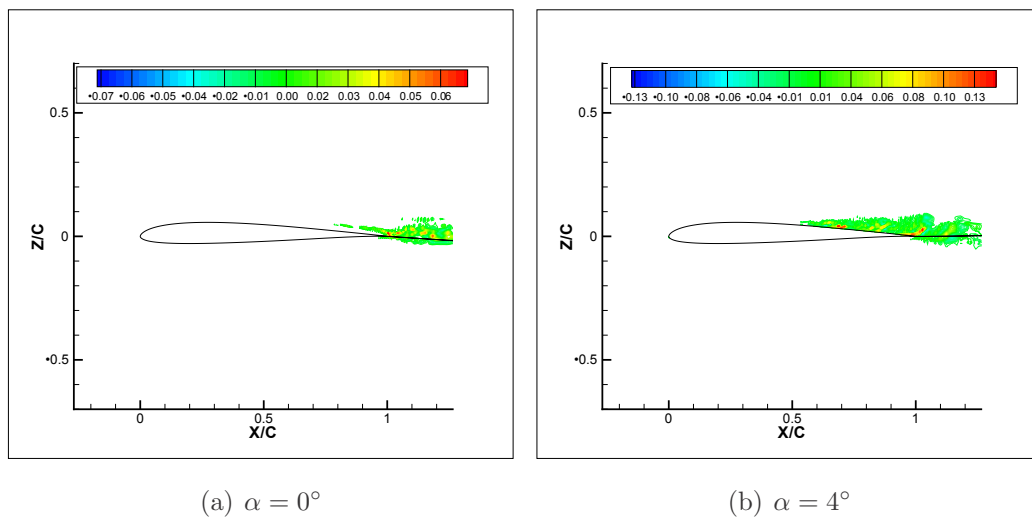


Figure 3.20: SD7003 Airfoil : Large Eddy Simulation. Contour map of the instantaneous spanwise-averaged $\frac{w}{V_\infty}$

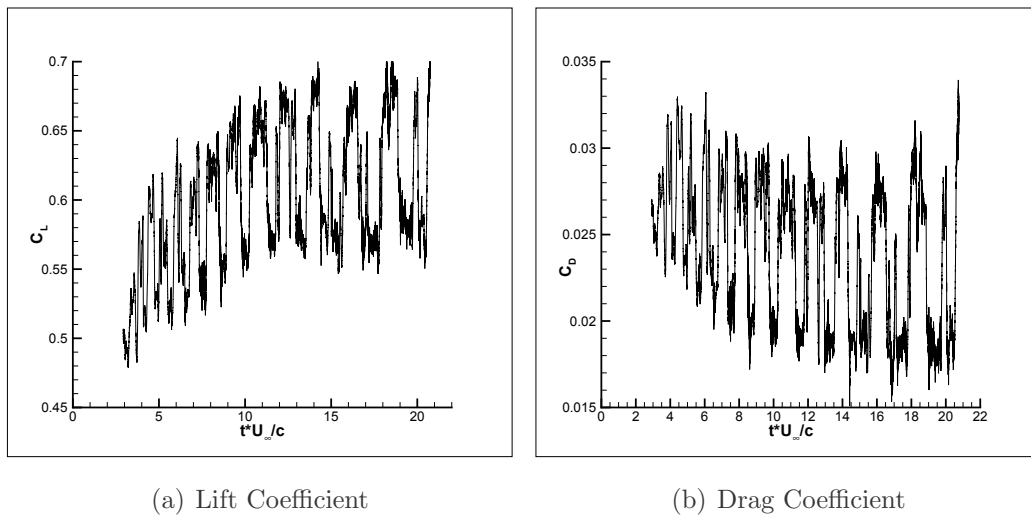


Figure 3.21: SD7003 Airfoil : Large Eddy Simulation at $\alpha = 4^\circ$. Time history of the aerodynamic coefficients.

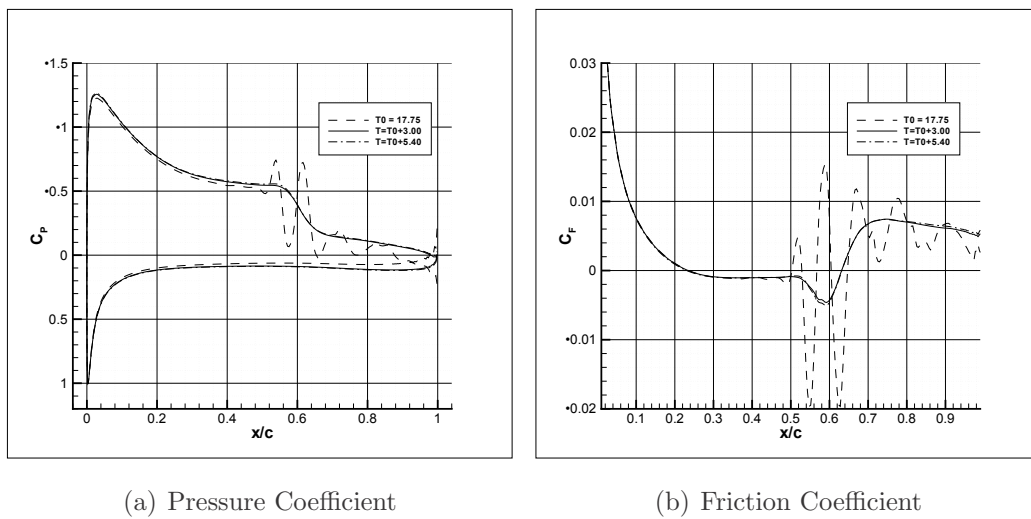
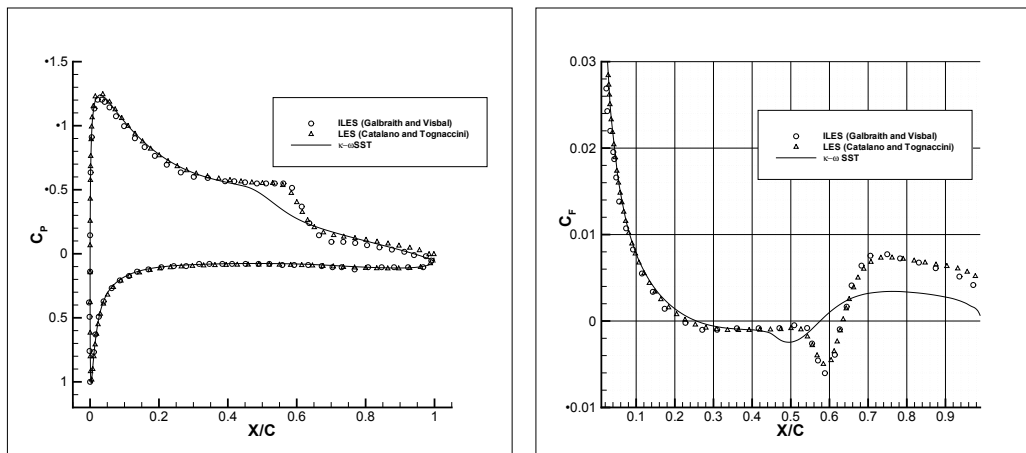


Figure 3.22: SD7003 Airfoil : Large Eddy Simulation at $\alpha = 4^\circ$. Time averaging of pressure and friction coefficient.

time-averaged. Figure 3.22 shows the time-averaging process of the pressure and friction coefficients. The solution achieved at a certain instant shows a well-defined separation point, and a series of separation and re-attachment points downstream the *dear-air* region. The bubble with one separation and one re-attachment point is obtained only when the solution is averaged in



(a) Pressure Coefficient

(b) Friction Coefficient

Figure 3.23: SD7003 Airfoil, $Re = 6.0 \times 10^4$, $\alpha = 4^\circ$. Pressure and friction coefficient; \circ : ILES (Galbraith and Visbal), \triangle : present LES, $—$: RANS $\kappa - \omega$ SST with laminar-turbulent transition not prescribed.

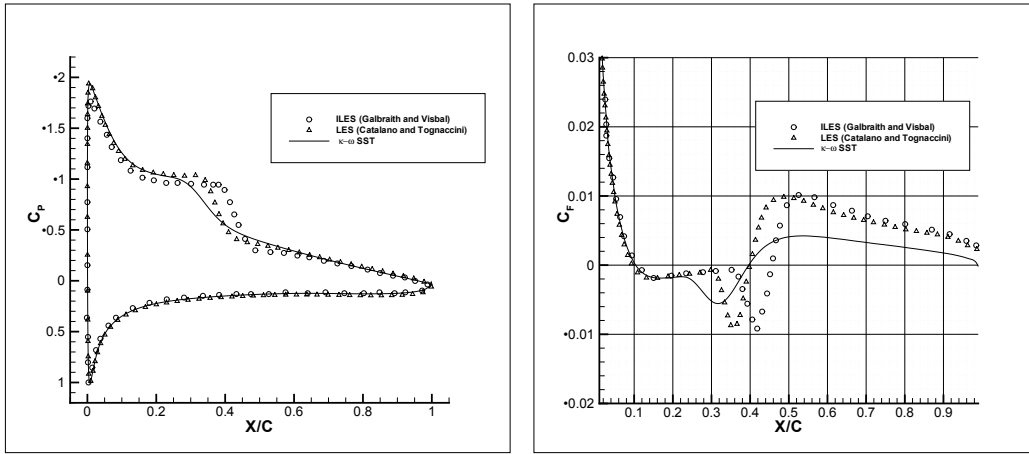
time for a significant period.

3.2.3.3 RANS-LES Comparison

The RANS solutions are compared in terms of pressure and friction coefficients to the large eddy simulations data by the authors and Galbraith and Visbal [18] in the figures 3.23, 3.24, and 3.25 at $\alpha = 4^\circ$, 6° , and 8° respectively. The pressure recovery in the zone of the bubble is much stronger in LES than in RANS data, as can be seen in all the C_p and C_f plots. The separation point is well predicted in the RANS simulations, but the RANS provide a re-attachment anticipated with respect to LES results. Downstream the flow re-attachment, the RANS recover to a level of pressure lower than LES.

The present large eddy simulations are in excellent agreement with the ILES by Galbraith and Visbal [18] at $\alpha = 4^\circ$ and 8° . Some discrepancies can be noted for the flow at $\alpha = 6^\circ$.

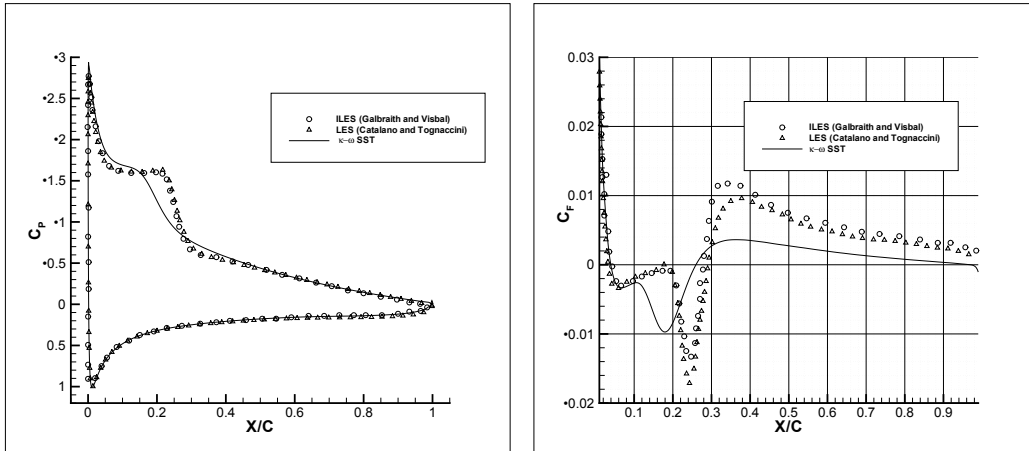
The RANS simulations have been performed without an *a priori* knowledge of the laminar-turbulent transition. It has been shown that a laminar



(a) Pressure Coefficient

(b) Friction Coefficient

Figure 3.24: SD7003 Airfoil, $Re = 6.0 \times 10^4$, $\alpha = 6^\circ$. Pressure and friction coefficient; \circ : ILES (Galbraith and Visbal), \triangle : present LES, —: RANS $\kappa - \omega$ SST with laminar-turbulent transition not prescribed.



(a) Pressure Coefficient

(b) Friction Coefficient

Figure 3.25: SD7003 Airfoil, $Re = 6.0 \times 10^4$, $\alpha = 8^\circ$. Pressure and friction coefficient; \circ : ILES (Galbraith and Visbal), \triangle : present LES, —: RANS $\kappa - \omega$ SST with laminar-turbulent transition not prescribed.

bubble is returned by the RANS methods with the $\kappa-\omega$ SST and the Spalart-Allmaras turbulence models used with low values of free-stream turbulence. The RANS satisfactorily predict the separation point and the flow in the

dead air region. A shorter bubble length and a weaker pressure recovery is provided by RANS with respect to LES.

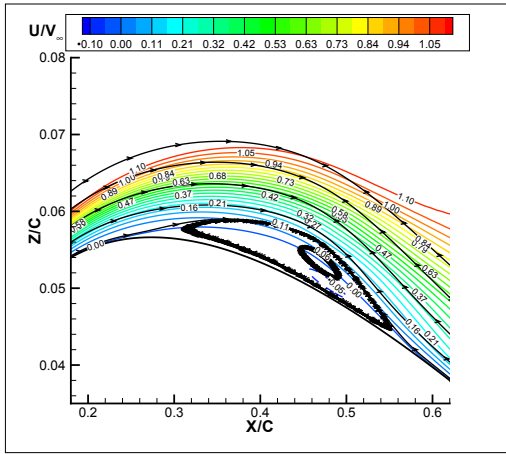
3.2.3.4 Flow at $\alpha = 4^\circ$

A comparison between the bubble returned by the RANS and LES methods at $\alpha = 4^\circ$ is presented in Fig. 3.26. The stream-lines with the contour map of the axial velocity and the pressure coefficient in the zone of the bubble are presented. The LES results are averaged along the span direction and in time for about 8 characteristic times. The structure of a laminar separation bubble [45] (Fig. 3.1) can be recognized. A *dead-air* region is returned by both RANS and LES. The zone of reverse flow lying below the dividing stream-line is characterized by very low value of the U/U_∞ for a large extent of the bubble. The pressure recovery occurs in the zone where stronger negative velocities are attained by the flow. A reverse flow vortex is seen in the LES results while a more spread region of pressure recovery is returned by the RANS method.

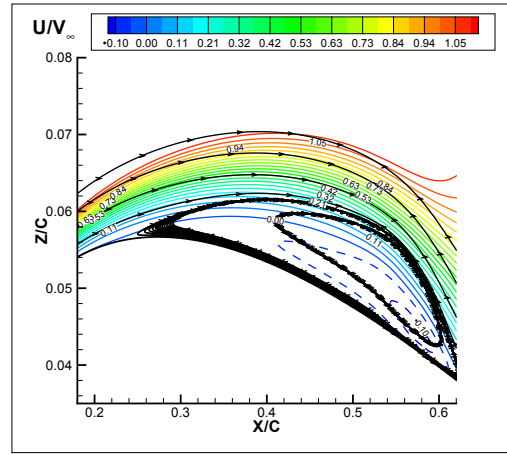
The flow has also been computed by imposing the transition location at $x_{tr}/c = 0.53$, a value retrieved by LES data. The results are expected to improve when the turbulence models are run with the transition point fixed at a reasonable location. This is shown in literature and has been verified by the author [46] for the flow over a flat plate with an imposed pressure gradient [48, 47].

The κ - ω BSL turbulence model [6] is also applied. The comparison between the friction and pressure coefficient achieved by applying the two models without and with the transition location fixed *a priori* is shown in Fig. 3.27. The two κ - ω models provide a similar result when used without fixing the transition location. On the contrary, a large difference occurs when the simulations are performed with the transition point fixed *a priori*. The κ - ω BSL provides a pressure recovery closer to the LES data. On the contrary, the κ - ω SST produces a too low turbulence and the flow does not reattach.

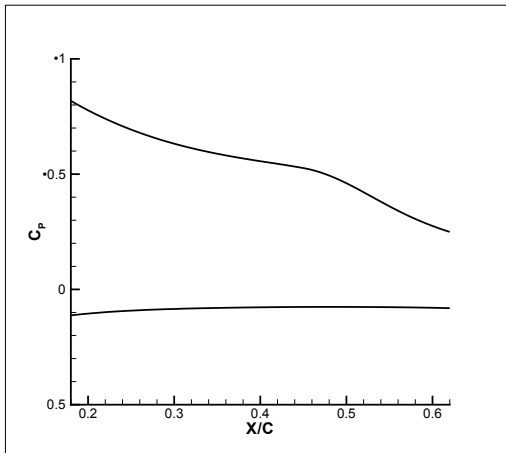
The Shear Stress Transport formulation should allow for a better charac-



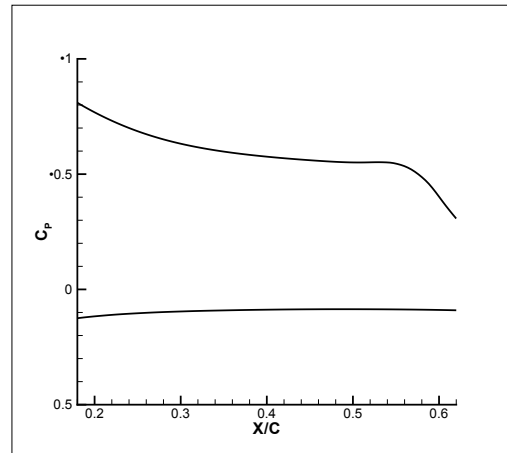
(a) RANS, $\kappa - \omega$ SST with laminar-turbulent transition not prescribed: Streamlines and contour map of the axial velocity



(b) LES : Stream-lines and contour map of the axial velocity



(c) RANS, $\kappa - \omega$ SST with laminar-turbulent transition not prescribed: Pressure Coefficient

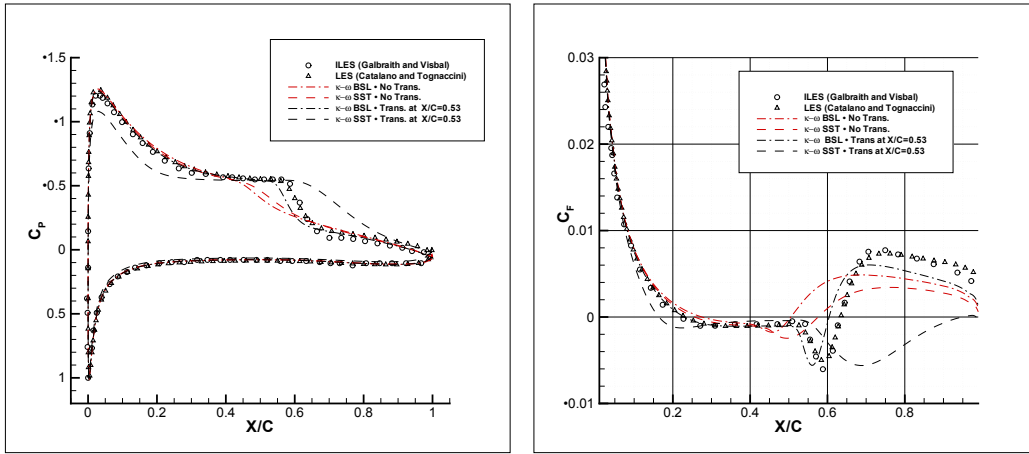


(d) LES : Pressure Coefficient

Figure 3.26: SD7003 Airfoil, $Re = 6.0 \times 10^4$, $\alpha = 4^\circ$. Structure of the Laminar bubble.

terization of flow separations and re-attachments. This has been verified for typical transonic benchmarks, but, as shown by the present results, at low Reynolds number seems to provide results even worse than the baseline BSL model. This confirms the analysis performed by Rumsey and Spalart [19] on

3.2 FLOW AROUND THE SD 7003 AIRFOIL



(a) Pressure Coefficient

(b) Friction Coefficient

Figure 3.27: SD7003 Airfoil, $Re = 6.0 \times 10^4$, $\alpha = 4^\circ$, Pressure and friction coefficient; \circ : ILES (Galbraith and Visbal), \triangle : present LES, $- \cdot -$: RANS $\kappa - \omega$ BSL, $- - -$: RANS $\kappa - \omega$ SST; red lines: transition not specified; black lines: transition fixed ($x_{tr}/c = 0.53$).

the poor accuracy of the $\kappa-\omega$ SST for low-Reynolds number flows.

Turbulence Modelling

This chapter is devoted to the derivation and description of the κ - ω SST-LR turbulence model. This consists in some modifications apported to the κ - ω SST model.

First the equations of the κ - ω SST are re-called, and some results achieved by the model are critically revised. Some features of the model are analyzed at decreasing Reynolds numbers. The implementation of the model will be shown to become critical as the Reynolds number decreases [52].

Modifications of the κ - ω SST model are proposed and applied to flows at low as well as high Reynolds number. The results obtained at low Reynolds number are noticeably improved by this modified model, and the characteristics at high Reynolds number are preserved [53].

4.1 Analysis of the the κ - ω SST model

The SST formulation accounts for computing the shear stress as

$$\tau = a_1 \kappa \quad (4.1)$$

in a suitable part of the boundary layer. This is obtained by considering that for boundary layer flows

$$\tau \approx \mu_t \Omega \quad (4.2)$$

where Ω is the vorticity. The eddy viscosity is computed by making use of a switching between the specific turbulent dissipation ω and Ω

$$\mu_t = \frac{\rho a_1 \kappa}{MAX(a_1 \omega, F_2 \Omega)} \quad (4.3)$$

where $a_1 = 0.3$ and F_2 is a blending function computed as

$$F_2 = \tanh(Arg2^2) \quad (4.4)$$

where

$$Arg2 = \max(Arg21, Arg22) \quad (4.5)$$

with

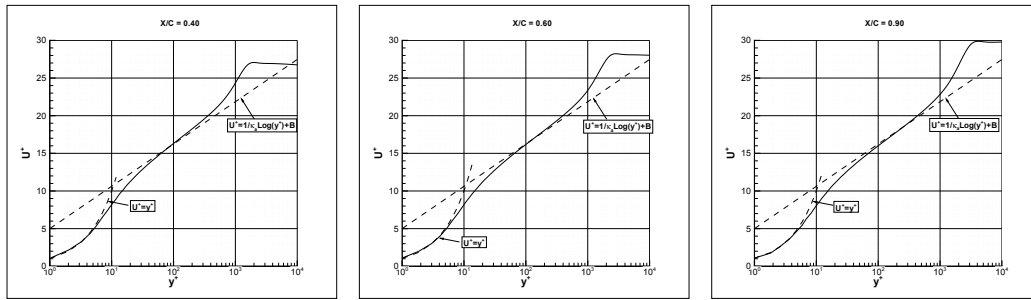
$$Arg21 = \frac{2\sqrt{\kappa}}{\beta^*\omega y}, \quad Arg22 = \frac{500\mu}{\omega y^2} \quad (4.6)$$

The function F_2 has been designed to be 1 close to solid boundaries and zero in the upper part of the logarithmic region of a turbulent boundary layer where Eq. (4.1) should be recovered. The presence and extension of the logarithmic region depends on the Reynolds number. In particular, its extension increases as the Reynolds number increases.

The flow around the SD 7003 airfoil has been analyzed at $\alpha = 0^\circ$ and Reynolds numbers 6.0×10^6 , 6.0×10^5 , and 6.0×10^4 . The turbulent intensity has been set to 0.1% and the ratio between the free-stream turbulent and molecular viscosity to 0.1. This numerical setting allows to concentrate on the effect of the Reynolds number on the boundary layer because laminar separation bubbles are not returned by any of the simulations. The spacing of the first layers of cells has been adapted to the Reynolds number in such a way to obtain a y^+ of order of magnitude one for all the simulations.

The stream-wise velocity profiles at three stations along the upper surface of the SD 7003 airfoil are shown in the Fig. 4.1. The curves $u^+ = y^+$ corresponding to the viscous sub-layer, and $u^+ = \frac{u}{u_\tau} = \frac{1}{\kappa_a} \log y^+ + B$ (with $\kappa_a = 0.41$, and $B = 5.0$) corresponding to the log-layer are also shown. The flow at the highest Reynolds number (Fig. 4.1a, Fig. 4.1b, and Fig. 4.1c) presents a well-defined logarithmic region in a large extent of the boundary layer. At Reynolds number 6.0×10^5 (Fig. 4.1d, Fig. 4.1e, and Fig. 4.1f), the log-layer still exists, but both the thickness of the boundary layer and the extension of the logarithmic region are reduced of an order of magnitude. The numerical results follow fairly well either the linear and the log law of the velocity at both the Reynolds numbers. On the contrary, at $Re = 6.0 \times 10^4$

4.1 ANALYSIS OF THE THE κ - ω SST MODEL

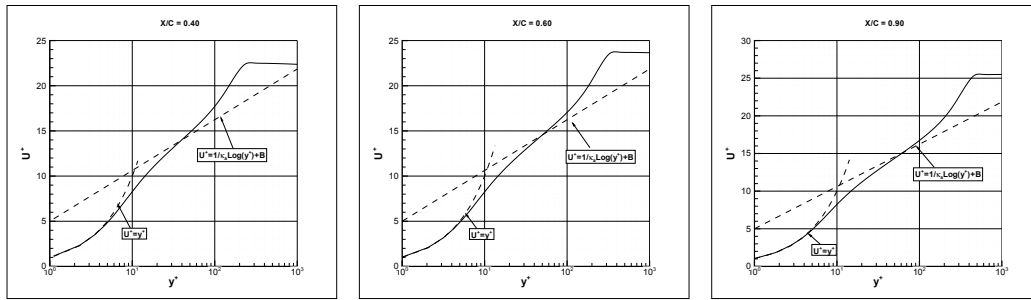


(a) $x/c = 0.40$

(b) $x/c = 0.60$

(c) $x/c = 0.90$

Reynolds number = 6.0×10^6

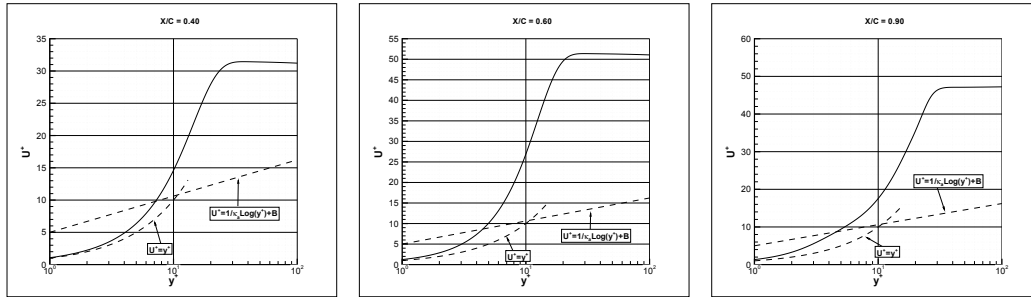


(d) $x/c = 0.40$

(e) $x/c = 0.60$

(f) $x/c = 0.90$

Reynolds number = 6.0×10^5



(g) $x/c = 0.40$

(h) $x/c = 0.60$

(i) $x/c = 0.90$

Reynolds number = 6.0×10^4

Figure 4.1: $\kappa - \omega$ SST. Velocity profiles on the SD 7003 Airfoil at three Reynolds numbers, $\alpha = 0^\circ$

(Fig. 4.1g, Fig. 4.1h, and Fig. 4.1i), the logarithmic region is totally absent in the calculations. The stream-wise velocity has a linear behaviour with y^+ for most of the boundary layer but does not follow the viscous law $u^+ = y^+$. The velocity reaches higher values with respect to the other two lower

Reynolds numbers.

The eddy viscosity is shown in Fig. 4.2. The two quantities $a_1\omega$ and $F_2\Omega$ at denominator of Eq. (4.3) are also reported as symbols, and their maximum as a solid line. Similar results are obtained at Reynolds numbers 6.0×10^6 (Fig. 4.2a, Fig. 4.2b, and Fig. 4.2c) and 6.0×10^5 (Fig. 4.2d, Fig. 4.2e, and Fig. 4.2f). The eddy viscosity is computed as $\mu_t = \rho\kappa/\omega$ in most of the boundary layer. $F_2\Omega$ is greater than $a_1\omega$ in a narrow region close to the zone where μ_t/μ has reached its maximum and starts to decrease. In this region, the eddy viscosity is computed as $\mu_t = a_1\kappa/F_2\Omega$.

At Reynolds number 6.0×10^4 (Fig. 4.2g, Fig. 4.2h, and Fig. 4.2i), the eddy viscosity μ_t/μ is lower than 0.01 at $x/c = 0.40$ and 0.1 at $x/c = 0.60$, and greater than one only at the station $x/c = 0.90$. At this location, $F_2\Omega > a_1\omega$ in the region where μ_t/μ is maximum. The flow can be considered turbulent only at $x/c = 0.90$.

The behaviour of the blending function F_2 (Eq. 4.4) and its arguments (Eq. 4.5 and Eq. 4.6) is presented in the Fig. 4.3. At Reynolds number 6.0×10^6 (Fig. 4.3a, Fig. 4.3b, and Fig. 4.3c), the F_2 , as expected, is computed as a function of the viscous quantity $Arg22$ in the sub-layer and then as a function of the turbulent length scale $Arg21$ in the remaining part of the boundary layer. It is worth noting that at the station $x/c = 0.40$, the F_2 presents a little jump. This can be seen also at Reynolds number 6.0×10^5 (Fig. 4.3d, Fig. 4.3e, and Fig. 4.3f) at $x/c = 0.40$ and in a less pronounced way at $x/c = 0.60$. This occurs in the upper part of the boundary layer when the viscous argument $Arg22$ becomes greater than the turbulent argument $Arg21$. At Reynolds number 6.0×10^4 (Fig. 4.3g, Fig. 4.3h, and Fig. 4.3i), the F_2 shows a large oscillation. Indeed, in the outer part of the boundary layer it again grows while it was expected to vanish in order to correctly perform the switch in the eddy viscosity calculation.

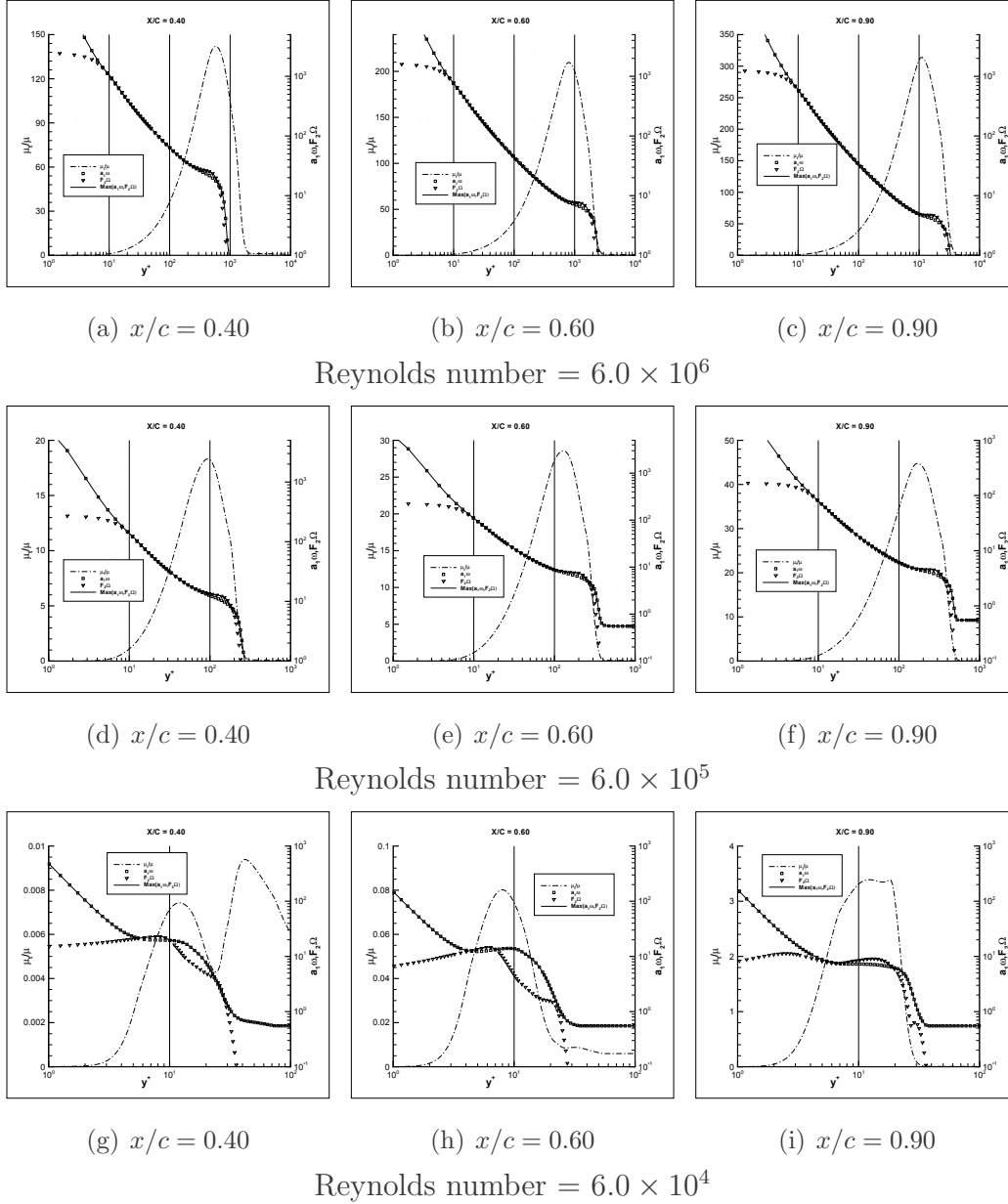


Figure 4.2: κ – ω SST. Eddy viscosity profiles on the SD7003 airfoil at three Reynolds numbers, $\alpha = 0^\circ$; $-\cdot-$: μ_t/μ , \square : $a_1\omega$, ∇ : $F_2\Omega$, $—$: $\max[a_1\omega, F_2\Omega]$

4.2 The κ - ω SST-LR model

The computation of F_2 in the standard SST formulation requires the calculation of the maximum between two arguments (Eq. 4.4). The first one is

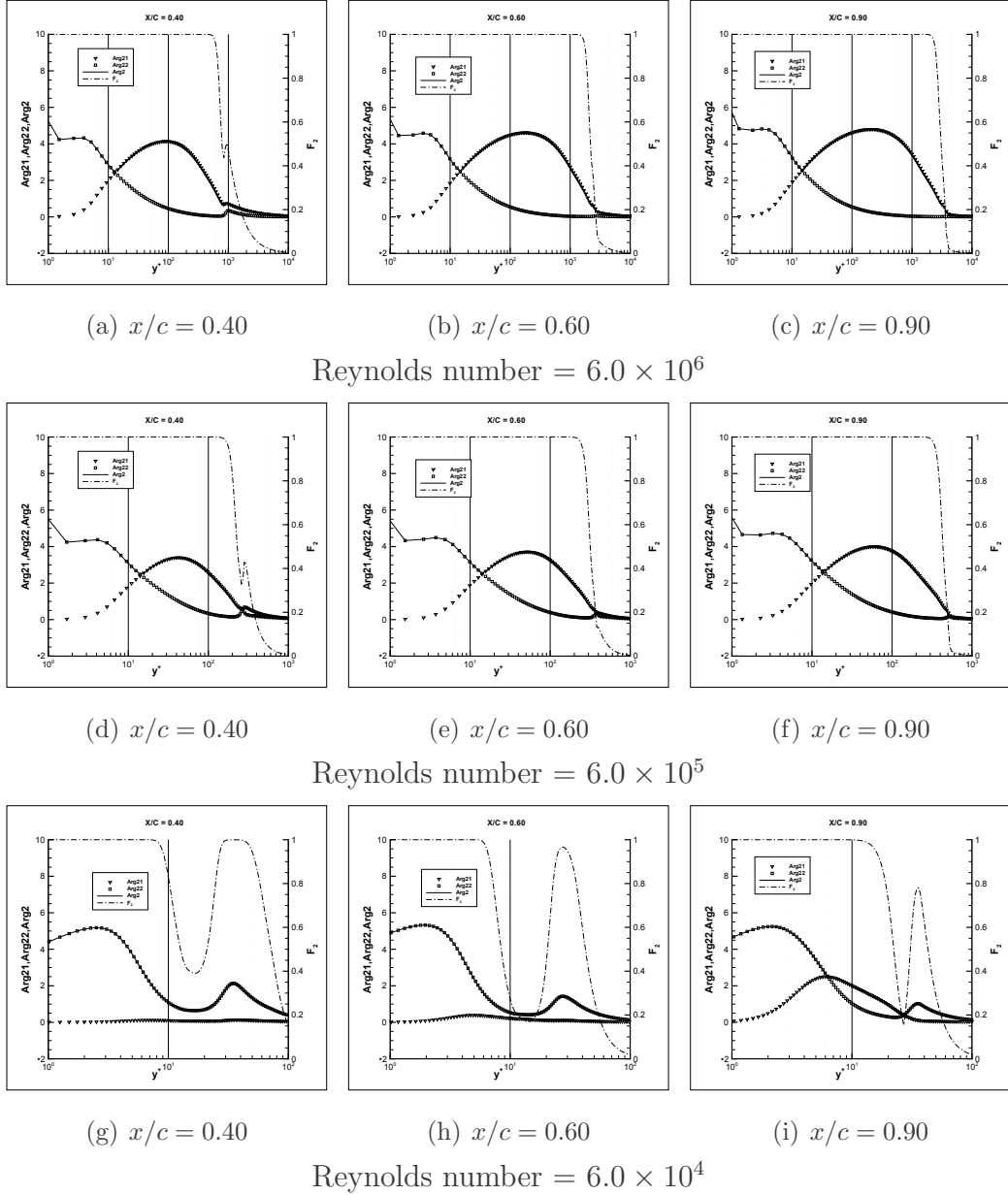


Figure 4.3: κ - ω SST. Function F_2 on the SD7003 airfoil at three Reynolds numbers, $\alpha = 0^\circ$; $-\cdot-$: F_2 , ∇ : $Arg21$, \square : $Arg22$, $—$: $\max[Arg21, Arg22]$

$Arg21$ (Eq. 4.6), the turbulent length scale divided by the distance from the wall. $Arg21$ is zero at the body surface, reaches a maximum in the log-region, and then vanishes in the upper part of the boundary layer. The second argument is $Arg22$ which depends on the molecular viscosity μ , the specific

dissipation rate ω , and the square of the distance from the body surface. The quantity $Arg22$ has a constant value close to a solid boundary since

$$\omega \propto \frac{1}{y^2} \quad as \quad y \longrightarrow 0 \quad (4.7)$$

and behaves as y in the outer part of the boundary layer. $Arg22$ should be important in the viscous sublayer, while $Arg21$ should play a role in the logarithmic part of the boundary layer. This occurs at $Re = 6 \times 10^6$ (Fig. 4.3a, 4.3b, and 4.3c) and $Re = 6 \times 10^5$ (Fig. 4.3d, 4.3e, and 4.3f). In these cases a log region can be clearly discerned in the boundary layer (Fig. 4.1a, 4.1b, 4.1c, and Fig. 4.1d, Fig. 4.1e, Fig. 4.1f). $Arg21$ should be small as the Reynolds number decreases and the log layer tends to disappear, but this is not true at $Re = 6 \times 10^4$. Indeed, the logarithmic region is absent (Fig. 4.1g, Fig. 4.1h, Fig. 4.1i), but $Arg21 > Arg22$ and $F_2 = \tanh(Arg21^2)$ in a significant part of the boundary layer at $x/c = 0.90$ (Fig. 4.3i).

A modification is here proposed in order to correctly apply the SST formulation to low Reynolds number flows. F_2 is again computed following Eq. 4.4, but Eq. 4.5 is modified as :

$$Arg2 = \max(1/k_f * Arg21, Arg22) \quad (4.8)$$

with

$$k_f = \left| \ln \left(k_r / Re \right) \right| \quad k_r = e^{\frac{B}{2\kappa^2 a}} \quad (4.9)$$

The coefficient k_f is of order of magnitude one if $Re \approx 10^6$, and greater than one at lower Reynolds numbers. In this way $Arg21$ decreases in case of low Reynolds numbers flows, but the original formulation is recovered for high Reynolds number flows.

The analysis in the previous section has also highlighted some oscillations of F_2 , more clear as the Reynolds number decreases. As recommended by Menter [6], a limiter for the turbulent specific dissipation in the form

$$\omega \geq \omega_{lim} = k_\omega \frac{U_\infty}{L_{ref}}, \quad k_\omega = 10 \quad (4.10)$$

has been used in the numerical simulations. This limiter does not properly work as the Reynolds number decreases. It has been here updated as follows:

$$\omega \geq \omega_{lim} = k_{\omega} \frac{U_{\infty}}{L_{ref}} * k_f \quad (4.11)$$

The modified model (equations 4.8, 4.9, and 4.11) is referenced as $\kappa - \omega$ SST-LR in the following sections.

4.2.1 Analysis for Low Reynolds Number Flows

The simulations of the flow around the SD 7003 airfoil at $\alpha = 0^\circ$ and Reynolds numbers 6×10^6 , 6×10^5 , and 6×10^4 have been repeated by using the $\kappa - \omega$ SST-LR model.

The velocity profiles are presented in the Fig. 4.4. There are negligible differences with the velocities provided by the $\kappa - \omega$ SST at Reynolds numbers 6×10^6 , and 6×10^5 . Large differences are instead seen at Reynolds number 6×10^4 . Indeed a viscous region is now clearly identified in the boundary layer. The velocity profiles follow the linear law $u^+ = y^+$ very well. The levels of u^+ remain of the same order of magnitude as at the higher Reynolds numbers. It is interesting to compare in Fig. 4.1 and 4.4, the solutions obtained at $x/c = 0.90$. The $\kappa - \omega$ SST-LR, with difference to the *standard* SST, provides a boundary layer profile with a small visible log region, which implies a significant turbulence.

The eddy viscosity is shown in Fig. 4.5. The results obtained by the $\kappa - \omega$ SST-LR model at Reynolds number 6×10^6 present the same behaviour as the μ_t/μ provided by the $\kappa - \omega$ SST (Fig. 4.5) in terms of either maximum value and zone where this maximum is attained. At Reynolds number 6×10^5 , the $\kappa - \omega$ SST-LR returns a slightly more turbulent flow than *standard* SST. The eddy viscosity behaviour after the maximum is slightly more irregular than *standard* SST. At Reynolds number 6×10^4 , the $\kappa - \omega$ SST-LR provides a turbulent flow ($\mu_t/\mu \geq 1$) also at $x/c = 0.60$. With difference to the SST model (Fig. 4.2g, 4.2h, 4.2i), the eddy viscosity is computed as $\mu_t = \rho\kappa/\omega$ in the entire boundary layer at both $x/c = 0.60$, and $x/c = 0.90$. The new

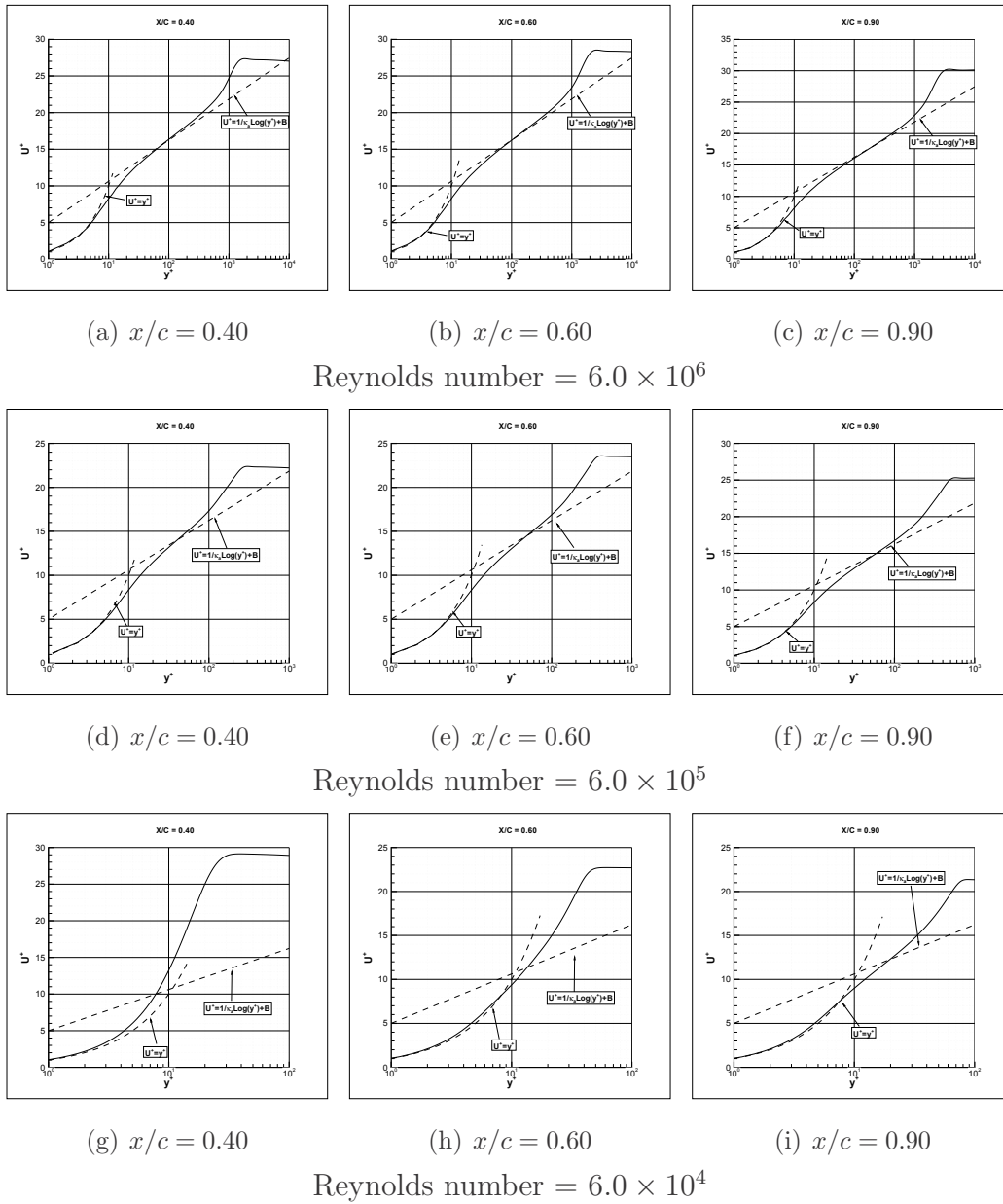


Figure 4.4: $\kappa - \omega$ SST-LR. Velocity Profiles on the SD7003 airfoil at three Reynolds numbers, $\alpha = 0^\circ$

limiter Eq. 4.11 increases significantly the value of $a_1\omega$ at the edge of the boundary layer.

The Fig. 4.6 shows the function F_2 computed by equations 4.4, 4.8, and 4.9. There are not significant differences between the results obtained by the

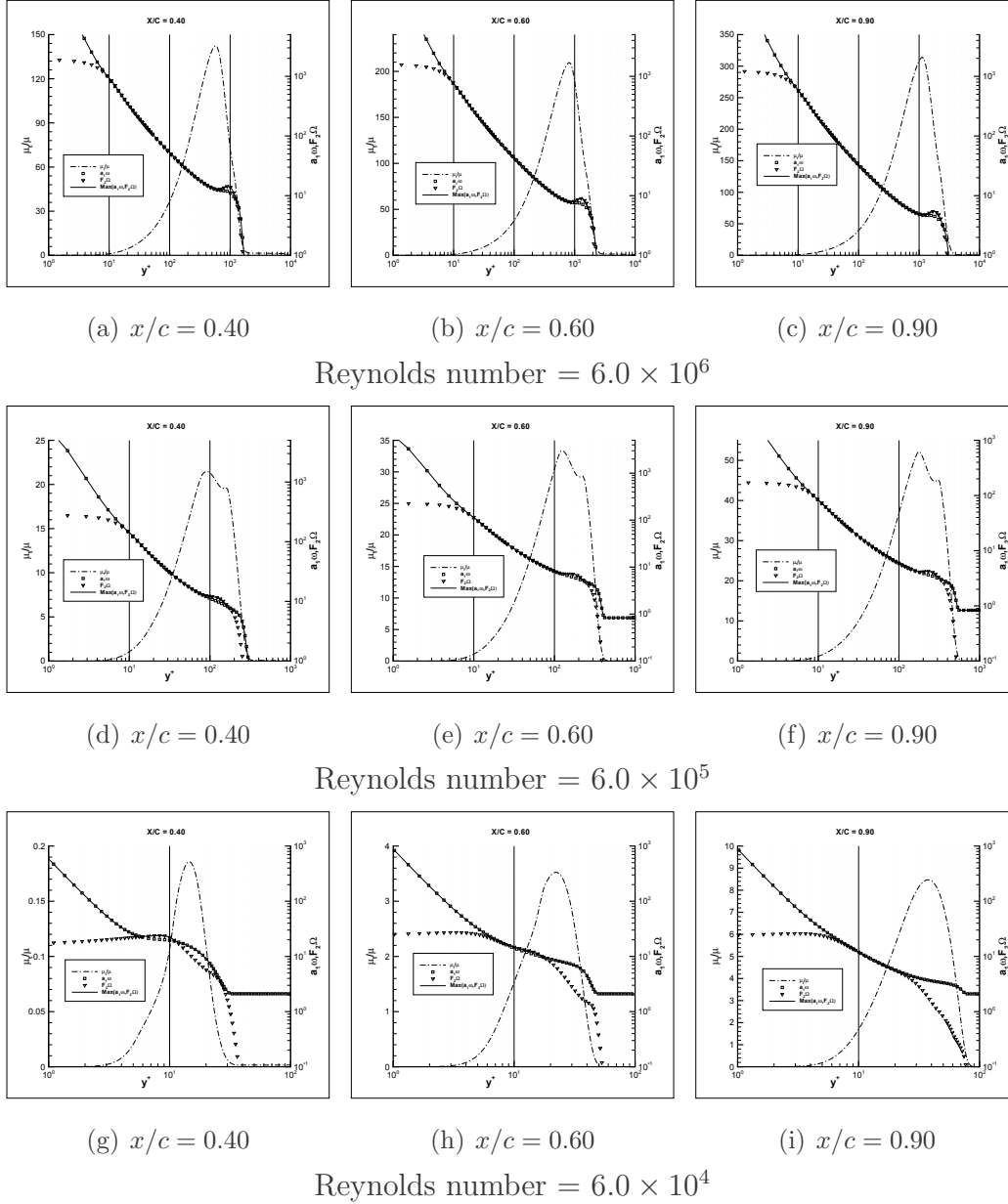


Figure 4.5: $\kappa - \omega$ SST-LR. Eddy viscosity profiles on the SD7003 airfoil at three Reynolds numbers, $\alpha = 0^\circ$; $-\cdot-$: μ_t/μ , \square : $a_1\omega$, ∇ : $F_2\Omega$, $—$: $\max[a_1\omega, F_2\Omega]$

$\kappa - \omega$ SST-LR and SST at all the three Reynolds numbers. The F_2 obtained by the $\kappa - \omega$ SST-LR has the same behaviour and goes to zero in the same zone of the boundary layer as the results provided by $\kappa - \omega$ SST (Fig. 4.3).

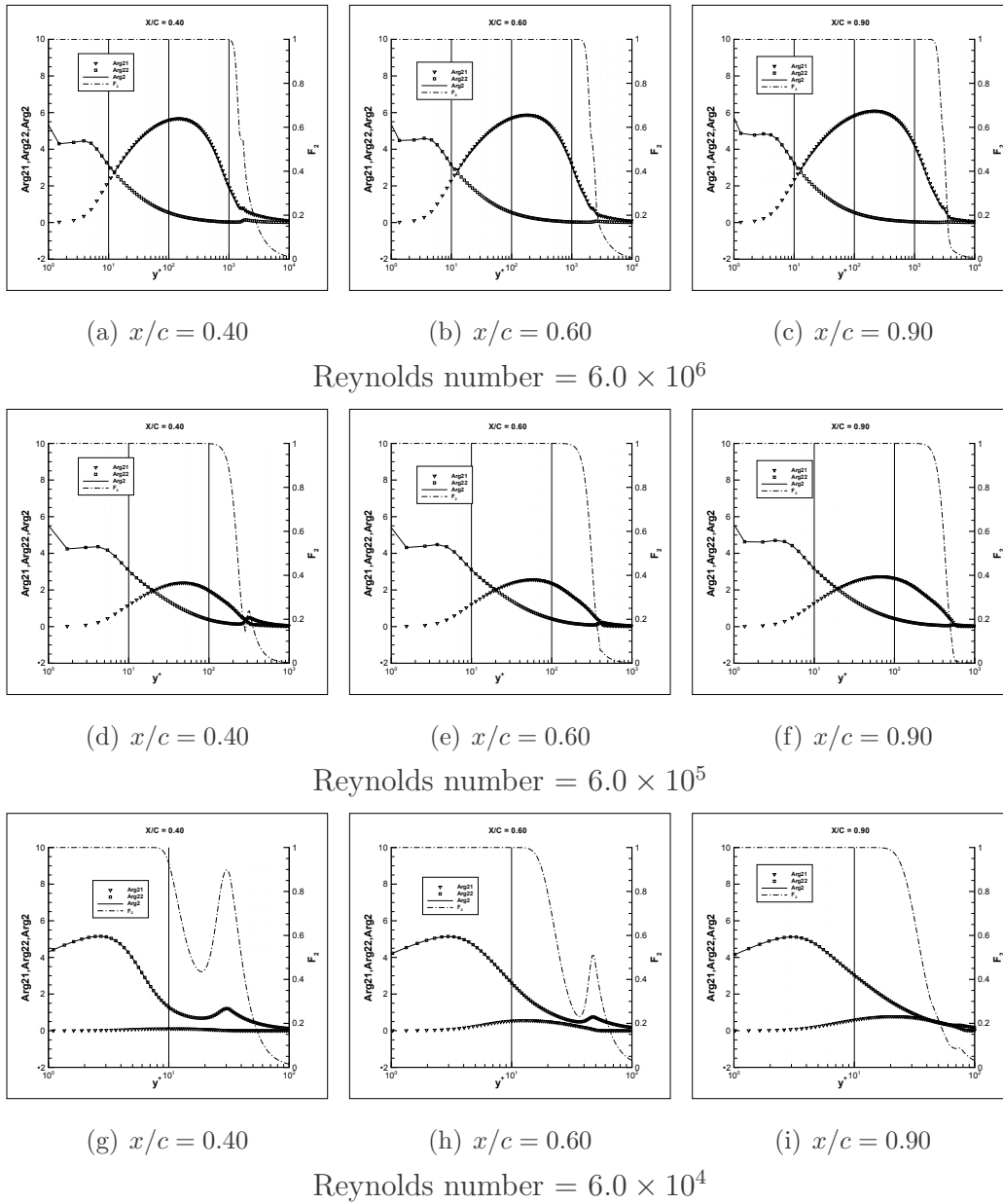


Figure 4.6: $\kappa - \omega$ SST-LR. Function F_2 on the SD7003 airfoil at three Reynolds numbers, $\alpha = 0^\circ$; $-\cdot-$: F_2 , ∇ : $Arg21$, \square : $Arg22$, $—$: $\max[Arg21, Arg22]$

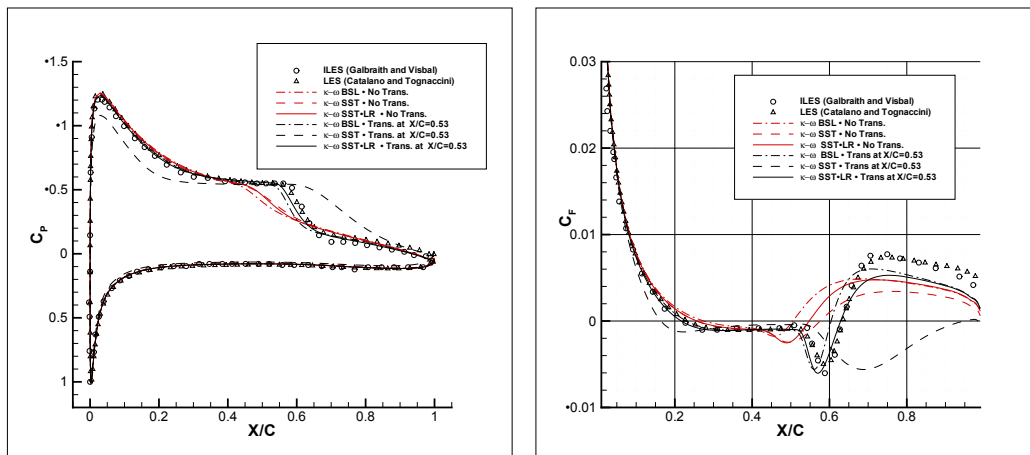
The oscillation in the F_2 is still present but reduced. F_2 depends on $Arg22$ close to the airfoil surface, and is $F_2 = \tanh(Arg21^2)$ in the log-layer zone. At Reynolds number 6×10^4 , $F_2 = \tanh(Arg22^2)$ except in a very narrow

zone at the station $x/c = 0.90$. This is consistent with the fact that the $\kappa - \omega$ SST-LR provides at $Re = 6 \times 10^4$ and $x/c = 0.90$ a turbulent solution with a logarithmic region in the boundary layer. It is worth noting that the discontinuous behaviour of the F_2 at Reynolds number 6×10^4 has no effect on the solution since, as already seen, the eddy viscosity is computed as $\mu_t = \rho\kappa/\omega$ in all the boundary layer.

In conclusions, the $\kappa - \omega$ SST-LR has returned the same results as the $\kappa - \omega$ SST model at high Reynolds number and improved the results at low Reynolds number. In particular at Reynolds number 6×10^4 , the flow presents a well-defined viscous region and a developing turbulent logarithmic zone.

The $\kappa - \omega$ SST-LR model has been applied to compute the flow at $\alpha = 4^\circ$ and Reynolds number 6×10^4 around the SD 7003 airfoil. The free-stream values of the turbulence are lowered $\left(\left(\frac{\mu_t}{\mu}\right)_\infty = 1 \times 10^{-9} \text{ and } \left(\frac{\sqrt{\kappa}}{U}\right)_\infty = 10^{-6}\right)$ in such a way to obtain a laminar separation bubble. The model has been employed with and without the transition imposed (same numerical input as previous tests with the standard formulation). The new and some previous results are presented together in Fig. 4.7. In case of simulation with transition point fixed, the results obtained by the $\kappa - \omega$ SST-LR model are significantly improved with respect to the *standard* SST. The $\kappa - \omega$ SST-LR model has returned a flow more turbulent than the *standard* SST. This has allowed the re-attachment of the flow and a pressure recovery in a far better agreement with LES results. The results are also slightly improved with respect to the $\kappa - \omega$ BSL, with a better agreement of the reattachment point. The stream-lines and the contour map of the axial velocity achieved by the $\kappa - \omega$ SST-LR are shown in Fig. 4.8. The structure of a laminar separation bubble (Fig. 3.1) is well resembled. The height and the length of the bubble are in good agreement with LES results (Fig. 3.26b), and improved with respect to the $\kappa - \omega$ SST model (Fig. 3.26a).

In case of simulation without specification of the transition point, the modifications of the results are not so dramatic, in particular the agreement



(a) Pressure Coefficient

(b) Friction Coefficient

Figure 4.7: SD7003 Airfoil, $Re = 6 \times 10^4$, $\alpha = 4^\circ$. Pressure and friction coefficient; \circ : ILES (Galbraith and Visbal), \triangle : present LES, $- \cdot -$: RANS $\kappa - \omega$ BSL, $- - -$: RANS $\kappa - \omega$ SST, $—$: RANS $\kappa - \omega$ SST-LR; red lines: transition not specified, black lines: transition fixed ($x_{tr}/c = 0.53$).

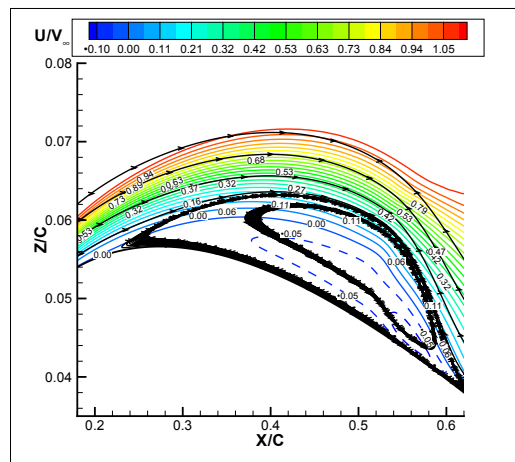
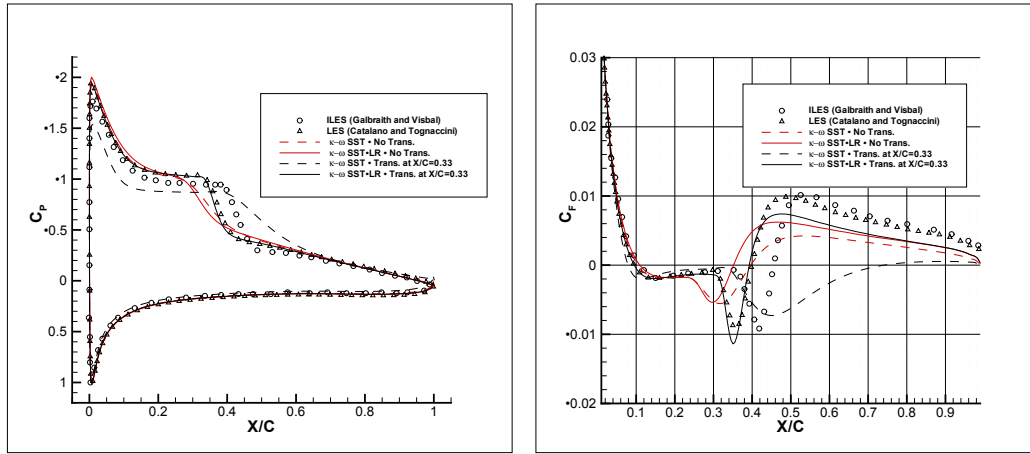


Figure 4.8: SD7003 Airfoil, $Re = 6.0 \times 10^4$, $\alpha = 4^\circ$. RANS $\kappa - \omega$ SST-LR, transition fixed ($x_{tr}/c = 0.53$): Structure of the laminar bubble.

of the reattachment point with LES results remains poor.

A possible strategy to compute the flow at low Reynolds number around an airfoil by the RANS approach can be the following. First, the presence of



(a) Pressure Coefficient

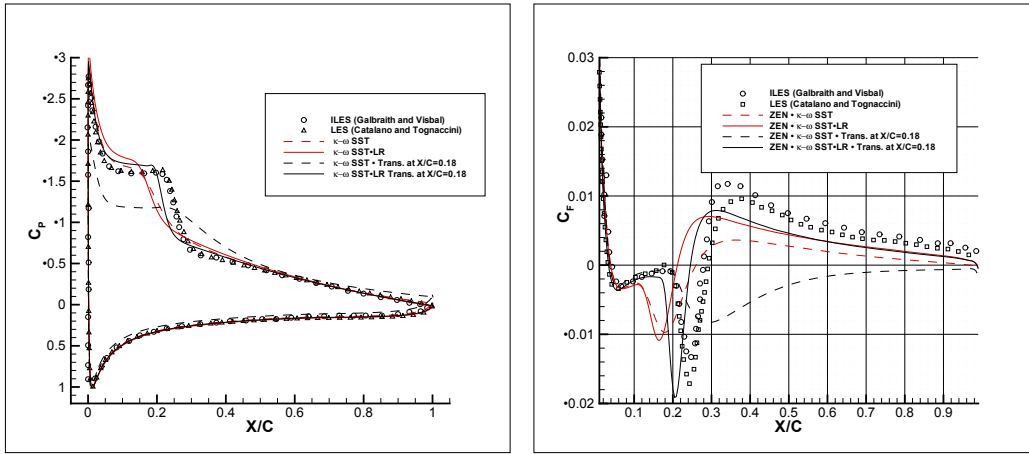
(b) Friction Coefficient

Figure 4.9: SD7003 Airfoil, $Re = 6 \times 10^4$, $\alpha = 6^\circ$. Pressure and friction coefficient; \circ : ILES (Galbraith and Visbal), \triangle : present LES, $---$: RANS $\kappa - \omega$ SST, $---$: RANS $\kappa - \omega$ SST-LR; red lines: transition not specified, black lines: transition fixed ($x_{tr}/c = 0.33$).

laminar separation bubbles can be detected by a simulation with low values of free-stream turbulence. Then, the results can be improved by imposing the transition location. A reasonable point is downstream the X/C where the friction coefficient is minimum. The flow at $\alpha = 6^\circ$ has been computed by this strategy and applying the κ - ω SST and SST-LR turbulence models. The results are shown in figure 4.9. The transition location is fixed 10% downstream the point of minimum C_f . The pressure and friction coefficients achieved by the $\kappa - \omega$ SST-LR in case of prescribed transition are in very good agreement with the LES data. The κ - ω SST model returns a poor result as for the flow at $\alpha = 4^\circ$.

The same strategy has been applied also to the flow at $\alpha = 8$ and 9 . The results are presented in the figures 4.10 and 4.11. The improvement in the pressure and friction coefficients achieved by the $\kappa - \omega$ SST-LR model with the transition point prescribed is evident. The $\kappa - \omega$ SST provides the same kind of results as at the other angles of attack.

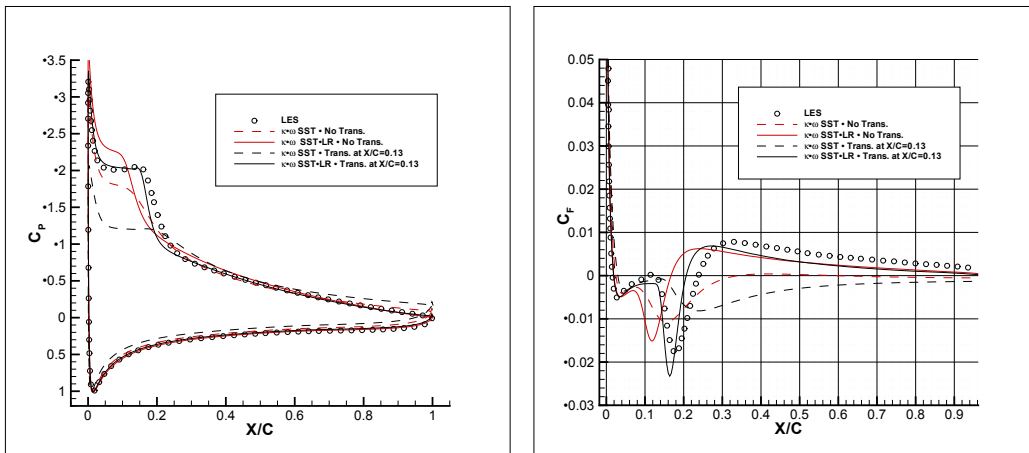
The very rough criterion used for imposing the transition could be im-



(a) Pressure Coefficient

(b) Friction Coefficient

Figure 4.10: SD7003 Airfoil, $Re = 6 \times 10^4$, $\alpha = 8^\circ$. Pressure and friction coefficient; \circ : ILES (Galbraith and Visbal), \triangle : present LES, ---: RANS $\kappa - \omega$ SST, —: RANS $\kappa - \omega$ SST-LR; red lines: transition not specified, black lines: transition fixed ($x_{tr}/c = 0.18$).



(a) Pressure Coefficient

(b) Friction Coefficient

Figure 4.11: SD7003 Airfoil, $Re = 6 \times 10^4$, $\alpha = 9^\circ$. Pressure and friction coefficient; \circ : ILES (Galbraith and Visbal), \triangle : present LES, ---: RANS $\kappa - \omega$ SST, —: RANS $\kappa - \omega$ SST-LR; red lines: transition not specified, black lines: transition fixed ($x_{tr}/c = 0.13$).

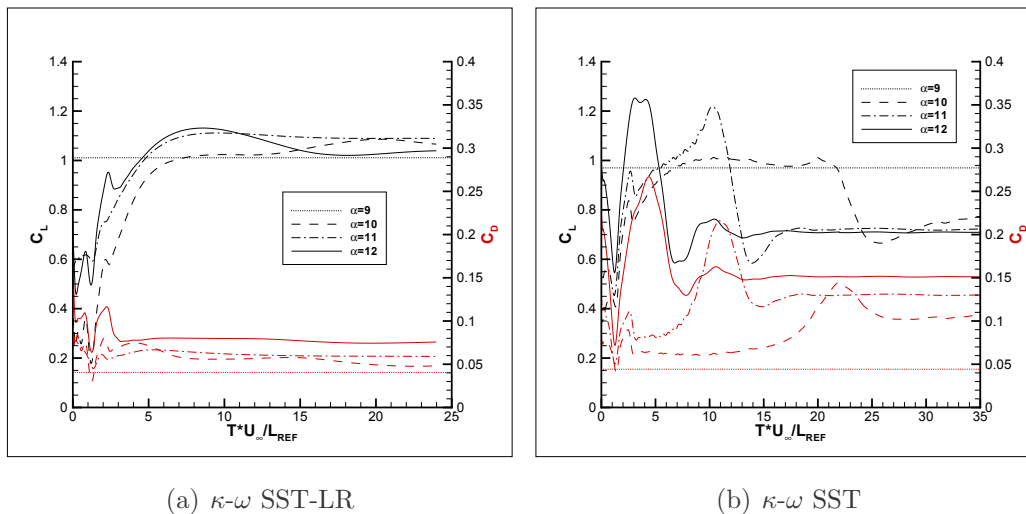


Figure 4.12: URANS of the flow around the SD7003 airfoil: Time evolution of lift and drag coefficients

proved by using methods able to estimate the transition location starting from a pressure distribution [54].

4.3 Drag polar of the SD 7003 airfoil

The drag polar of the SD 7003 airfoil at Reynolds number 6.0×10^4 has been computed by the the κ - ω SST and SST-LR models [55]. RANS simulations up to $\alpha = 9$, and time-accurate URANS simulations from $\alpha = 10$ to 12 have been performed. Three levels of the computational grid are used in the time-accurate computations in order to limit the CPU time.

The evolution in time of the lift and drag coefficients are shown in figure 4.12. Steady state solutions are obtained in all the simulations. The κ - ω SST-LR model (figure 4.12_a) provides solutions with a C_L slightly increasing with the angle of attack up to $\alpha = 11$. A light decrease is seen for $\alpha = 12$. Instead, the κ - ω SST (figure 4.12_b) yields a drop of the lift coefficient when α goes from 9 to 10. The drag coefficient increases with the angle of attack for both the models. A large variation of C_D occurs for the κ - ω SST model between $\alpha = 9$ and 10.

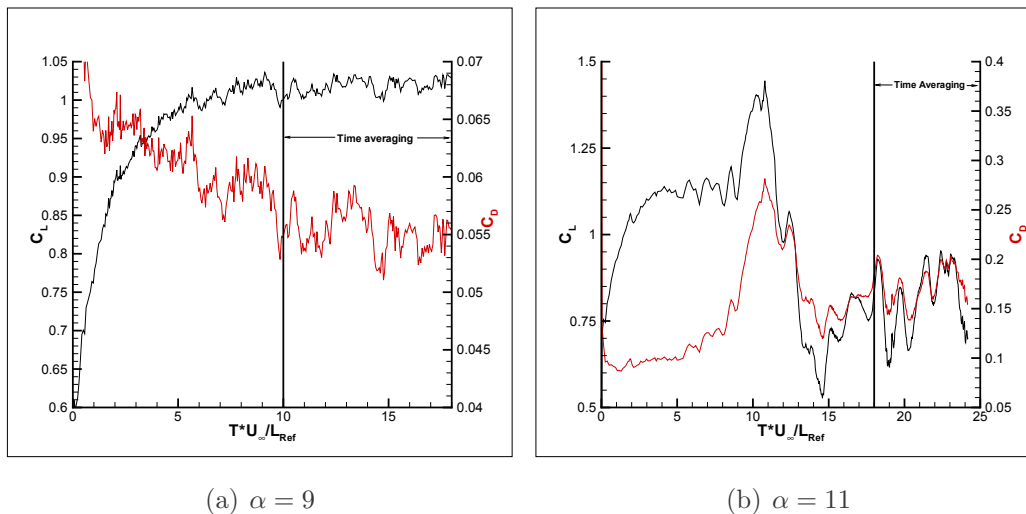
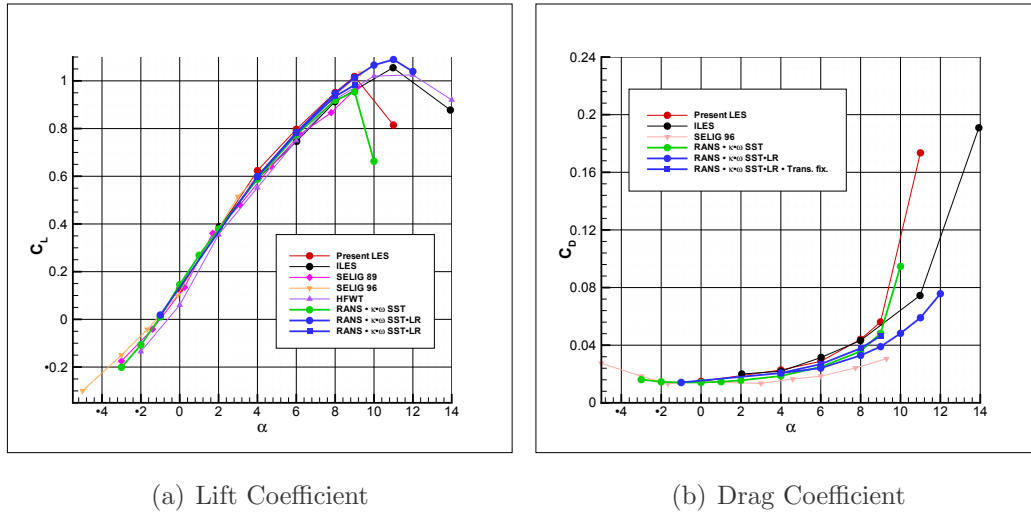


Figure 4.13: Large Eddy simulation of the flow around the SD 7003 airfoil: Time evolution of lift and drag coefficients

Large eddy simulations have also been performed up to $\alpha = 11$. The span-wise extension Δz of the computational domain is $0.1 \times c$ for $\alpha \leq 9$ and $0.2 \times c$ for $\alpha > 9$. The number of cells used in the span-wise direction is 48 for $\Delta z = 0.1$, and 96 for $\Delta z = 0.2$. The simulations are started from a RANS flow field. The solution is first advanced in time with a fixed Courant number and a time step computed on the basis of numerical stability analysis. Then, once the solution has started to develop, a constant time step $\Delta t = 0.5 \times 10^{-4}$ is used. The evolution in time of the aerodynamic coefficients is presented in figure 4.13 for $\alpha = 9$ and 11. The behaviour of the aerodynamic coefficient at $\alpha = 11$ shows a large variation when the flow starts to separate on the central region of the upper surface of the airfoil.

The lift and drag coefficients are compared (figure 4.14) to three sets of experimental data, and to the numerical results obtained by the ILES approach [18]. The measurements taken from Selig *et al.* [56] at University of Princeton in 1989, from Selig *et al.* [57] at University of Illinois in 1996, and from Ol *et al.* [49] at the Horizontal Free-Surface Wind Tunnel (HFWT) of the Air Force Research Laboratory in 2005 are considered.

The differences in the lift coefficient (figure 4.14_a) are mainly seen at the


 Figure 4.14: SD7003 Airfoil : Drag Polar at $Re = 6.0 \times 10^4$

high incidences. The $\kappa-\omega$ SST model provides a stall anticipated with respect to all the other set of data. The $\kappa-\omega$ SST-LR model follows the experimental and ILES data very well. The largest differences are with the HFWT data and are always lower than 5%.

The large eddy simulations data slightly over-predict the ILES (6% at $\alpha = 6$) and experimental data (10% with respect to HFWT, 2% with respect to Selig 96, 3% with respect to Selig 89 at $\alpha = 6$) and yields a stall at $\alpha = 11$, lower than the stall angle provided by the implicit LES and the experiments from Selig.

All the computed drag coefficient over-predict the experimental measurements (figure 4.14.b). The large eddy simulations are in good agreement between them. The largest difference is about 8% at $\alpha = 6$.

The RANS results under-predict the large eddy simulations (both explicit and implicit). The $\kappa-\omega$ SST-LR model provides at $\alpha = 4$ a C_D 5% lower than LES and 9% lower than ILES. The under-prediction with respect to LES data grows to 15% and 20% at $\alpha = 6$ and 8 respectively. The ILES data are under-predicted of 23% at both $\alpha = 4$ and 6.

The $\kappa-\omega$ SST model has an under-prediction with respect to ILES data of 15% at $\alpha = 4$, 20% at $\alpha = 6$, and 17% at $\alpha = 8$. The drag coefficients are

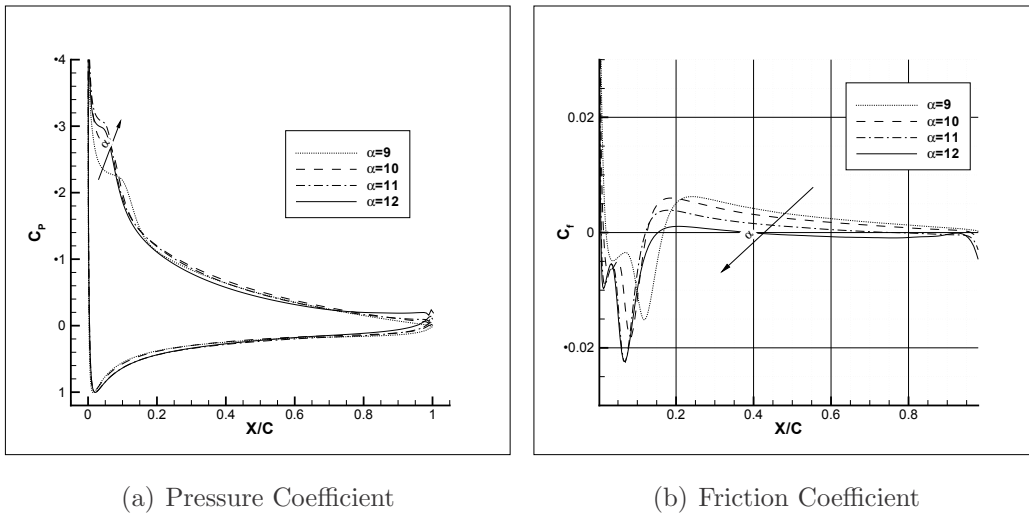


Figure 4.15: SD7003 Airfoil : Evolution with α of the pressure and friction coefficient. κ - ω SST-LR turbulence model - transition not specified.

lower than LES data of 18% at $\alpha = 4$ and 8, 13% at $\alpha = 6$.

The results at higher angles of incidence are close to the drag rise of the stall and have not been analyzed from a quantitative point of view.

The comparison between LES and the RANS data obtained by fully turbulent simulations is acceptable at low angles of attack. The C_D and C_L achieved by the κ - ω SST-LR with an imposed transition point (also if with a very rough criterion) are also shown in figure 4.14. The agreement with the aerodynamic coefficients provided by the large eddy simulations improves. The largest difference presented by the C_D is 14%. This occurs at $\alpha = 6$ for the comparison with the explicit LES, and at $\alpha = 8$ for the explicit LES.

4.3.1 Stall Characteristics

The evolution with the angle of attack of the pressure and friction coefficients achieved by the κ - ω SST-LR turbulence model is presented in figure 4.15. The bubble moves towards the leading edge of the airfoil as α increases from 9 to 10. Both the separation and re-attachment points do not change for $\alpha = 11$ but the recovery of the pressure is decreased. A separation zone starts to develop in the trailing edge zone at $\alpha = 11$. The flow at $\alpha = 12$

4.3 DRAG POLAR OF THE SD 7003 AIRFOIL

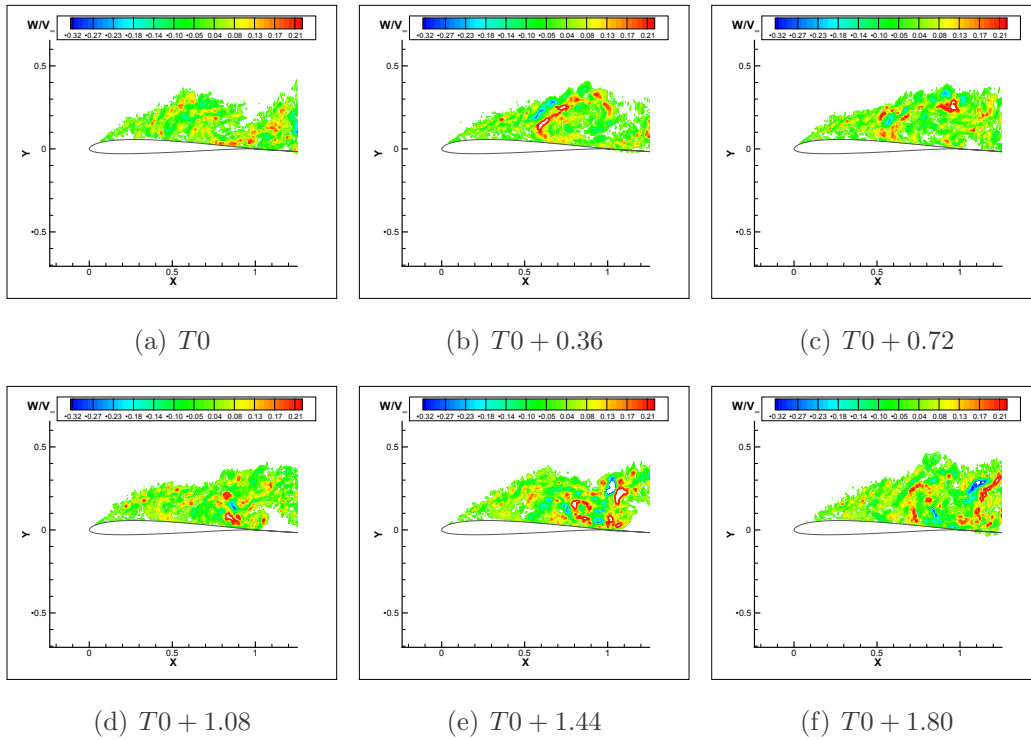


Figure 4.16: SD7003 Airfoil : Large Eddy Simulation at high α . Instantaneous span-wise averaged w/v_∞

re-attaches at a level of pressure significantly lower with respect to $\alpha = 11$. A large separated region is present on the upper surface of the airfoil. As α still increases the flow is not more able to re-attach and the bubble joins with the region of the separated flow forming on the upper surface of the airfoil. Therefore a combined stall occurs.

This analysis is confirmed by LES results. Figure 4.16 shows the span-wise velocity at high angle of attack. The w is averaged in the span direction and is presented at six different instants of time. The bubble in the leading edge zone can be discerned. Turbulent flow structures downstream the bubble are also visible in some plots. A large region of separated flow is present in the upper region of the airfoil.

The fluctuations originating in the zone of the bubble and the large zone of separated flow are also visible in the pressure distribution (figure 4.17). A re-circulating flow at low pressure is present on the upper region of the airfoil.

4.3 DRAG POLAR OF THE SD 7003 AIRFOIL

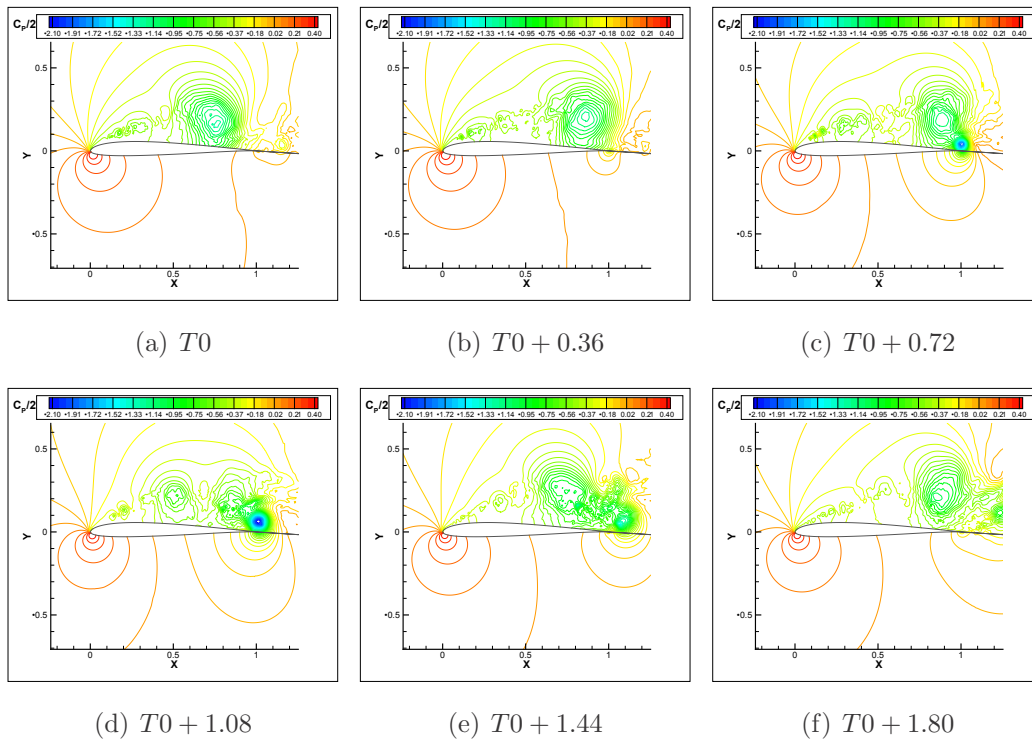


Figure 4.17: SD7003 Airfoil : Large Eddy Simulation at high α . Instantaneous span-wise averaged $(P - P_\infty)/(\rho_\infty v_\infty^2)$

A second low-pressure re-circulating zone appears close to the trailing-edge, is fed by the upstream flow, and then is convected downstream in the wake.

Transonic Flows

The κ - ω SST-LR is applied to typical transonic benchmarks [22] in order to verify that the accuracy and reliability of the *original* SST formulation is recovered for transonic flows at high Reynolds number. The RAE 2822 airfoil and the wing RAE M2155 are considered.

5.1 RAE 2822 Airfoil

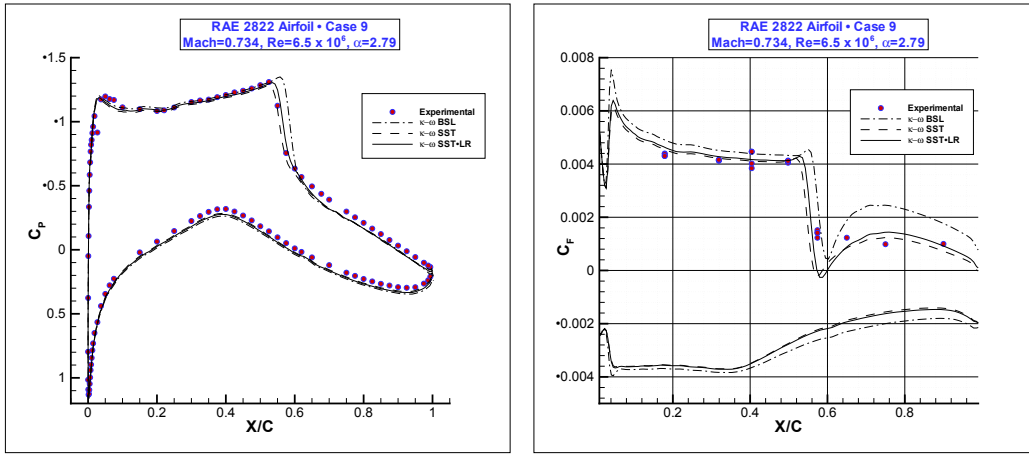
The flow around the RAE 2822 airfoil has been computed at the following specifications named as case 9 and case 10 in literature [58].

	Case 9	Case 10
Mach number =	0.734	0.754
Reynolds number =	6.5×10^6	6.2×10^6
$\alpha =$	2.79	2.54

The transition is fixed at $X/C = 0.3$ as in the experiments. The flow is characterized by a strong shock boundary-layer interaction.

5.1.1 Case 9

The pressure and the friction coefficient achieved by the κ - ω BSL, SST, and SST-LR turbulence models for the case 9 flow condition are compared to the experimental data in figure 5.1. The friction coefficients on the lower surface of the airfoil are reported as negative values. The agreement with



(a) Pressure Coefficient

(b) Friction Coefficient

Figure 5.1: RAE 2822 Airfoil, Case 9 flow condition: Pressure and friction coefficient; symbols: experimental, $-\cdot-$: RANS $\kappa - \omega$ BSL, $- - -$: RANS $\kappa - \omega$ SST, $—$: RANS $\kappa - \omega$ SST-LR;

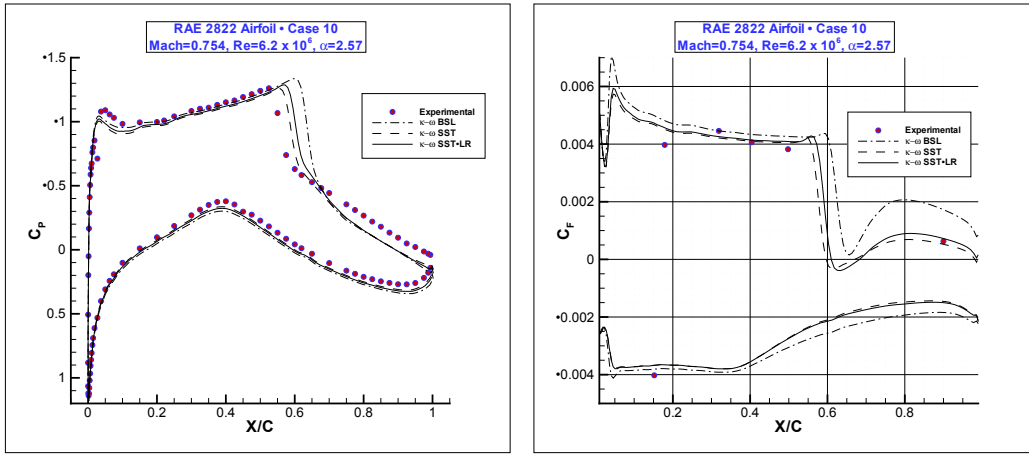
the experimental data is good for all the three turbulence models. The SST and SST-LR provide a very similar pressure and friction coefficients and a weak shock-induced separation. The BSL model shows a shock located more downstream with respect to the other results.

5.1.2 Case 10

At the condition named as case 10, the flow is characterized by a shock-induced separation followed by a pressure recovery and a re-attachment.

The pressure and the friction coefficients are shown in figure 5.2. Differences between the turbulence models are more evident with respect to the case 9 flow condition. The $\kappa - \omega$ SST and SST-LR return a shock-induced separation. The SST predicts the location of the shock better than the SST-LR, and the SST-LR shows a pressure recovery in the region where the flow re-attaches stronger than the SST. The $\kappa - \omega$ BSL provides a shock located too downstream and does not present a separation.

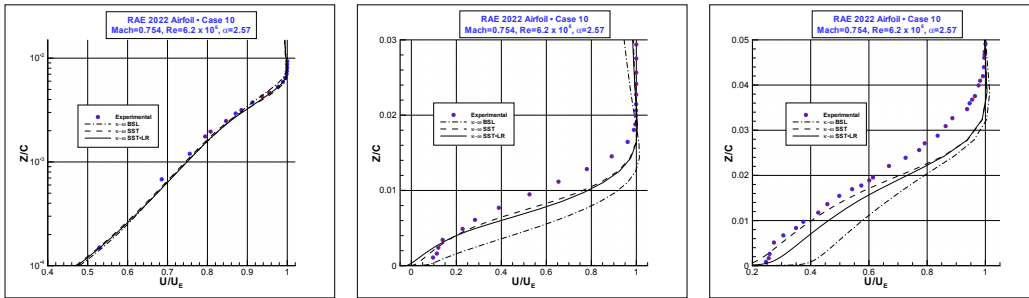
The velocity profiles at three stations on the upper surface of the airfoil are presented in figure 5.3. The first station is located upstream of the shock



(a) Pressure Coefficient

(b) Friction Coefficient

Figure 5.2: RAE 2822 Airfoil, Case 10 flow condition: Pressure and friction coefficient; symbols: experimental, $- \cdot -$: RANS $\kappa - \omega$ BSL, $- - -$: RANS $\kappa - \omega$ SST, $- - -$: RANS $\kappa - \omega$ SST-LR;



(a) $X/C = 0.40$

(b) $X/C = 0.65$

(c) $X/C = 0.90$

Figure 5.3: RAE 2822 Airfoil, Case 10 flow condition: Velocity profiles; symbols: experimental, $- \cdot -$: RANS $\kappa - \omega$ BSL, $- - -$: RANS $\kappa - \omega$ SST, $- - -$: RANS $\kappa - \omega$ SST-LR;

and all the three turbulence models provide a velocity profile in very good agreement with the experimental data. The second station is very critical because located just downstream the shock in the region of separated flow. The agreement is not as good as at $X/C = 0.40$. However, the SST and SST-LR models show a zone of negative velocity and a behaviour that resembles the experimental data. The result of the BSL model is definitely worse. The

last station is located in the region where the flow is re-attached. The κ - ω SST provides a result better than the SST-LR and a good agreement with the experimental data in the inner part of the boundary layer. The κ - ω BSL model has provided a solution without separation, and the boundary layer at $X/C = 0.90$ is significantly different with respect to the other solutions.

5.2 RAE M2155 Wing

The RAE M2155 wing placed is a transonic benchmark [59] for which the $\kappa - \omega$ SST model has provided appreciable results [21].

The case 2 condition:

- *Mach number* = 0.806
- *Reynolds number* = 4.1×10^6
- $\alpha = 2.50^\circ$

is characterized by a quite complex shock topology [59]. The flow on the upper surface of the wing is characterized by a triple shock wave system from the root to about the 50% of the span, and by a single shock wave from about the 50% to the tip. Inboard the 50% span, changes in the flow direction occur in the region of the forward leg of the triple shock wave system and in trailing edge zone but without flow separation. The flow separation starts where the three shock waves join together and ends at about 90% of the span. The separation extends for about 10% of the local chord.

A mesh with 35 blocks and about 1.2×10^6 cells has been employed. The $\kappa - \omega$ SST, SST-LR, and BSL turbulence models are applied.

The results are shown in terms of pressure coefficient at several stations along the span in Fig. 5.4. At the inboard span-wise stations, the interaction between the shock wave system and the boundary layer is not very strong and the three $\kappa - \omega$ models present the same pressure coefficients. At the stations where the shock boundary-layer interaction becomes stronger and

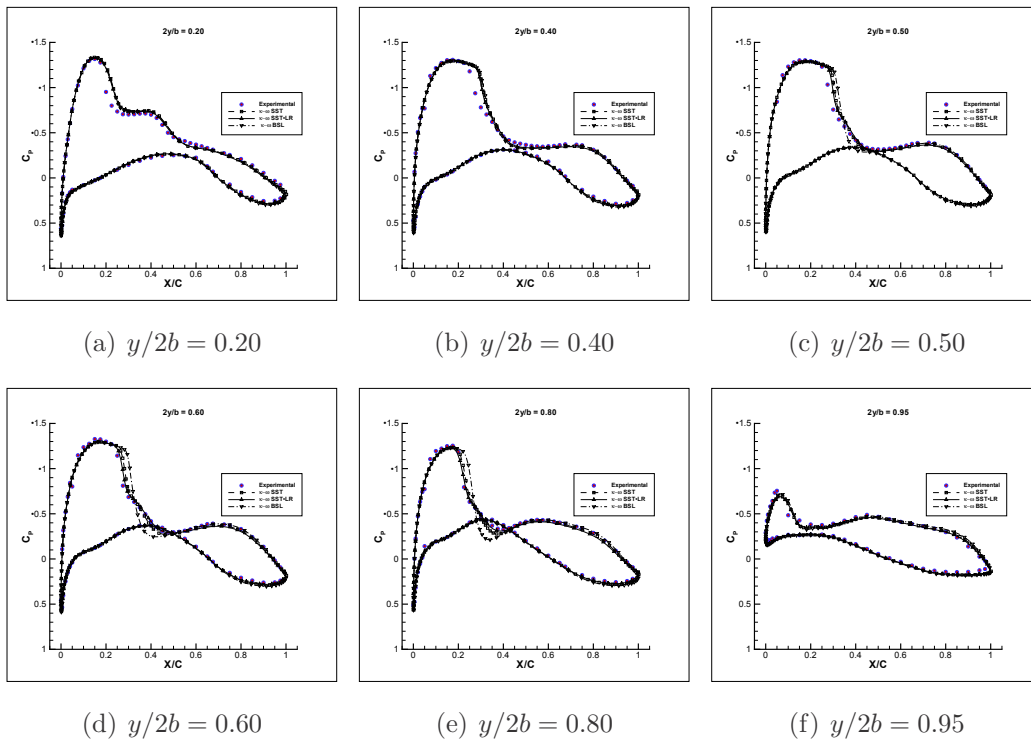


Figure 5.4: Pressure coefficients over the RAE M2155 wing; \bullet : experiment, $-\square-$: RANS $\kappa - \omega$ SST, $-\Delta-$: RANS $\kappa - \omega$ SST-LR, $-\nabla-$: RANS $\kappa - \omega$ BSL

the flow separates the $\kappa - \omega$ SST-LR provides the same results as the SST model and follows the experimental data better than the BSL model.

Conclusions

A contribution to the numerical simulation of low-Reynolds number flows has been given.

The focus has been placed on the methods based on the resolution of the Reynolds Averaged Navier Stokes equations. The capability of the turbulence models to return a laminar separation bubble has been investigated. The incompressible flow over a flat plate with an imposed pressure gradient, and around the SD 7003 airfoil have been considered. Large eddy simulations have also been performed and used as a reference for the RANS results.

Laminar separation bubbles have been found by the Spalart-Allmaras and the κ - ω SST turbulence models. The simulations have been performed using very low values of the free-stream turbulence without an *a priori* knowledge of the laminar-turbulent transition, and by prescribing the transition location as retrieved by LES data. A satisfactory prediction of the flow characteristics in the *dead air* region of the bubble is obtained. On the contrary, a poor agreement has been provided by RANS with respect to LES in the zone of pressure recovery. These discrepancies are essentially due to a too low level of turbulence in the bubble.

The behaviour of the κ - ω SST turbulence model has been investigated in detail. Simulations of the flow around the SD 7003 airfoil at Reynolds numbers 6×10^4 , 6×10^5 , and 6×10^6 have been performed. This model did not predict correctly the viscous and logarithmic regions of the boundary layer at the lowest Reynolds number. However, it has been shown that this is related to the implementation at low Reynolds numbers, rather than to an intrinsic

“design” limit of the model. Indeed, a modification has been proposed. The modified model, the κ - ω SST-LR, has provided a correct simulation of the viscous sublayer and logarithmic region in the tests performed at high and low Reynolds numbers. The laminar separation bubble arising on the SD 7003 airfoil is well captured and the results of the RANS simulations are in excellent agreement with the LES data. In addition, high Reynolds number performances of the model do not deteriorate with respect to the *standard* κ - ω SST as shown by the transonic tests around the RAE 2822 airfoil and M2155 wing. The κ - ω SST-LR turbulence model can be used in a wide range of Reynolds numbers to simulate different flow aspects from the laminar separation bubbles to the shock-boundary layer interaction.

Bibliography

- [1] Carmichael, B. H., “Low Reynolds Number Airfoil,” Tech. Rep. NASA-CR-165803, NASA, 1981.
- [2] Lissaman, P. B. S., “Low Reynolds Number Airfoils,” *Annual Review of Fluid Mechanics*, Vol. 39, 1983, pp. 223–239.
- [3] Arina, R., Atkin, C., Hanff, E., Jones, K., Lekas, T., Oi, M., Khalid, M., McAuliffe, B., Paquet, J. B., Platzer, M., Rist, U., Windte, J., and Yuan, W., “Experimental and Computational Investigations in Low Reynolds Number Aerodynamics with Applications to Micro Air Vehicles,” RTO Technical Report NATO-AVT-101, NATO, 2009.
- [4] Spalart, P. R. and Strelets, M. K., “Mechanisms of Transition and Heat Transfer in a Separation Bubble,” *Journal of Fluid Mechanics*, Vol. 30, 2000, pp. 329–349.
- [5] Spalart, P. R. and Allmaras, S. R., “A one equation turbulence model for aerodynamic flows,” 30th *AIAA Aerospace Sciences Meeting and Exhibit*, Reno, NV, Jan. 1992, AIAA paper 92-0439.
- [6] Menter, F. R., “Two-equation Eddy Viscosity Turbulence Models for Engineering Applications,” *Aerospace Science and Technology Journal*, Vol. 32, No. 7, 1994, pp. 1598–1695.

- [7] Howard, R. J. A., Alam, M., and Sandham, N. D., “Two-Equations Turbulence Modelling of a Transitional Separation Bubble,” *Flow Turbulence and Combustion*, Vol. 63, 1999, pp. 175–191.
- [8] Kalitzin, G., Gould, A., and Benton, J., “Application of two-equation turbulence models to aircraft design,” *34th AIAA Aerospace Sciences Meeting and Exhibit*, Reno, NV, 1996, AIAA paper 96-0327.
- [9] Wilcox, D. C., *Turbulence Modeling for CFD*, DCW Industries inc., La Canada, Los Angeles, California, 1994.
- [10] Windte, J., Scholz, U., and Radespiel, R., “Validation of RANS Simulation of Laminar Separation Bubbles on Airfoils,,” *Aerospace Science and Technology Journal*, Vol. 10, No. 7, 2006, pp. 484–494.
- [11] Radespiel, R., Windte, J., and Scholz, U., “Numerical and Experimental Flow Analysis of Moving Airfoils with Laminar Separation Bubbles,” *44th AIAA Aerospace Sciences Meeting and Exhibit*, Reno, NV, Jan. 3–Jan. 5 2006, AIAA paper 2006-0501.
- [12] Yuan, W., Khalid, M., Windte, J., Scholz, U., and Radespiel, R., “An Investigation of Low-Reynolds-Number Flows past Airfoils,” *23rd AIAA Applied Aerodynamics Conference*, Toronto, Canada, June 6–June 9 2005, AIAA paper 2005-4607.
- [13] Wallin, S. and Johansson, A., “An Explicit Algebraic Reynolds Stress Model for Incompressible and Compressible Turbulent Flows,” *Journal of Fluid Mechanics*, Vol. 403, 2000, pp. 89–132.
- [14] Tang, L., “RANS Simulation of Low-Reynolds-Number Airfoil Aerodynamics,” *44th AIAA Aerospace Science Meeting and Exhibit*, Reno, NV, Jan. 3–Jan. 5 2006, AIAA paper 2006-0249.
- [15] Jones, W. P. and Launder, B. E., “The Prediction of Laminarization with a Two-Equation Model for Turbulence,” *International Journal of Heat and Mass Transfer*, Vol. 15, 1972, pp. 301–314.

- [16] Ferziger, J. H. and Peric, M., *Computational Methods for Fluid Dynamics*, Springer-Verlag, Berlin & Heidelberg, 1996.
- [17] Lenormand, E., Sagaut, P., Phuoc, L., and Comte, P., “Subgrid-Scale Models for Large Eddy Simulation of Compressible Wall Bounded Flows,” *AIAA Journal*, Vol. 38, 2000, pp. 1340–1350.
- [18] Galbraith, M. C. and M. R. Visbal, “Implicit Large Eddy Simulation of Low Reynolds Number Flow past the SD 7003 Airfoil,” *46th AIAA Aerospace Sciences Meeting and Exhibit*, Reno, NV, Jan. 7 –Jan. 10 2008, AIAA paper 2008-225.
- [19] Rumsey, C. L. and Spalart, P. R., “Turbulence Model Behavior in Low Reynolds Number Regions of Aerodynamic Flow Fields,” *AIAA Journal*, Vol. 47, No. 4, 2009, pp. 982–993.
- [20] Spalart, P. R. and Rumsey, C. L., “Effective Inflow Conditions for Turbulence Models in Aerodynamic Calculations,” *AIAA Journal*, Vol. 45, No. 10, 2007, pp. 2544–2553.
- [21] Catalano, P. and Amato, M., “An Evaluation of RANS Turbulence Modelling for Aerodynamic Applications,” *Aerospace Science and Technology Journal*, Vol. 7, No. 7, 2003, pp. 493–509.
- [22] Catalano, P. and Amato, M., “A Numerical Evaluation of 2-D and 3-D Application Challenges of Transonic Aerodynamics,” *QNET-CFD Network Newsletter*, Vol. 1, No. 7, 2001, pp. 25–28.
- [23] Catalano, P., Wang, M., Iaccarino, G., and Moin, P., “Numerical Simulation of the Flow around a Circular Cylinder at High Reynolds Numbers,” *International Journal of Heat and Fluid Flow*, Vol. 24, 2003, pp. 463–469.
- [24] Kim, J. and Moin, P., “Application of a Fractional Step Method to Incompressible Navier-Stokes Equations,” *Journal of Computational Physics*, Vol. 59, 1985, pp. 308–323.

- [25] Germano, M., Piomelli, U., Moin, P., and Cabot, W. H., “A Dynamic Subgrid-scale Eddy Viscosity Model,” *Physics of Fluids*, Vol. 3, 1991, pp. 1760–1765.
- [26] Lilly, D. K., “A Proposed Modification of the Germano Subgrid Scale Closure Method,” *Physics of Fluids*, Vol. 4, 1992, pp. 633–635.
- [27] Baldwin, B. S. and Lomax, H., “Thin layer approximation and algebraic model for separated turbulent flows,” American Institute of Aeronautics and Astronautics (AIAA), 1978, AIAA Paper 78-257.
- [28] Menter, F. R., “Performance of popular turbulence models for attached and separated turbulent boundary layers,” *AIAA Journal*, Vol. 30, No. 8, 1992, pp. 2066–2072.
- [29] Wilcox, D. C., “A half-century historical review of the κ - ω model,” *AIAA Journal*, Vol. 26, No. 11, 1988, pp. 1311–1320.
- [30] Wilcox, D. C., “Reassessment of the scale-determining equation for advanced turbulence models,” *AIAA Journal*, Vol. 26, No. 11, 1988, pp. 1299–1310.
- [31] Monsen, E., Rudnik, R., and Beeckle, H., “Flexibility and efficiency of a transport equation turbulence model fro three-dimensional flows,” *Notes on Numerical Fluid Mechanics*, Vol. 60, 1997, pp. 237–244.
- [32] Menter, F. R., “Influence of free-stream values on κ - ω model prediction,” *AIAA Journal*, Vol. 30, No. 6, 1991, pp. 1657–1659.
- [33] Wilcox, D. C., “A two equations turbulence model for wall-bounded and free-shear flows,” *24th Fluid Dynamics Conference*, American Institute of Aeronautics and Astronautics (AIAA), Orlando, FL, July 6–9 1993.
- [34] Kok, J., “Resolving the Dependence on Free-Stream Values for the κ - ω Turbulence Model,” *AIAA Journal*, Vol. 38, No. 7, 2000, pp. 1292–1295.

- [35] Cazalbou, J. B., Spalart, P. R., and Bradshaw, P., “On the behavior of two equation models at the edge of a turbulent region,” *Physics of Fluids*, Vol. 5, No. 5, 1994, pp. 1797–1804.
- [36] Leschziner, M. A. and Loyau, H., “Numerical Investigation of three-dimensional transonic flows with large separation,” *ICAS 2000 Conference*, Harrogate, UK, Aug. 28 –Sept. 1 2000.
- [37] Beazard, H., Catalano, P., Courty, J. C., Kok, J., Krumbein, A., and Wallin, S., “Progress in advanced turbulence and transition modelling in the European project AVTAC,” *18th AIAA Applied Aerodynamics Conference*, Denver, CO, 2000, AIAA paper 2000-4511.
- [38] Catalano, P., Marini, M., Nicoli, A., and Pizzicaroli, A., “CFD Contribution to the Aerodynamic Data Set of the Vega Launcher,” *Journal of Spacecraft and Rockets*, Vol. 44, No. 1, 2007, pp. 42–51.
- [39] Catalano, P. and Amato, M., “Assessment of κ - ω turbulence modeling in the CIRA flow solver ZEN,” *ECCOMAS 2001 Conference*, Swansea, Wales, Sept.4–7 2001.
- [40] Amato, M. and Catalano, P., “Non Linear κ - ε turbulence modeling for industrial applications,” *ICAS 2000 Congress*, Harrogate, UK, Aug. 28 – Sept. 1 2000.
- [41] Marongiu, C., Catalano, P., Amato, M., and Iaccarino, G., “U-ZEN : A computational tool solving U-RANS equations for industrial unsteady applications,” *34th AIAA Fluid Dynamics Conference*, Portland (Or), June 28 –July 1 2004, AIAA Paper 2004-2345.
- [42] Jameson, A., “Time Dependent Calculations using Multigrid with Application to Unsteady Flows past Airfoils and Wings,” June 24–26 1991, AIAA Paper 1991-1596.

- [43] Catalano, P., “Numerical Investigation of the Flow around the Ahmed Model,” *18th AIAA Computational Fluid Dynamics Conference*, Miami, FL, June 25 –June 28 2007, AIAA paper 2007-4096.
- [44] Shur, M., Spalart, P. R., Strelets, M., and Travin, A., “Detached-eddy Simulation of an Airfoil at High Angle of Attack,” *Engineering Turbulence Modelling and Experiments - 4*, ETMM-4, Ajaccio, Corsica, FR, May24–26 1999.
- [45] Horton, H. P., *Laminar Separation in two and three-dimensional incompressible flow*, PhD thesis, University of London, 1968.
- [46] Catalano, P. and Tognaccini, R., “Influence of Free-stream Turbulence on Simulations of Laminar Separation Bubbles,” *47th AIAA Aerospace Sciences Meeting and Exhibit*, Orlando, FL, Jan. 3 –Jan. 5 2009, AIAA paper 2009-1471.
- [47] Lang, M., Rist, U., and Wagner, S., “Investigation on Controlled Transition Development in a Laminar Separation Bubble by means of LDA and PIV,” *Experiments in Fluids*, Vol. 36, 2004, pp. 43–52.
- [48] Marxen, O., Lang, M., Rist, U., and Wagner, S., “A Combined Numerical/Experimental Study of Unsteady Phenomena in a Laminar Separation Bubble,” *Flow Turbulence and Combustion*, Vol. 71, 2003, pp. 133–146.
- [49] Ol, M. V., McAuliffe, B. R., Hanff, E. S., Scholz, U., and Kalher, C., “Comparison of Laminar Separation Bubble Measurements on a Low Reynolds Number Airfoil in Three Facilities,” *135th AIAA Fluid Dynamics Conference*, Toronto, Canada, June 6–June 9 2005, AIAA paper 2005-5149.
- [50] Schlichting, H., *Boundary Layer Theory*, McGraw-Hill Book Company, 7th Edition, 1978.

- [51] Myong, H. and Kasagi, N., “A new Approach to the Improvement of the κ - ε Turbulence Model for Wall-bounded Shear Flows,” *JSME International Journal Series II*, Vol. 33, No. 1, 1990, pp. 63–72.
- [52] Catalano, P. and Tognaccini, R., “An Analysis of the Shear Stress Transport Formulation for Low Reynolds Number Flows,” *XX Congresso Nazionale AIDAA*, Milano, June29–July 3 2009.
- [53] Catalano, P. and Tognaccini, R., “Turbulence Modelling for Low Reynolds Number Flows,” *AIAA Journal*, under review for publication.
- [54] Catalano, P., Iuliano, E., Donelli, R., and Paniza, A., “A Numerical Procedure for Predicting Transition in a RANS Environment,” *XX Congresso Nazionale AIDAA*, Milano, June29–July 3 2009.
- [55] Catalano, P. and Tognaccini, R., “Numerical analysis of the Flow around the SD 7003 Airfoil,” *to be presented at 48th AIAA Aerospace Sciences Meeting and Exhibit*, Orlando, FL, Jan. 4 –Jan. 7 2010, AIAA paper 2010-68.
- [56] Selig, M. S., Donovan, J. F., and Fraser, D. B., “Airfoils at Low Speeds,” *Soartech 8*, H. A. Stokely, Soartech publications, Virginia Beach, VA, USA, 1989.
- [57] Selig, M. S., Guglielmo, J. J., Groeren, A. P., and Giguere, P., “Summary of Low-Speed Airfoil Data,” H. A. Stokely, Soartech Aero publications, Virginia Beach, VA, USA, 1995.
- [58] Haase, W., Bradsma, F., Elsholz, E., Leschziner, M., and Schwamborn, D., “EUROVAL - An European initiative on validation of CFD codes,” *Notes on Numerical Fluid Mechanics*, Vol. 42, 1992.
- [59] Firmin, M. C. P. and McDonald, M. A., “Measurements of the Flow over a Low Aspect-Ratio Wing in the Mach number range 0.6 to 0.87

for the Purpose of Validation of Computational methods,” Technical Report DRA-TR-92016, DRA — Defence Research Agency, Farnborough, Hampshire, UK, 1992.